ENGINEERING ESTIMATION OF TOPOGRAPHIC EFFECTS IN SITE RESPONSE ANALYSIS

Juan Carlos Vergara Gallego

Advisor:
Prof. Juan David Gomez

A thesis submitted for the degree of Doctor of Philosophy

May 2021

Acknowledgements

A mi esposa María, mis hijos Juan Manuel y Juliana.

A mi madre Doris y mi hermana Elisabeth.

Contents

List of Figures

Preface

Despite the irrefutable amount of theoretical and field evidence of the impact of topographic effects on the local response at a site the engineering community still lacks practical methods for its consideration in a standard routinely basis. The incorporation of topographic effects into site response analysis has been a major challenge to engineers as it involves coupling between mechanical and geometric modifications to the incident seismic waves, which at the same time demands for field data that is rarely available to the practicing engineer. On the other hand, it has been observed that the main signature of topographic effects, besides the expected change in frequency content, is its spatial variation. These complexities combined to the field data required to build fully coupled mechanical-geometrical models have resulted in complete underconsideration of these effects. In this work we follow a rational approach to study the effect of surface topography on the response at local sites after formulating the problem following a diffraction perspective. Since this work is framed in an engineering context our main result is a method to incorporate the effect of surface topography in ground response analysis. Although the method requires numerical simulations we show that if the analyst brings into the problem the dynamic properties of the structure for which the analysis is conducted in the first place very moderate models may be required. These idea leads to the concept of size conditioned response spectra which uses a target structural response spectra to fix the size of the computational model. The resulting numerical domain turns out to be of manageable size thus it can be handled with standard computing resources. Although our proposed approach is limited to surface topography the combination of the theory of diffracted waves and the consideration of the structural response creates new venues to advance in understanding the problem of topographic effects.

Chapter 1

Introduction

Topographic effects are the modifications experienced by the incident seismic field as it interacts with surface and sub-surface topography. The main signature of these effects upon the ground response is its spatial and frequency variation which implies that consideration of these effects is a fundamental input for building analysis and design. However and despite the numerous and irrefutable amount of theoretical and field evidence of the impact of topographic effects in the seismic ground motions (Trifunac & Hudson, 1971; Celebi, 1987; Assimaki & Jeong, 2013), the engineering community still lacks a solid approach for its practical consideration. Major limitations are the vast number of material and geometric parameters involved in predicting the site response within a realistic topographic scenario. At the practical level, only a few seismic regulations propose spectral modification factors to account for the presence of irregular surface topography. These so-called topographic aggravation factors (TAF) are limited as they are frequency independent thus neglecting the relative size of the topographic irregularity, sometimes resulting in excessively conservative amplifications. In this work we propose an engineering approach to incorporate the effects of surface topography into site response analysis using computing resources typically available at a consulting office.

Historically, the problem of topographic effects has been addressed, mainly by the academic and research community through 4 strategies: (i) closed-form solutions based on oversimplified models resulting from strong geometric idealizations (ii) interpretation of seismic records (iii) realistic models using high-performance computing and (iv) parametric analysis of simplified topographies . Although all these approaches have fueled the understanding of the problem they all have failed to provide code-like expressions or engineering methods applicable at the practicing level. For instance, closed form solutions, corresponding to case (i) assume isolated topographic features and are only valid under strong idealizations. Likewise, studies pertaining to cases (ii) and (iii) are also limited as they are either related to a particular scenario or require field data that is rarely available for the consulting engineer. Similarly, although parametric analysis pertaining to group (iv) provide results across a wide range of physical and geometric features of the topographic environment they are very limited at shedding light on

fundamental concepts that can be translated into general solutions.

Figure 1.1 shows, as an example of a realistic topographic environment, the case of the Aburra Valley Region in Medellin, Colombia. The observed landscape rests on top of a sedimentary basin which produces mechanical amplification. As shown in the figure the topographic setup is configured by the flat lands in the central part of the region while the east and west flanks correspond to a combination of concave and convex shapes of different characteristic dimensions. The site response in the central part is expected to be dominated by mechanical amplification which can be considered through one-dimensional wave propagation models. By contrast, predicting the response in the more complex topographic environment is a harder challenge since the different shapes are expected to interact with the incident seismic field. These geometric complexities result in changes across a wide range of frequencies in the final ground response.

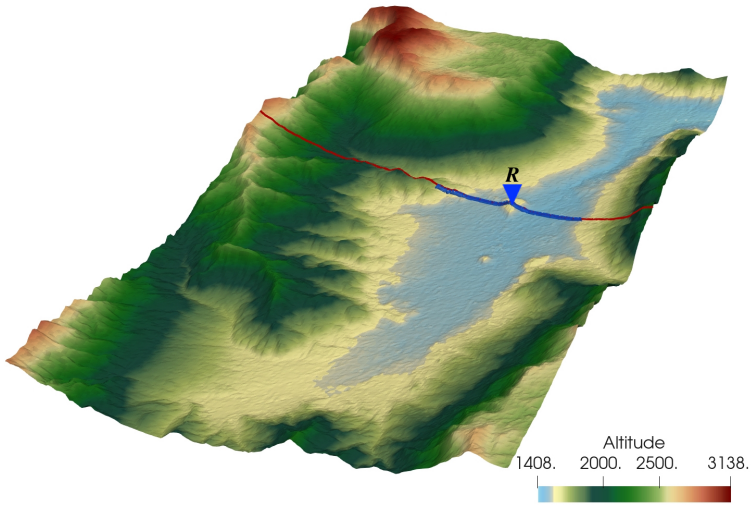

Figure 1.1. Typical topographic landscape conformed by a combination of concave and convex shapes of different size scales and exhibiting a complex interaction that can not be captured by models based upon isolated features.

In this work we contribute to the incorporation of topographic effects in site response analysis at the engineering level for sites located within realistic scenarios. As described previously such scenario is frequently the found case in urban settlements built on top of sedimentary basins with a complex surface topography. We have followed a rational and physically based approach starting from the analysis of canonical solutions initially existing within the context of scalar SH waves. One particular feature of these solutions is that the problem is formulated like a diffraction problem instead of the scattering approach typically followed in engineering seismology. In the scattering perspective the problem is formulated in terms of the so-called incoming field, which is the field

that would exist in the absence of the topographic feature, and a scattered field which is the perturbation introduced by the scatterer to the incoming field. This point of view is very useful in numerical formulations and also in practical applications since the incoming field may be obtained as an outcropping motion in terms of field records or as the superposition of incident and reflected fronts impinging against a half-space. However in the scattering approach the explicit contribution to the field from the geometric elements of the topographic feature is hardly recognized since that contribution is contained in the scattered field which is the result of a mathematical artifact. By contrast in the diffraction approach the interaction of the incident field with the canonical shape is studied by geometric methods highlighting the contribution of each one of the involved shapes to the total response. These solutions, originally developed in the context of electromagnetic waves, not only provide an analysis method that, although cumbersome to implement, can be extended to complex geometries but it is also based on solid physical concepts. For instance in the scalar problem the total response can be built by the addition of incident and reflected rays, which are easy to calculate, and diffracted waves produced by geometric singularities in the topographic profile. As will be shown later in this dissertation these cylindrical diffracted waves, which in the scalar problem are relatively simple to track and manipulate capture all the modifications introduced by the topographic profile. Curiously, this point of view of the topographic problem has not been used by researches working in the field of earthquake engineering where studies based on the scattering approach have prevailed. Although in the more general case of in-plane waves the diffracted field is highly complex as the resulting waves are now P-waves, S-waves and head-waves propagating at different speeds the same ideas can be applied in terms of numerical methods. In this dissertation we have used a boundary element algorithm to study topographic effects using a diffraction approach for two-dimensional profiles of realistic shape.

1.1 A brief survey of topographic effects and the diffraction perspective

Starting from the early contributions from Boore (1972) in very simple topographic shapes to the highly realistic models based on high performance computing (Taborda & Bielak, 2011; Restrepo et al., 2016) the effect of topography on the ground response has already written a 50 years old history. Despite these many years and strong efforts of the academic community at understanding how to incorporate the geometric effect in site response analysis, engineering practitioners are still far from having simple and effective methods to account for spatial variations of motions due to topography. This literature review is not intended to cover the many treatments and attempts to understand topographic effects but instead it is focused on those fundamental works leading to what we have called the diffraction perspective.

1.1.1 Early developments

The earliest studies of topographic effects were prompted by the San Fernando, California 1971 earthquake where anomalously high accelerations ($1.25g$) were observed near the Pacoima dam station. These amplifications, as revealed by later studies (Trifunac, 1971, 1973), were attributed mainly to the strong relief near the site (Trifunac & Hudson, 1971). Those contributions however were limited by the incipient state of numerical methods at the time, and most important, by a still limited amount of computing power. Similar works, motivated by the Pacoima dam response can be identified for instance in the analysis of 3 symmetrical and antisymmetrical inclined surfaces subjected to incident plane SH waves conducted by Boore (1972) as well as the work by Geli et al. (1988) using the Aki-Larner method to study a simple hill under SH waves but now incorporating complex sub-surface structures. Similar studies were also conducted by Sánchez-Sesma & Rosenblueth (1979) and Sánchez-Sesma (1987) who focused attention on canyons of arbitrary shapes under incident SH waves using integral formulations. Even under these simplified conditions the scattered field in the vicinity of the topographic feature in all these studies appeared so complex that arriving at general conclusions seemed an impossible task. As a result some of the research community turned its eyes to a more fundamental approach. The prevailing technical restrictions at the time were in part overcame by focusing on problems related to scalar SH waves, a problem that also had the additional advantage of being scalar instead of vectorial therefore avoiding the complexities of mode conversion at boundaries and free surfaces. At the same time, the preliminary and irrefutable evidence of topographic effects was that the ground response experiences amplifications at the top of hills and ridges.

These preliminary, but unquestionable observations led to a strong interest in fundamental problems related to simplified topographies in the form of wedges. This effort was mainly led by Sanchez-Sesma and co-workers who recognized the fundamental role of wedge-shaped geometric features in the topographic effect. Following these ideas led Sanchez-Sesma to establish the mathematical connection between the problem of scalar anti-plane elastic waves and electromagnetic waves: electromagnetic fields could also be studied in terms of scalar waves (in the form of uncoupled electric and magnetic fields), however in contrast to the problem of seismic fields, where interest remains in the total response, here the final goal is the determination of the diffracted field. Within the context of plane waves or non-planar fields represented by rays, the diffracted field is that part of the solution that cannot be built using fundamental laws of reflection and refraction. In Sanchez-Sesma's own description "diffraction is every change in the wave's path that cannot be described as reflection or refraction". For instance using seismological jargon this description can be written like

$$u = u^i + u^r + u^f + u^d \tag{1.1}$$

where u, u^i , u^r, u^f and u^d are the total, incident, reflected, refracted and diffracted fields respectively.

In a first paper in a series (Sanchez-Sesma, 1985) uses the MacDonald (1902) solution

to propose a separation of variables scheme for wedges of internal angle $\nu\pi$ subjected to plane and cylindrical SH waves. As a first general result it was shown that the amplification factor at the vertex was $2/\nu$. Later, in a short note (Sanchez-Sesma, 1990) this author found particular solutions under incident SV waves for angles of 90° and 120° and values of Poisson's ratio for which there is no diffraction.

Although the fundamental results for simple wedges appeared to pave the way in the search for general conclusions the emergence of computational tools in terms of numerical algorithms and an increase in computing power since the early to mid 90s created a proliferation of numerical solutions and parametric analysis. Highly realistic simulations using high performance computing together with the increasing number of field records have confirmed the relevance of topographic effects in site response analysis but have failed to propose engineering solutions.

1.1.2 Back to the fundamentals

Even for the simplest cases of topographies under homogeneous elastic conditions the solution to incident SH waves presented difficult challenges. However the observation that in these problems the field could be represented as per eq. (1.1) highlighted once again the importance of being able to predict the diffracted part of the motion. Surprisingly a robust technique to construct the total field in a generalized wedge was available and identified in the so-called Geometric Theory of Diffraction (GTD) in the context of electromagneitc waves as proposed by Keller (1956, 1962) and refined by Kouyoumjian & Pathak (1974). This family of solution techniques combined with today's computational resources facilitate the construction of complex solutions under SH wave incidence even for arbitrary surface topographies. For completeness this fundamental problem is shown in fig. 1.2 and its detailed discussion is the subject of chapter 3 in this work. The total solution in this problem can be obtained from superposition of the incident, reflected and diffracted field. The incident and reflected fields can be readily obtained from simple ray theory while the diffracted field, generated by the interaction between the incident and reflected fields with the geometric singularity at the corner of the wedge, can be computed from Kouyoumjian & Pathak (1974) solution. This computation of the diffracted field is possible for the interaction of a planar or cylindrical SH wave. In the case of an arbitrary surface topography with several geometric singularities each one of them becomes a source of diffracted waves which at the same time interact with the adjacent wedges generating additional higher order diffraction events.

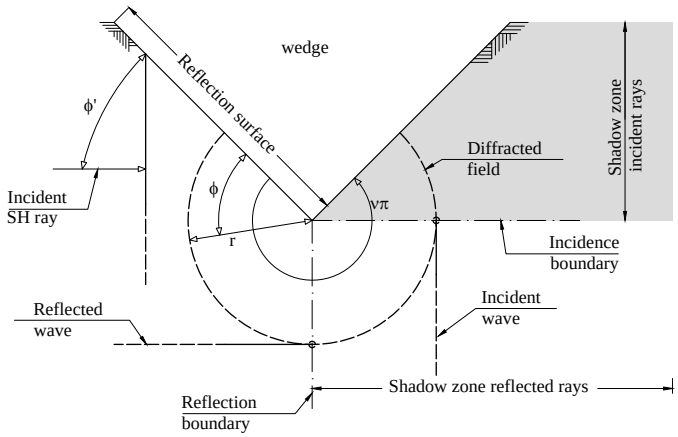

Figure 1.2. Fundamental wedge from the Geometrical Theory of Diffraction

The most important finding from the studies focusing on the diffraction field in the fundamental wedge is the fact that the effect of the geometric singularity in the vertex is a frequency dependent field that decays with distance. This means that a solution for an arbitrary topographic surface could be built as a superposition of rays (each one of which is frequency independent) and a series of diffracted fields of various orders according to the number of corner singularities existing in the profile. The theory of diffraction appears as a natural explanation of the spatial variation of the ground response in a topographic scenario. A further literature review of the theory and particular aspects of the diffraction based methods used in this dissertation are described later in chapter 3. In that same section we also conduct analysis of simple surface (concave and convex) topographies applying the solution from Kouyoumjian & Pathak (1974). These canonical analysis are conducted to demonstrate that in the simple case of SH waves there are only 6 possible patterns of spatial variation of the response in terms of amplification and de-amplification.

1.1.3 Topographic aggravation factors

Topographic aggravation factors (TAF) have been proposed by a few seismic regulations throughout the world to account for the effect of surface topography in site response analysis. The most relevant of such factors are those available in the french seismic provisions (AFPS French Association for Earthquake Engineering, 1995) and in the EuroCode (EuroCode8, 2000). The french regulation defines a TAF for sloped geometries composed by a single or a double slope as shown in fig. 1.3a while the one proposed by Eurocode (EuroCode8, 2000) is for topographic shapes as displayed in fig. 1.3b. The defining parameters in each case are also provided below. Clearly these spectral factors are very limited since they are applicable for single isolated topographies on the one hand and are frequency independent on the other hand although it is widely known that the main signature on the response of the topographic effect is precisely its spatial and frequency variation.

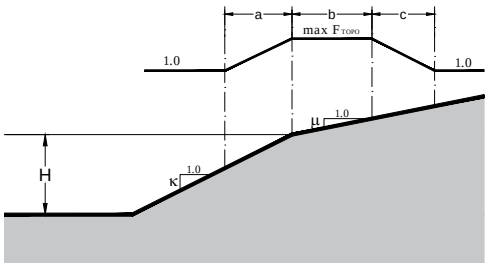

(a) Topographic aggravation factor as per the French Seismic Provisions

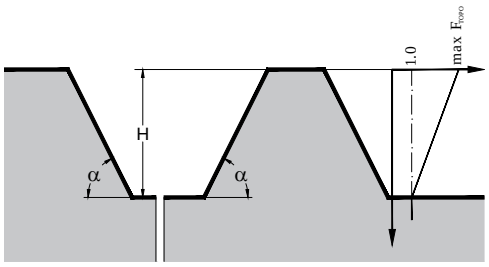

(b) Topographic aggravation factor as per EuroCode

Figure 1.3. Typical frequency (and size) independent Topographic Aggravation Factors (TAF)

$$
\begin{aligned}
a &= \frac{H}{3} \\
b &= min\left(\frac{H+10}{4}, 20\kappa\right) \\
c &= \frac{H}{4} \\
max\ F_{TOPO} &= 1.0 + 0.80\,(\kappa - \mu - 0.40) \\
1.00 &\leq max\ F_{TOPO} \leq 1.40
\end{aligned}
$$

Similarly, a TAF is proposed in EuroCode8 (2000) for shapes like the one described in fig. 1.3 and defined like:

$$
max\ F_{TOPO} = \begin{cases} 1.40, & \alpha > 30° \\ 1.20, & 15° \leq \alpha \leq 30° \\ 1.00, & H < 30m \text{ o } \alpha < 15° \end{cases}
$$

1.2 What is novel in this research?

Despite the efforts undertaken by the research and engineering community to understand the effects of topography on the response at a local site, guidelines for its actual

consideration are still missing from seismic codes. As shown previously, some of these works have focused on the analysis of idealized geometries, parametric analysis using numerical methods or large-scale models of realistic scenarios. Although all these approaches have contributed to the understanding of topographic effects from different points of view none of them have provided a general methodology that can be used by practicing engineers. In this work we use the theory of diffracted waves to propose a physically based and rational approach to incorporate topographic effects under realistic topographic environments. A new and key idea introduced in this work is the concept of a target response spectra (TRS) and its connection with the topographic scenario. A TRS is a response spectra which is accurate only over a limited period range. This novel concept starts from the engineering assumption that when performing site response analysis the engineer does not necessarily need the topographic spectral amplification across all the period range but only over a limited window. This resolution in the TRS also fixes the minimum required features in the topographic model. However, the identification of these minimum requirements in the topographic model can only be realized in terms of physically based methods. Such methods, as will be shown in this work, can be derived in terms of the diffraction perspective. As far as we know, based on our literature review, our work is the first one to address topographic effects through a direct connection with the response spectra. Furthermore, we provide engineering criteria to build topographic models that give accurate results for a specific TRS.

1.2.1 Scope of research

The local response at a site is the result of the combined effect of mechanical amplification, usually involving nonlinear response and surface and sub-surface topography which is inherently three-dimensional. Due to these complexities a complete and exact solution is only possible through realistic numerical models which would required computational resources and field data which are not available at the engineering level. At the engineering level current techniques assume a flat layered site where the mechanical effect is accounted through approximate linear equivalent methods. However, the state of the practice is still far from incorporating full models and earthquake engineering is still conducted through spectral approaches. Although in this work we still follow this spectral approach we intent to advance the field one step further. We recognize the fact that with the topographic effect being frequency dependent thus resulting in spatial variations in the response it must be solved through numerical models involving the actual topographic features. Moreover, we assume that with the existing computational power it is already possible to build moderate computational models of surface topography to conduct engineering analysis. In that sense we formulate a method to build models that rationally incorporate the effects of surface topography in site response analysis. Due to this spectral approach the method involves the range of structural periods for which the analysis is required. This idea leads to the concept of target response spectra which at the same time indicates the relevant features of the required computational model. Accordingly, a highly realistic, and numerically expensive model is required if the target is a spectral response over the full period range. However, if

the analysis is tailored to a specific period range the problem can be solved with very modest computational simulations.

On the other hand, although the fundamental concept of decay-with-distance effect present in diffracted waves is still expected to hold under three-dimensional conditions, our methods have been verified only with two-dimensional models. We believe that this is the right approach since computational resources to study 2D models are commonly available within a typical consulting company. Our results are also limited to problems under homogeneous elastic materials, with dissipation considered in terms of a quality factor. This means that the resulting amplification functions are applicable to outcroping motions corresponding to flat sites.

1.3 Report outline

This report is divided in four major parts. Chapter two provides a brief overview of an in-house boundary element algorithm used mainly as a numerical verification tool throughout this study. The algorithm is formulated in the frequency domain and can be used for scalar SH waves and for in-plane SV and P waves. We use a boundary integral formulation since we need to obtain highly accurate solutions without spurious reflections. In this same chapter we also describe the dominant geology of the Aburrá Valley Region together with its dynamic response: this is a useful scenario since it contains local sites with a wide variety of geometric shapes and the overall topography is composed of concave and convex formations of different scales. The report then describes in chapter three the fundamentals of the so called diffraction perspective. We start from the fundamental solution of the diffraction of incident SH waves by a infinite wedge and build from there to formulate a general method of analysis which has been termed superposition based diffraction. The method is then applied to the solution of canonical topographies where it is shown that all the possible cases can be solved through three different analysis. Most of the results in this chapter are given in the frequency domain. However we show that if amplification functions are given in terms of structural period these transfer functions resemble typical spectral amplification factors. The main result from this chapter is the strong relation between the topographic effects and diffracted waves. These ideas are then explored in chapter four where we introduce the concept of target response spectra and size conditioned response spectra. These limited spectral responses are used as input to the construction of the topographic model required in the computation of topographic amplification functions. Chapter five then covers a time-domain explicit finite element solver intended to be used at the practical level. In this chapter we also show how to excite a topographic model using the finite element method.

Chapter 2

Numerical description of topographic effects in the Aburra Valley Region

Introduction

Medellin is the second largest city in Colombia with an estimated population in its extended metropolitan area of nearly 4 million people and, with a public and private civil infrastructure that has seen a tremendous growth within the last 30 years. The city, which is built over a sedimentary basin, is located inside the Aburrá Valley Region (AVR) at the north end of the central range of the Colombian Andean region in Northwestern South America. The basin has a total length of about $30\,km$ and a shortest width of about $7\,km$ near its center. Most of the basin is filled by residual soils and hillslope deposits, which are susceptible to seismic wave amplification due to local effects. The eastern part of the region is dominated by moderate to steep slopes (> 30 per cent) with geometric irregularities of various lengths. In addition to this complex geometric scenario its south-east sector has experienced an increase in population leading to an architectural setting composed mostly by mid to high rise reinforced concrete buildings with fundamental periods larger than 2.0 seconds.

From the seismic point of view, the city is exposed to an intermediate activity (Aa = 0.15) as per the national seismic regulations (NSR-2010). The intensities of the seismic excitation expected in the city are mainly attributed to its location with respect to the Cauca-Romeral fault system which crosses the country from south to north. Due to the importance of the city for the national economy, the seismic response of the Aburrá Valley region (AVR) has been studied for approximately 30 years in terms of microzonation studies and the set up of Medellin Accelerographic Network (RAM). The microzonation studies have already undergone two major updates and the accelerographic network has extended to include additional municipalities located also in the AVR region. One of the main features identified in field reports after almost 30 years of records of seismic

events in the region has confirmed the marked presence of site effects which have been mainly explained through the impedance contrasts among the surface deposits in the last 100 meters of the prevailing sites. Although, mechanical amplification may be the main cause of the observed site effects it is also plausible to anticipate an important effect induced by the local and overall geometric configuration of the valley. Colombian seismic regulations allow for the implementation of local site effects through particular studies as an alternative to the mandatory site coefficient approach based upon the 30 m soil classification. However in these regulations there are no specific guidelines as to how to consider possible topographic effects if any. The topographic effect has been addressed during the last 10 years by the Applied Mechanics research group at Universidad EAFIT through large-scale and highly realistic computational models and by alternative physics-based approaches.

The possibility of field data from the accelerographic network combined with the diverse geometric formations existing in the zone make the AVR region an ideal scenario for the development of this work. Topographic effects for this scenario have already been addressed by Restrepo et al. (2016) using large scale computational models considering the seismic fault and a first version of a community velocity model for the city. That work revealed a strong modification to the incident wave field induced by topographic effects. Here we will concentrate not in the accurate prediction of the ground motions considering mechanical and geometrical effects, but only in the determination of the modifications experienced by the incident motions due to the global surface topography. Moreover, the main goal in our analysis is to test and highlight the connection between topographic resolution and spectral response and to explore its potential application to site response analysis. In this section we obtained the dynamic response of the valley using an in-house implementation of the boundary element method (BEM) (Banerjee & Butterfield, 1981). In particular we study the 2D response of two cross sections representative of the topographic environment present along the region. The response is described in terms of spectral amplification. This idea of using plane models aims at identifying fundamental physical concepts related to the interactions between incident seismic fields and simple geometric formations and that can be extended to other scenarios.

2.1 A brief description of the AVR

Figure 2.1 shows the location of the AVR region within Colombian national territory. The region rests over a depression located in the central mountain range in the north-western part of the country. Most of the city of Medellín, the main municipality in the region, is located on the low flat parts of the valley, however the mountains which are dominated by gentle and moderate slopes contain a large number of buildings of diverse quality and various construction techniques. The predominant construction type over the north-western and eastern slopes of the valley is precarious dwellings mainly of masonry and with maximum heights up to 5 stories and in many cases built with low seismic resistance standards. These construction typologies are in contrast with the reinforced concrete buildings in the south-eastern part of he valley having heights

between 10 and 30 stories and designed following Colombian seismic regulations. From the point of view of site effects and particularly those due to local topography, it is of interest to know the relationship between frequency content and the dominant dimensions of the different topographic features of the area.

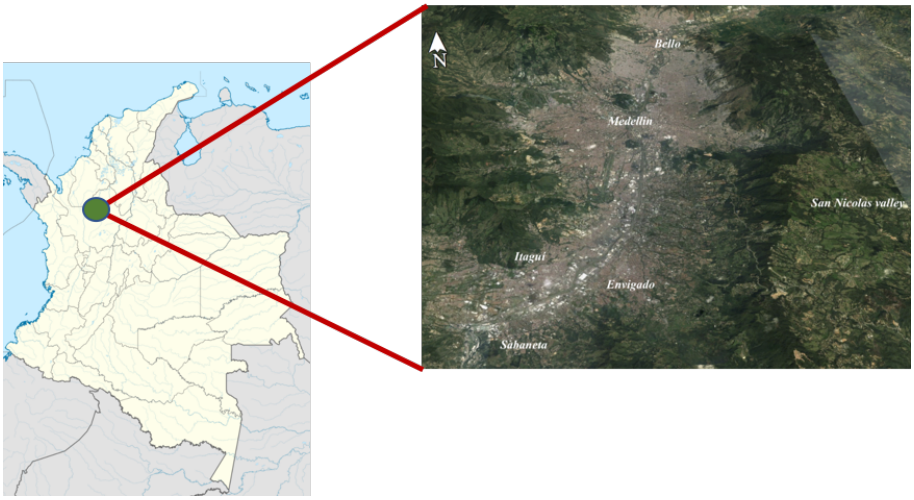

Figure 2.1. Overall view of the dominant surface topography in the Aburrá valley region. The city of Medellin occupies the most part of the valley. In the east margin of valley is located the San Nicolas Valley. Source: Google (2018)

The AVR is probably the most representative morphological feature over the northern segment of the Central Cordillera ridge in Colombia. The valley is an elongated topographic depression, relatively narrow ($7km$ in its central part) and deep (a little greater than $1000m$ with respect to a system of plateaus flanking the valley) and forged in the middle of a system of surfaces of erosion or plateaus of the middle tertiary age known as the Altiplanicie or Altiplano Antioqueño. This accident is especially influenced by several dynamic processes related to the Rio Medellín basin and framed between the higher lands of Rionegro and Santa Elena to the east along Valle de San Nicolas and the Llano de Ovejas to the west. Figure 2.2 describes the different lithological landscapes of the area (left panel) as well as the variation of its slopes (right panel).

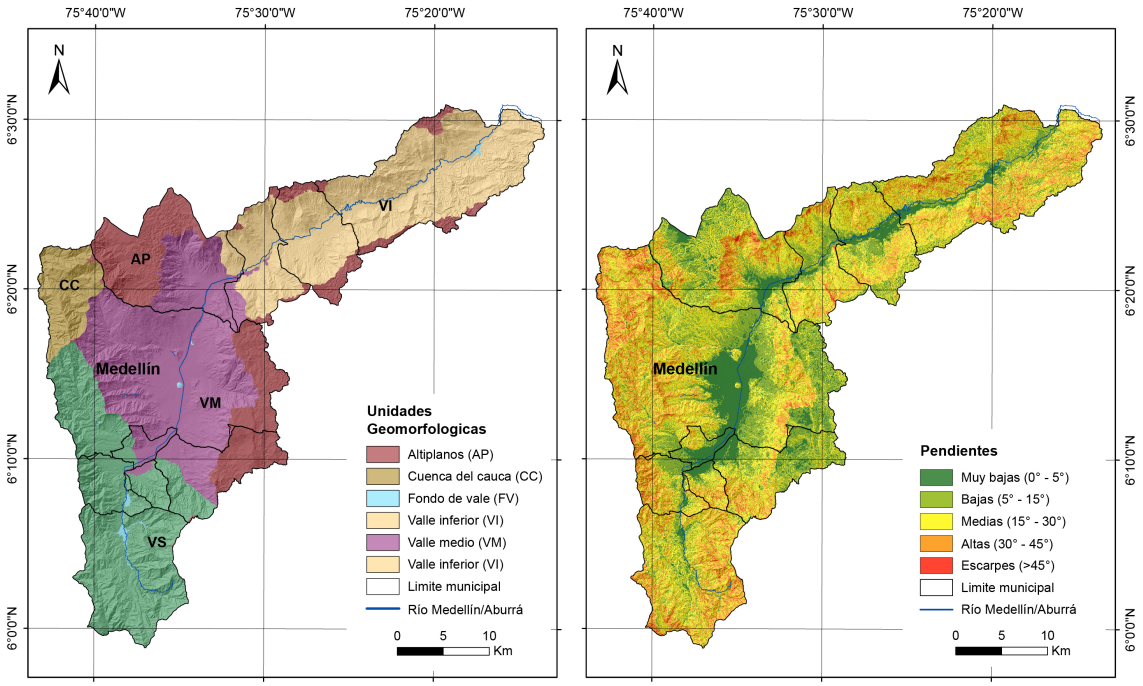

Figure 2.2. Overall view of the dominant surface topography in the Aburrá valley region. The city of Medellin occupies the most part of the valley. In the east margin of valley is located the San Nicolas Valley.

The different forms of the AVR can be explained in terms of a relief system that has been formed as a result of different geomorphological processes. Due to the particularities of the different geometric and tectonic features the region can be divided into 6 landscapes depicted in the left panel of fig. 2.2. The area called Middle Valley (MV) at the lower zone holds the city of Medellin and its extended metropolitan area. It covers a zone going from the municipalities of Itagui and Envigado (to the south) to the municipality of Bello and Copacabana (to the north). The MV is the largest area in the valley and is configured by a wide and almost flat bottom that is flanked by soft to medium surfaces conformed by systems of hills and ridges that extend all the way to the highest part shaping into linear escarpments that mark the limit between the valley and the highlands. The main characteristic of the lower zone of the MV is the fact that it is molded on alluvial deposits with very low incision, an a high heterogeneity in its granulometric composition. This condition is generated by the presence of different streams such as La Iguana, La Santa Elena, La Madera, La Miel, La Doctora and Ayura. Although the prevailing slopes are usually low (less than 5°) there are also some isolated disturbances like Cerro El Volador and Cerro Nutibara. The ridge and hill systems as well as the smooth surfaces have been developed on residual soils and in slope deposits that tend to become into drainage networks and slopes that vary from medium to high (typically between 15° and 45°). On the other hand, the escarpments are located towards the upper part of the valley. These are characterized by a minor soil development, typically converted into fresh or moderately weathered rock with different levels of fracturing, and slopes categorized as high to steep (greater than 30°). The

escarpments are the units that separate the Valley from the highland. These highlands are the direct product of concentrated erosion on the residual soils of the Batolito Antioqueño and they tend to exhibit dendritic drainage networks, with medium to low incision and slopes ranging from low (5° to 15°). These formations are concentrated between 2.200 and 3.200 meters above sea level.

2.2 Numerical determination of the response of the AVR

In this section we briefly describe our frequency domain based implementation of the direct boundary element method. We have selected a BEM technique since in this algorithm the exact implementation of the plane wave excitation is natural and since we can accurately incorporate radiation boundary conditions at infinity through Green's functions. Although in this dissertation we have used the diffraction perspective the integral formulation is readily implemented in terms of the scattered field. Accordingly in the first part of the section we formulate the scattered problem in which the excitation is in terms of the classical incoming motion or free field. In the next following sections, depending in the specific Green's function available we formulate three algorithms with different levels of approximation of the radiation condition. In the final part of the section we describe the computational model used for the simulation of two topographic cross sections in the AVR.

2.2.1 Boundary Integral Formulations of the Scattering Problem

Representation theorem for the scattered field

Consider a homogeneous isotropic elastic-half space with a scatterer (topographic irregularity) (Figure 2.3) subject to incident harmonic plane waves with a time dependence $e^{\hat{i}\omega t}$ (which is omitted here an hereafter) and where ω is the circular frequency and $\hat{i} = \sqrt{-1}$. The scatterer and half-space are characterized by its mass density ρ_i, shear modulus μ_i, and Lame constant λ_i where i=1, and 0 for the scatterer and half-space respectively. The purpose of the analysis is to determine the motions in the scatterer and inside the half-space due to the incident wave. The total response in the half-space is the superposition of incoming and scattered waves according to

$$u = u^0 + u^S \tag{2.1}$$

and where the incoming or free field motion u^0 is also the superposition of the incident and reflected waves at the free surface of the half-space in the absence of the scatterer. In this sense, the scattered field u^S, corresponds to the relative motion introduced by the irregularity with respect to the incoming wave. The Boundary Value Problem (BVP), governing the scattered motions inside the half-space can be formulated either through a differential approach or via an integral representation theorem.

If the scatterer is represented in discrete terms by a FEM model, then the effect of the half-space and its boundary conditions may be considered in the form of a standard finite element, termed herein a Half-Space-Super-Element (HSSE). In this form, the implementation of the scattering problem in a FEM-algorithm reduces to the formulation of the dynamic matrix for the HSSE and the consideration of the incident wave in the form of an effective loads vector. In this work we review the formulation and performance of several super-elements to capture the diffraction field.

The simplest approach makes use of finite elements following directly from an application of the principle of virtual work. In this case the half-space domain is discretized with finite elements up to an artificial truncation surface S_D supported on absorbing boundary elements that mimic the radiation condition. To take full advantage of the absorbing boundaries, the problem can be formulated for total motions inside the scatterer and relative (or scattered) motions inside the half-space, (Bielak & Christiano, 1984). The key aspect in that approach is the fact that the scattered motions satisfy homogeneous boundary conditions at infinity while the incoming field does not. Alternatively, the half-space can be described in terms of integral equations steaming from the elastodynamic representation theorem (Aki & Richards, 2002) and leading to different super-elements corresponding to BEM discretizations (Banerjee & Butterfield, 1981). In particular, we consider integral representations that use both, the half-space and the full-space Green tensor (i.e.,Lamb and Stokes tensors respectively). The description with the half-space Green function–simultaneously satisfying radiation and free-surface boundary conditions–results in a BEM discretization involving only boundary elements along the coupling surface S. Such description is regarded as the referent or exact solution in this study. In contrast to the exact approach, if one uses a full-space Green's function satisfying radiation condition only, the discretization of the half-space must be extended beyond the coupling surface. All these alternative integral formulations will be described next.

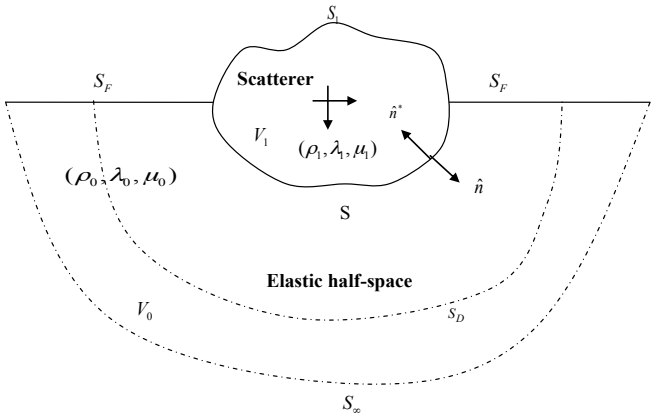

Figure 2.3. Definition of the problem domain.

Let us consider as starting point for all the subsequent integral formulations the exact elastodynamic representation theorem for the scattered motions at a point $\vec{\xi}$ over the

half-space (Pao & Varatharajulu, 1976) in terms of full-space Green tensors expressed by

$$
\begin{aligned}
u_i^S(\vec{\xi},\hat{i}\omega) = &\int_S \left[G_{ij}(\vec{x},\hat{i}\omega;\vec{\xi})t_j^S(\vec{x},\hat{i}\omega;\hat{n}^*) - H_{ij}(\vec{x},\hat{i}\omega,\hat{n}^*;\vec{\xi})u_j^S(\vec{x},\hat{i}\omega)\right] \mathrm{d}S(\vec{x}) - \\
&\int_{S_F} H_{ij}(\vec{x},\hat{i}\omega,\hat{n}^*;\vec{\xi})u_j^S(\vec{x},\hat{i}\omega)\,\mathrm{d}S(\vec{x}) + \\
&\int_{S_D} \left[G_{ij}(\vec{x},\hat{i}\omega;\vec{\xi})t_j^S(\vec{x},\hat{i}\omega;\hat{n}^*) - H_{ij}(\vec{x},\hat{i}\omega,\hat{n}^*;\vec{\xi})u_j^S(\vec{x},\hat{i}\omega)\right] \mathrm{d}S(\vec{x}) \quad \text{for } \vec{\xi} \in V_0
\end{aligned}
\tag{2.2}
$$

where $G_{ij}(\vec{x},\hat{i}\omega;\vec{\xi})$ and $H_{ij}(\vec{x},\hat{i}\omega,\hat{n}^*;\vec{\xi})$ correspond to the displacement and tractions Green's tensors respectively. The relevant surfaces and parts of the domain in this integral equation are described in Figure 2.3 and defined as follows: the surface S couples the scatterer to the half-space, the boundary S_F is the tractions free surface of the half-space, S_∞ is the external remote surface of the half-space where radiation conditions are prescribed; whenever S_∞ is rendered finite in a computational representation, this surface becomes the internal truncation surface S_D. The representation theorem (2.2), yielding the scattered motions $u_i^S(\vec{\xi},\hat{i}\omega)$ inside the half-space is exact, even for finite surfaces S_F and S_D as long as the fields $u_j^S(\vec{x},\hat{i}\omega)$ and $t_j^S(\vec{x},\hat{i}\omega;\hat{n}^*)$ to be prescribed along S_D are the correct ones.

Boundary integral equation with a full-space Green tensor $G_{ij}(\vec{x},\hat{i}\omega;\vec{\xi})$ and approximate radiation condition

If the surfaces S_F and S_D are kept finite, the representation theorem (2.2) still remains exact, but now there will be two unknown fields at the artificial boundary S_D, namely the scattered displacements $u_j^S(\vec{x},\hat{i}\omega)$ and the scattered tractions $t_j^S(\vec{x},\hat{i}\omega;\hat{n}^*)$. This equation can be approximately solved if the scattered tractions are expressed in terms of scattered displacements using local absorbing viscous boundaries (Lysmer & Kuhlemeyer, 1969) yielding the following approximated form of the representation theorem;

$$
\begin{aligned}
u_i^S(\vec{\xi},\hat{i}\omega) \approx &\int_S \left[G_{ij}(\vec{x},\hat{i}\omega;\vec{\xi})t_j^S(\vec{x},\hat{i}\omega;\hat{n}^*) - H_{ij}(\vec{x},\hat{i}\omega,\hat{n}^*;\vec{\xi})u_j^S(\vec{x},\hat{i}\omega)\right] \mathrm{d}S(\vec{x}) - \\
&\int_{S_F} H_{ij}(\vec{x},\hat{i}\omega,\hat{n}^*;\vec{\xi})u_j^S(\vec{x},\hat{i}\omega)\,\mathrm{d}S(\vec{x}) + \\
&\int_{S_D} K_{ij}(\vec{x},\hat{i}\omega;\vec{\xi})u_j^S(\vec{x},\hat{i}\omega;\hat{n}^*)\,\mathrm{d}S(\vec{x}) \quad \text{for } \vec{\xi} \in V_0
\end{aligned}
\tag{2.3}
$$

and where $K_{ij}(\vec{x},\hat{i}\omega;\vec{\xi}) = G_{pq}(\vec{x},\hat{i}\omega;\vec{\xi})\hat{i}\omega C_{ijp}\hat{n}_q - H_{ij}(\vec{x},\hat{i}\omega,\hat{n}^*;\vec{\xi})$ represents the viscous boundary contribution. The approximate representation in (2.3) can be used to obtain a pair of integral equations for the scattered displacements and tractions along the

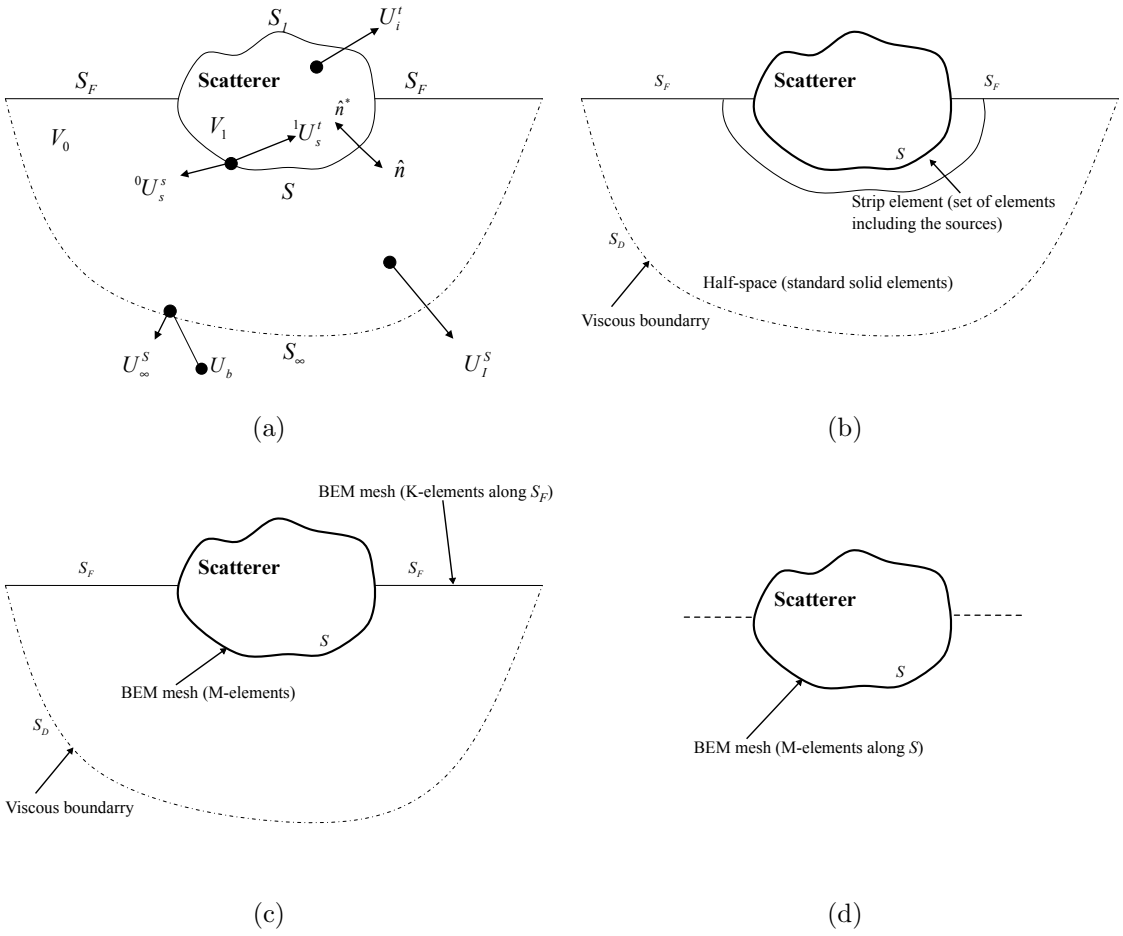

Figure 2.4. Definition of the domain and the different instances appearing in the BEM schemes

coupling surface S and for the scattered displacements along the tractions free surface S_F, see Figure 2.4c.

Boundary integral equation with a full-space Green tensor $G_{ij}(\vec{x}, \hat{i}\omega; \vec{\xi})$ and exact radiation condition

If the radiation condition along S_∞ is expressed in integral form like;

$$\lim_{\vec{r}\to\infty} \int_{S_\infty} \left[G_{ij}(\vec{x}, \hat{i}\omega; \vec{\xi}) t_j^S(\vec{x}, \hat{i}\omega; \hat{n}^*) - H_{ij}(\vec{x}, \hat{i}\omega, \hat{n}^*; \vec{\xi}) u_j^S(\vec{x}, \hat{i}\omega) \right] \mathrm{d}S(\vec{x}) = 0$$

and subsequently imposed in equation (2.2) we have the following exact representation for the scattered motions in the half-space

$$u_i^S(\vec{\xi},\hat{i}\omega) = \int_S \left[G_{ij}(\vec{x},\hat{i}\omega;\vec{\xi})t_j^S(\vec{x},\hat{i}\omega;\hat{n}^*) - H_{ij}(\vec{x},\hat{i}\omega,\hat{n}^*;\vec{\xi})u_j^S(\vec{x},\hat{i}\omega)\right] \mathrm{d}S(\vec{x}) - \int_{S_F} H_{ij}(\vec{x},\hat{i}\omega,\hat{n}^*;\vec{\xi})u_j^S(\vec{x},\hat{i}\omega)\,\mathrm{d}S(\vec{x}) \quad \text{for } \vec{\xi}\in V_0. \tag{2.4}$$

Since the free surface has to be rendered finite in the computational model, it is only possible to satisfy (2.4) approximately as specified in (2.5)

$$u_i^S(\vec{\xi},\hat{i}\omega) \approx \int_S \left[G_{ij}(\vec{x},\hat{i}\omega;\vec{\xi})t_j^S(\vec{x},\hat{i}\omega;\hat{n}^*) - H_{ij}(\vec{x},\hat{i}\omega,\hat{n}^*;\vec{\xi})u_j^S(\vec{x},\hat{i}\omega)\right] \mathrm{d}S(\vec{x}) - \int_{S_F} H_{ij}(\vec{x},\hat{i}\omega,\hat{n}^*;\vec{\xi})u_j^S(\vec{x},\hat{i}\omega)\,\mathrm{d}S(\vec{x}) \quad \text{for } \vec{\xi}\in V_0 \tag{2.5}$$

The resulting integral equation and its related boundary element scheme now takes a form close to (2.3) but with a vanishing boundary element mesh along the surface S_D, (dashed line in Figure 2.4c).

Boundary integral equation with a half-space Green tensor $G_{ij}^{HS}(\vec{x},\hat{i}\omega;\vec{\xi})$

A third algorithm can be directly derived from (2.2) if the used Green's functions satisfy the free surface boundary condition. After using the integral representation of the radiation conditions we arrive at the following representation theorem for the scattered motions in the half space;

$$u_i^S(\vec{\xi},\hat{i}\omega) = \int_S G_{ij}^{HS}(\vec{x},\hat{i}\omega;\vec{\xi})t_j^S(\vec{x},\hat{i}\omega;\hat{n}^*)\,\mathrm{d}S(\vec{x}) - \int_S H_{ij}^{HS}(\vec{x},\hat{i}\omega,\hat{n}^*;\vec{\xi})u_j^S(\vec{x},\hat{i}\omega)\,\mathrm{d}S(\vec{x}) \quad \text{for } \vec{\xi}\in V_0 \tag{2.6}$$

and where $G_{ij}^{HS}(\vec{x},\hat{i}\omega;\vec{\xi})$ and $H_{ij}^{HS}(\vec{x},\hat{i}\omega,\hat{n}^*;\vec{\xi})$ are the displacement and tractions Green's tensors for a half-space. The resulting BE algorithm now involves only the mesh along the coupling surface S as shown in Figure 2.4d. This approach may result computationally expensive since the free surface boundary condition is difficult to satisfy. In this work this condition is enforced using the Discrete Wavenumber Boundary Element Method (DWBEM), (Kawase, 1988).

2.2.2 Computational model

The dynamic response of the AVR was computed using the in-house implementation of the frequency domain boundary element method, (Banerjee & Butterfield, 1981) with an explicit consideration of radiation conditions at infinity Achenbach (1973) described in the previous section. A typical mesh is shown for reference in fig. 2.5. The considered cross sections, of approximately 20 km in width, were discretized with constant

boundary elements with a maximum size of 10 m. The analysis were conducted under vertically incident SH and SV waves with a maximum frequency $f_{max} = 6.0\ Hz$. As for the half-space we considered a perfectly elastic material with shear wave propagation velocity $\beta = 1.0\ km/s$ and a Poisson's ratio $\nu = 1/3$. For these material properties and frequency content the model guranteed at least 10 elements per minimum wave length.

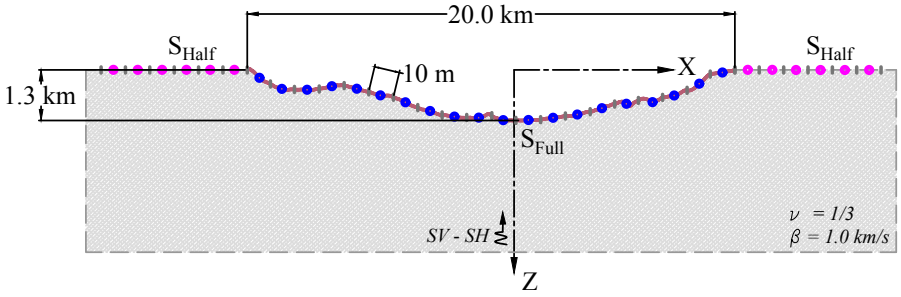

Figure 2.5. Typical boundary element mesh of a cross-section in the Aburra valley region. The models consider the Sommerfeld radiation condition.

To obtain a time domain representation of the response we also computed synthetic seismograms and used them as input motions after using a seed and a target response spectra. The seed consisted of records from the horizontal component at the Manchester station corresponding to the Hector Mine earthquake(fig. 2.6). The seeds were modified using the wavelets algorithm from Al Atik & Abrahamson (2010) in order to produce maximum spectral amplitudes in a period range between 0.5 s and 6.0 s (fig. 2.7). These artificial motions were tailored to a wide band response spectra in such a way that it would allows us to identify amplification (and deamplification) levels over a large period range.

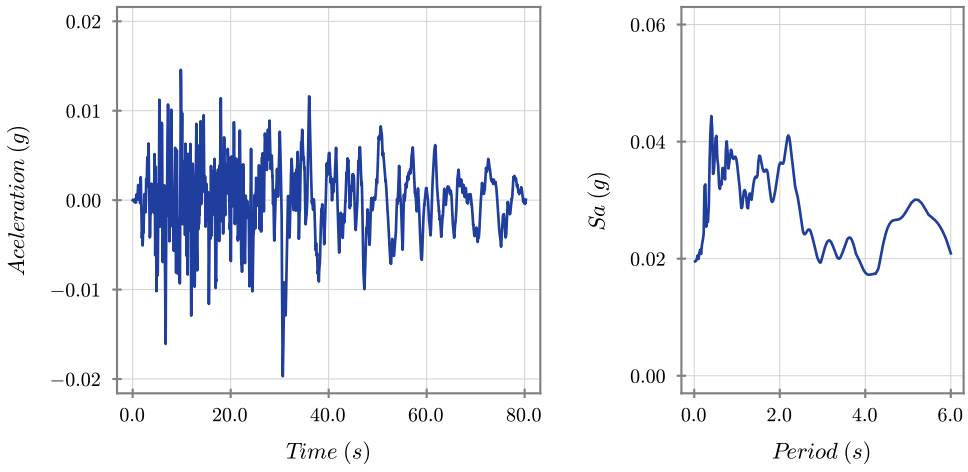

Figure 2.6. Acceleration time history and response spectra for the N-S component of the Manchester station record corresponding to the 1999-Hector Mine earthquake.

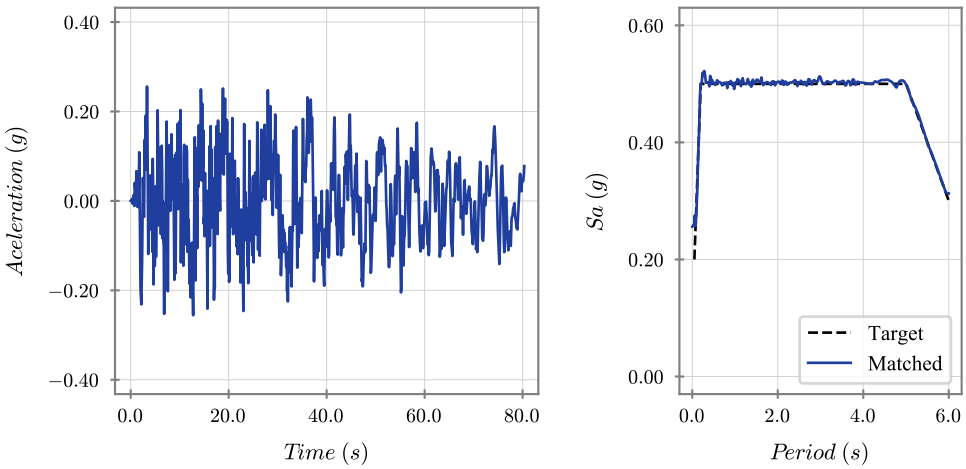

Figure 2.7. Acceleration time history and response spectra corresponding to the synthetic signal used in this study. The target response spectra corresponds is shown by the dashed line.

2.3 Dynamic response

Here we will focus in the response at the two cross sections shown in fig. 2.8 and involving localized topographic features and coupled or interacting topography. In general, both sections are representative of the topographic layout prevailing in the region with soft slopes or an almost flat configuration in the center and steeper slopes in the west and east margins. The east margin is particularly important as it continues its extension along a second flat region (not shown in the figure) with an increasing growth in population. This figure includes also an overall view of the Aburra valley showing the cross sections to be analyzed and its corresponding topographic profile (with distorted vertical scale).

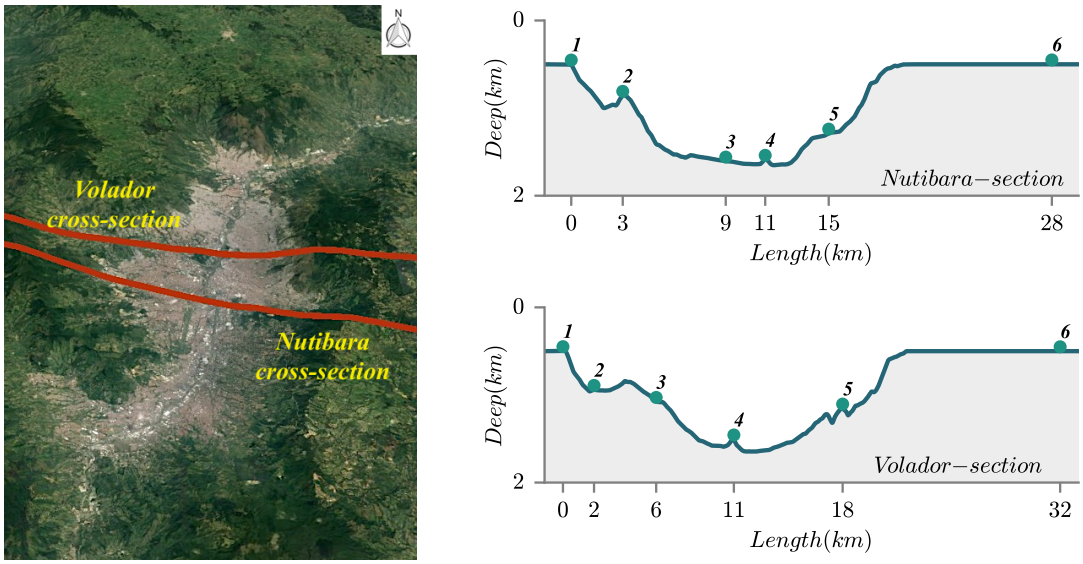

Figure 2.8. Overall view of the dominant surface topography in the AVR. The shaded rectangles correspond to the two west-east cross sections analyzed in this work. Both sections contain a localized topographic feature in the form of an isolated hill in the center of the valley and a stronger coupled topography towards the east and west margins. In both cases the slopped parts of the topographic scenario are highly populated with a large density of reinforced concrete buildings with varying quality levels.

From the geometric point of view present in both cross sections we can identify the following general typologies: (i) localized or isolated topographies with small characteristic dimension expected to produce changes in the high frequency regime (ii) clusters of concave and convex shapes with strong interaction expected to produce complex interference patterns (iii) large scale or regional topography expected to influence the low frequency regime and (iv) localized zones near sharp changes in slope. In the remaining of this work we will use the terms isolated and coupled when referring to cases (i) and (iii) to (iv) respectively. As pointed out previously most of the theoretical works have been devoted to the study of isolated topographies while the coupled general case has been studied exclusively by numerical models. The complexity in the scenario and the variability in the numerical results clearly demonstrate the challenge involved in the development of simplified analysis procedures for topographic effects. This research aims at developing physical understanding of the scattering of waves in such complex geometric scenarios with the goal of identifying controlling parameters. Although the variability of the results suggest that in order to predict the nature of the ground mo-

tions, even at the practicing level, the analysis necessarily requires the use of numerical simulation, here we intend to provide guidelines that can be used for the construction of the proper numerical model at specific conditions. Points marked ① through ⑥ indicate receivers for further analysis. The first cross section contains an isolated hill, named Cerro Nutibara, located at the bottom of the valley (receiver ④). This formation has a shape closely resembling that of a trapezoidal wedge of approximate height $h = 120\ m$. Cerro Nutibara (CN) section also contains a smaller isolated hill over the west flank (receiver point ②) and a flat step-like site over the east flank (receiver point ⑤). This last site is characteristic of artificial formations introduced during typical construction process. A second flat site has also been selected at the bottom of the valley (receiver point ③) locally approaching half-space conditions as the flat geometry is enclosed by the lateral boundaries defining the slopes of the valley. The second cross-section under analysis contains also an isolated hill, known as Cerro Volador (CV) with a trapezoidal shape of approximate height $h = 180,\ m$ (receiver point ④) and located at the bottom of the valley. By contrast with the CN section, this formation contains a small depression in the west flank with a form closely approximating that of a V-shaped canyon (receiver point ②). Towards the east margin the cross section includes a second small-scale hill (receiver point ⑤) as opposed to the flat feature considered in the CV section. We have also included a flat site located over the west flank (receiver point ③). This last point is intended to produce results comparable with those at point ③ in the CN cross section. In addition to the previously described set of receivers both models consider also a diffraction source located along the top part of the west margin (receiver points ①) and a half-space points located over the east, in the region identified as San Nicolas valley (receiver points ⑥). The considered cross sections and selected set of receivers are expected to represent topographic effects in a wide frequency regime and at the same time introduce different spatial motion variation. Table 2.1 presents a physical description of the different receivers along both cross-sections.

Feature	Name	Receiver	Cross section
	Diffractor	①	CN, CV
	High frequency canyon	②	CV
	High frequency hill	②	CN
	Flat open	③	CN
	Long slope	③	CV
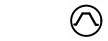	Isolated hill	④	CN , CV
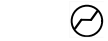	Flat closed	⑤	CN , CV
	Halfspace	⑥	CN , CV

Table 2.1. Physical description of the receiver points considered in this study.

Figure 2.9 to fig. 2.12 display the spectral response for each cross section under vertically incident SH and SV waves. In each case the plot shows the spectral acceleration at the

receiver point indicated in the insert figure. The blue trace marked as $1D$ in the plots corresponds to the perfect half-space response in such a way that the actual response (labeled as exact in the figures) is indicative of the topographic changes experienced by the incident wave field.

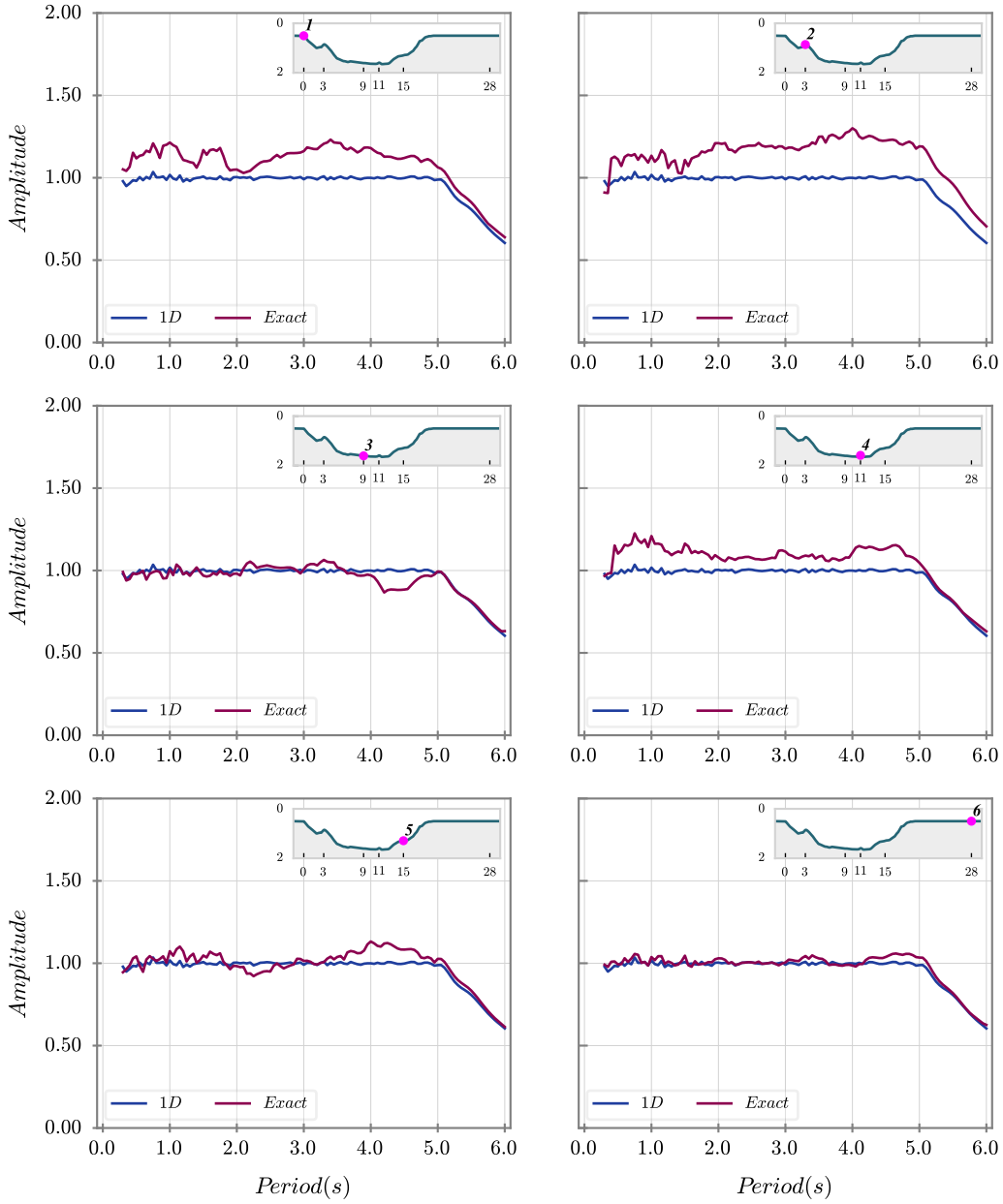

Figure 2.9. Acceleration response spectra along the 6 receiver points in the cerro Nutibara cross section under vertically incident SH waves. The trace marked as target corresponds to the response spectra under perfect half-space conditions

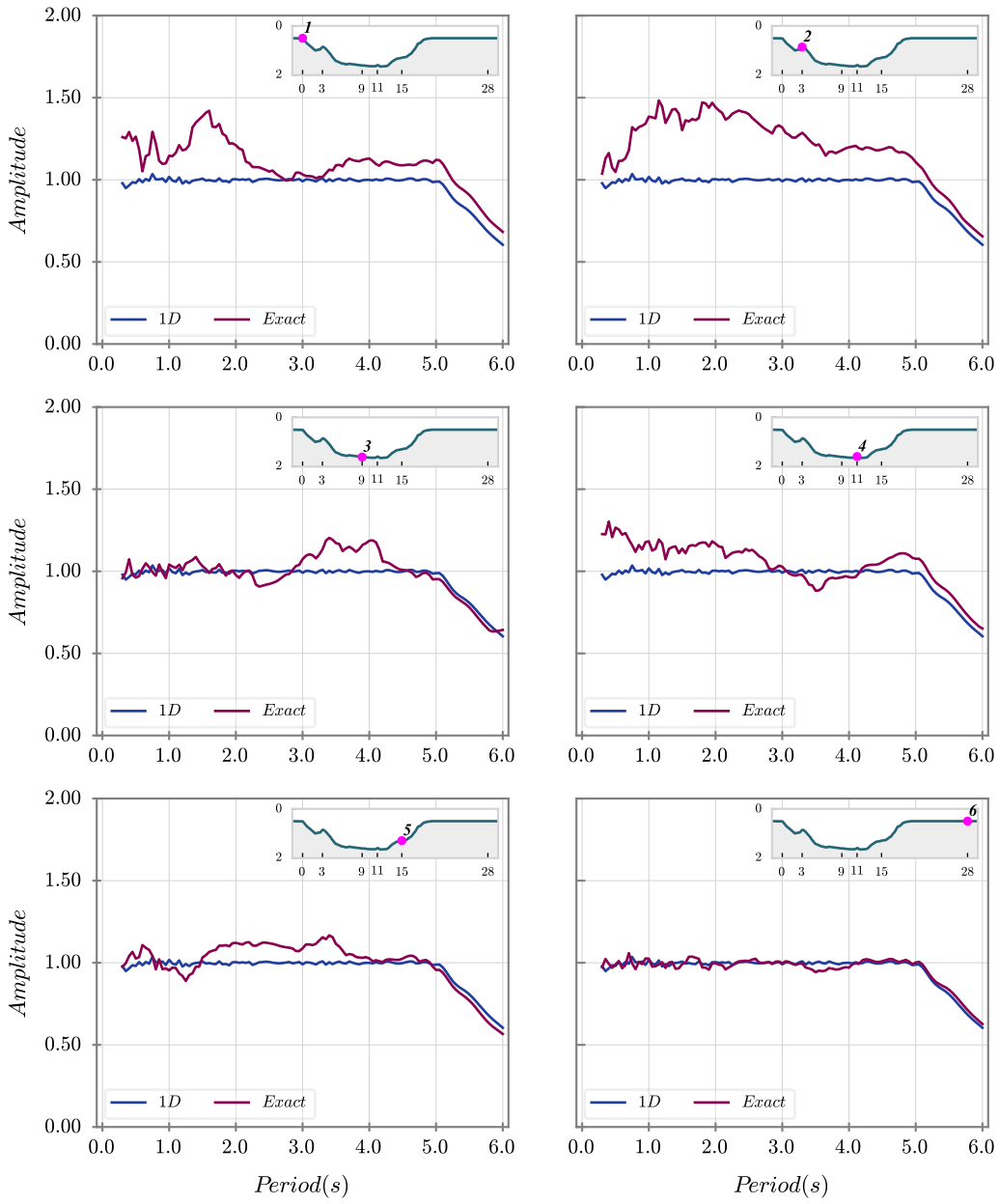

Figure 2.10. Acceleration response spectra along the 6 receiver points in the cerro Nutibara cross section under vertically incident SV waves.The trace marked as target corresponds to the response spectra under perfect half-space conditions

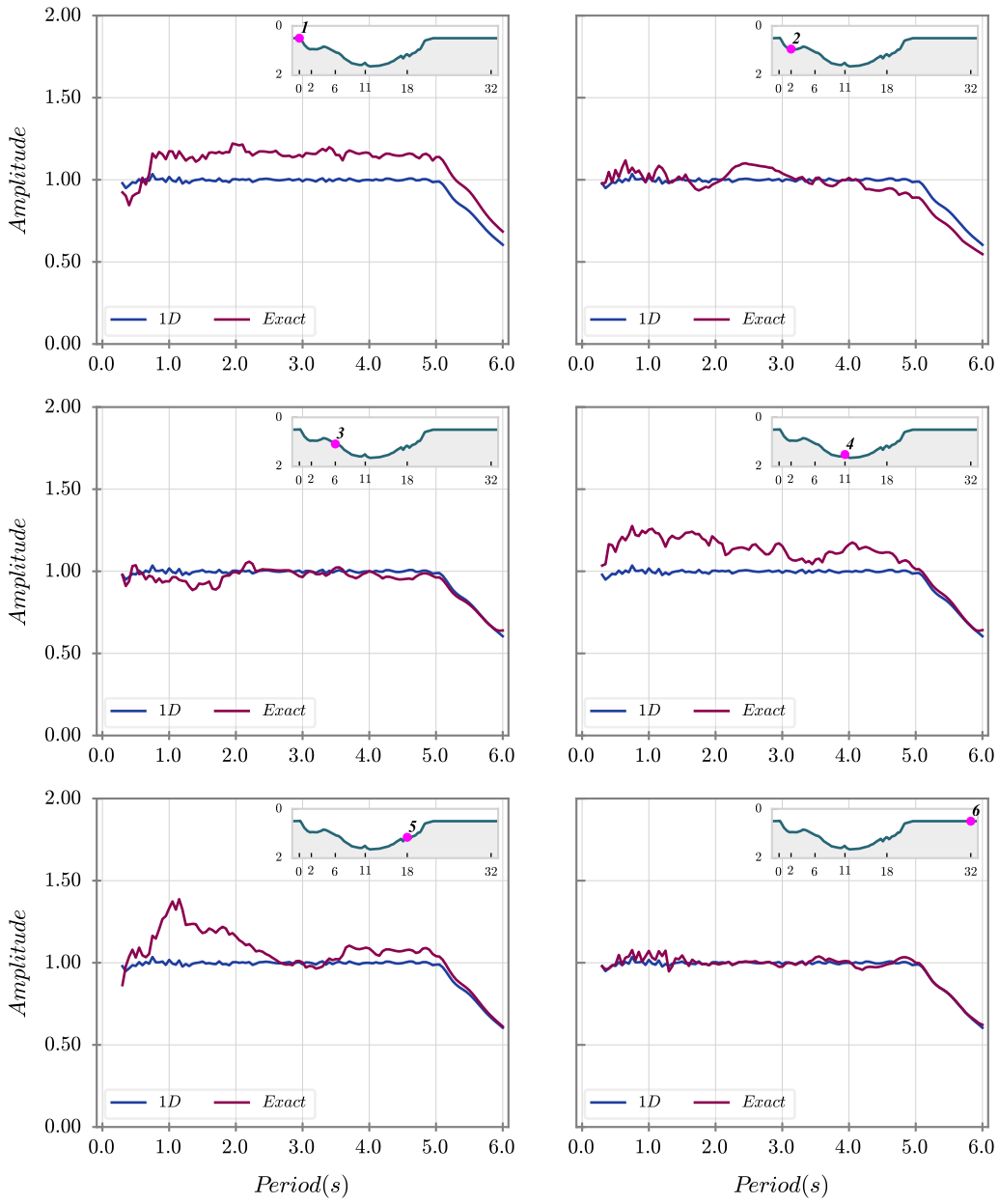

Figure 2.11. Acceleration response spectra along the 6 receiver points in the cerro Volador cross section under vertically incident SH waves. The trace marked as target corresponds to the response spectra under perfect half-space conditions

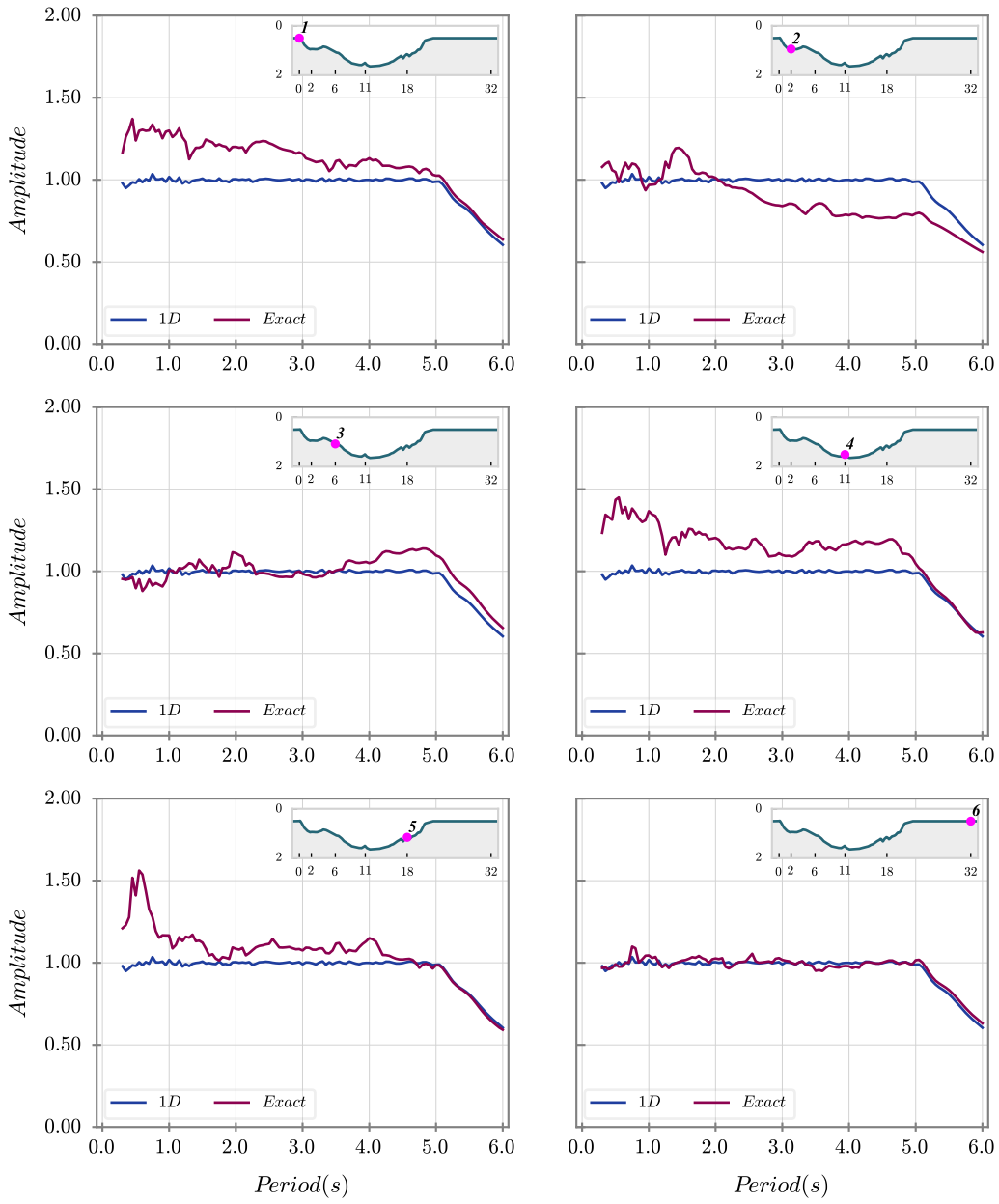

Figure 2.12. Acceleration response spectra along the 6 receiver points in the cerro Volador cross section under vertically incident SV waves. The trace marked as target corresponds to the response spectra under perfect half-space conditions.

The spectral results in both cross sections exhibit a strong spatial variation with a combined pattern of amplification and deamplification. Although there are some points located at strongly marked topographic features, like the hills at points ② in CN-section and those at point ④ in both cross sections, the response in these cases is not consistent with theoretical results predicted by models where the topographic feature is maintained isolated. These results are suggestive of the presence of a regional effect

introduced by the large scale topography and by interactions between nearby features. These findings, however, must be further explored. Such possible regional effect is also apparent at ⑤ in CV-section. That observation point corresponds to a localized flat site placed over the right slope of the valley and shows an amplification peak close to $0.5s$ while the amplification decreases over the high period range.

Conclusions

We described, from a topographic point of view, the Aburrá Valley Region in Medellin, Colombia. We have selected this scenario as a test space to study site effects involving topography since it contains localized and interacting topography of wide diversity. In conclusion this geometric scenario is highly interesting for the study of topographic effects since it is realistic and at the same time offers several conditions of geometric typology. The analyses were conducted with an in-house implementation of the frequency-domain-based boundary element method. In particular we describe three alternative algorithms depending on the implemented Green's function and its ability to satisfy radiation boundary conditions. In the next section we proceed to determine the dynamic response of two cross sections along the valley under vertically incident horizontally and vertically polarized shear waves.

The transfer functions resulting from the analysis were convoluted with an acceleration time history synthetically produced from a seed earthquake previously scaled to match a target response spectra with near constant amplitude in the period range between 0.5 s and 6.0 s. The resulting acceleration time-histories were later used in the computation of acceleration response spectra at several observation points. The spectral amplitudes reveal strong spatial variations in motion due to the topographic effect. The motion at local isolated topographies is not always consistent with theoretical observations from analysis when these features are considered isolated. On the other hand, the response at two specific locations is of particular interest. First, at receivers located over the steep slopes surrounding the region, the topographic effect appears to be rather moderate, probably due to the combination of constructing and destructing interference among the local sites. Second, the observation point located near the upper corner of the region exhibits strong amplification although it is located in a flat zone.

Chapter 3

The diffracted field and topographic effects-Analysis under incident SH waves

Introduction

The wedge as a fundamental topographic element has been recognized by Sáenz et al. (2019). Furthermore, Jaramillo et al. (2012) and Gomez et al. (2016) formulated a method to find the SH-wave response of irregular surface topographies built through the superposition of several wedges. The interaction of plane and/or cylindrical waves with a semi-infinite wedge is a fundamental problem which has been widely studied within the context of electromagnetic waves. A seminal contribution in the field is clearly identified in the work of Sommerfeld (1896) which at the same time fueled future developments like those from (Keller, 1962, 1956) who used a diffraction coefficient to express the diffraction field as a function of the incident wave. The geometric theory of diffraction from Keller was further advanced by Kouyoumjian & Pathak (1974) who proposed a high frequency solution valid in the transition regions adjacent to shadow and reflection boundaries and useful in practical applications. The Kouyoumjian & Pathak (1974) solution was then particularized by Jaramillo et al. (2012) to the case of SH waves. Of paramount importance to the Kouyoumjian & Pathak (1974) solution is the appearance of a transition function in the form of a Fresnel integral. This function effectively takes care of restoring continuity at the boundaries while producing a geometrically spreading field. This chapter covers fundamental aspects of the diffracted field and at the same time addresses its impact in the problem of topographic effects. In particular, the chapter covers canonical topographies which exhibit additional limiting values and properties of the diffracted field not reported elsewhere.

The chapter is divided in 3 sections. The first part covers the fundamental Kouyoumjian & Pathak (1974) solution highlighting interesting aspects of the diffracted field. The second part focuses on the response of surface topographies based on canonical cases.

These serve to exhibit additional phenomena contributed by the diffracted field and not observed without the application of superposition of several solutions. The last part of the chapter is dedicated to the spectral response of the considered topographic irregularities.

3.1 Diffraction by a wedge

As described previously the geometric singularity present in the semi-infinite wedge has long been recognized as the key element in topographic irregularities . This section focuses in the response of this particular irregularity to incident SH waves since for this idealized case the resulting diffracted field does not experiences mode conversions allowing us to identify key ideas to explore in the problem of in-plane waves. For this purpose fig. 3.1 shows a semi-infinite wedge of internal angle $(2-n)\pi$ where n is a factor varying between 1.0 and 2.0. The wedge is subjected to an incident plane wave u^{IN} of horizontal polarization forming an angle ϕ' with the free surface, and producing a reflected field u_F^R. The dashed lines marked as IB and RB define regions of discontinuity of the geometric field setting up associated shadow zones. This discontinuous optical field (OF) is thus given by

$$u_F^0 = u^{IN} + u_F^R \tag{3.1}$$

while the complete solution at field point (r, ϕ) is

$$u^T = u^{IN} + u_F^R + u^D \equiv u_F^0 + u^D \tag{3.2}$$

and where u^D is the diffracted field. Since the response of the geometrical field is different in the regions separated by a boundary, there is a transition region adjacent to each boundary along which there is a rapid variation of the field between the two regions. The diffracted field exactly provides the correct transition between the illuminated regions and the shadow zones. The problem of predicting the diffracted field by the illuminated wedge has been widely studied in the context of electromagnetic waves and relevant observations are summarized as described next.

- Diffraction is the result of boundaries in the geometric optics field produced by partial illumination or by corner singularities in the illuminated zones.
- The diffraction field exists everywhere and restores continuity to the discontinuous optical field.
- Along the transition regions the magnitude of the diffracted field is comparable to that of the incident and reflected field.
- The diffracted field satisfies traction free boundary conditions present at reflecting surfaces.
- The diffracted field reaches limit values at the incident and reflection boundaries.

- In the wedge problem the diffracted field u^D depends upon the wedge angle $n\pi$ and the incidence angle ϕ'.
- Over the incidence and reflection boundaries the diffracted field assumes a sign relative to the incident front corresponding to the ray optics field, which is opposite in the illuminated zone and equivalent in the shadow zone.

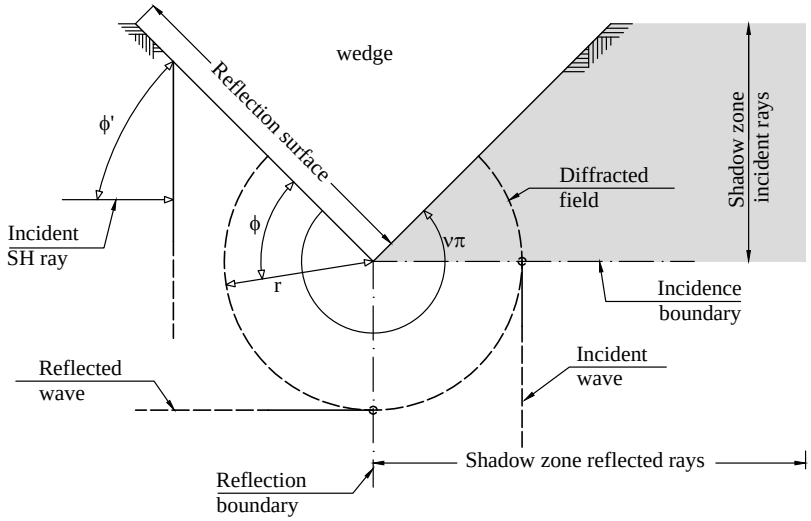

Figure 3.1. Fundamental semi-inifnite wedge under an incident plane SH wave front. The wedge has an external angle $\nu\pi$ and internal traction's free surface. The discontinous lines inside the computational doamin correspond to planes of displacement discontinuities along which the incident or reflected fields are interrupted.

The closed form solution to the wedge problem formulated by Kouyoumjian & Pathak (1974) is given in eq. (3.3) below as follows:

$$
\begin{aligned}
u^D(\phi, r) = A \frac{-e^{\left(-\hat{i}(kr+\pi/4)\right)}}{2\nu\sqrt{2\pi}\sqrt{kr}} \Bigg[& \cot\left(\frac{\pi + (\phi - \phi')}{2\nu}\right) F\left(kLa^+(\phi - \phi')\right) \\
& + \cot\left(\frac{\pi - (\phi - \phi')}{2\nu}\right) F\left(kLa^-(\phi - \phi')\right) \\
& + \cot\left(\frac{\pi + (\phi + \phi')}{2\nu}\right) F\left(kLa^+(\phi + \phi')\right) \\
& + \cot\left(\frac{\pi - (\phi + \phi')}{2\nu}\right) F\left(kLa^-(\phi + \phi')\right) \Bigg]
\end{aligned}
\tag{3.3}
$$

where r =radial coordinate to the field point measured from the vertex of the wedge, ϕ = angular coordinate measured with respect to the reflection boundary, ϕ' =incidence angle measured with respect to the reflection boundary, $\nu\pi$ =wedge angle, r' =radius of the incident cylindrical wave (for the diffraction of a cylindrical front), k =wave

number and β =velocity of wave propagation. The remaining terms appearing in (3.3) are defined as

$$F(X) = 2\hat{i}\sqrt{X}e^{\hat{i}X}\int_{\sqrt{X}}^{\infty} e^{-\hat{i}\tau^2}\mathrm{d}\tau$$

$$L = r \qquad \text{for incident plane waves}$$

$$L = \frac{rr'}{r+r'} \qquad \text{for incident cylindrical waves}$$

$$a^{\pm}(\theta) = 2\cos^2\left(\frac{2\nu\pi N^{\pm} - \theta}{2}\right)$$

$$N^{+} = \begin{cases} 0 & \text{if } \theta \leq \nu\pi - \pi \\ 1 & \text{if } \theta > \nu\pi - \pi \end{cases}, \quad N^{-} = \begin{cases} -1 & \text{if } \theta < \pi - \nu\pi \\ 0 & \text{if } \pi - \nu\pi \leq \theta \leq \pi + \nu\pi \\ 1 & \text{if } \theta > \pi + \nu\pi \end{cases}$$

From the solution described in (3.3) it is clear that the diffraction yields a cylindrical front and that for values of ϕ corresponding to points far removed from the incidence and reflection boundaries, the amplitude decays with $1/\sqrt{kr}$. On the other hand, right at the incidence/reflection boundary the diffracted field is discontinuous. This is a required condition that must be satisfied by the term u^D in order to match the corresponding discontinuity appearing in the superposition of the incident and reflected contributions.

3.1.1 Two relevant cases

Two relevant cases within the context of topographic effects are discussed next. The first case corresponds to the more general scenario of partial illumination by the incident field as displayed in fig. 3.2 where the wave is propagating along the horizontal direction. Values of the amplitude of the wave field at the incident and reflection boundaries for the incident and diffracted components are reported in each case. The limit values, corresponding in this case to $u^D = \pm\frac{1}{2}e^{i\kappa r}$ have been calculated in Jaramillo et al. (2012). Note that the total field at the boundary results from $u^T = 1.0 - 0.5 + 0.5 \equiv 1.0$. In the near field, as $r \to 0$ this value of the diffracted component of the response remains close to 1.0 but it geometrically spreads as $r \to \infty$. In the case of surface topography the diffracted wave traveling along the free surface may interact with nearby irregularities producing increments in the duration for the ground motions at the site.

The response of the wedge in the time domain is also shown in fig. 3.3 in terms of snapshots at different instants. The three reported cases correspond to the ray optics field, the diffracted field and the total response. The incident and reflection boundaries are evident in the first two cases.

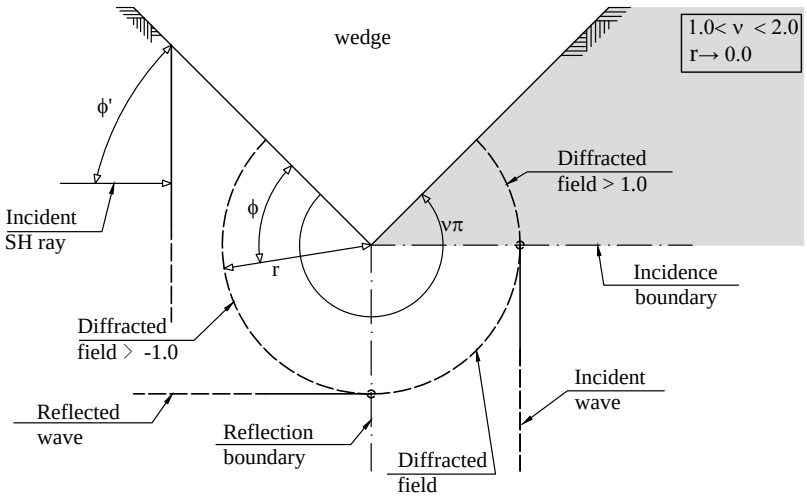

Figure 3.2. Incident, reflected and diffracted fronts corresponding to the case of partial illumination. The field values shown at the boundaries correspond to limits in the far field behaviour.

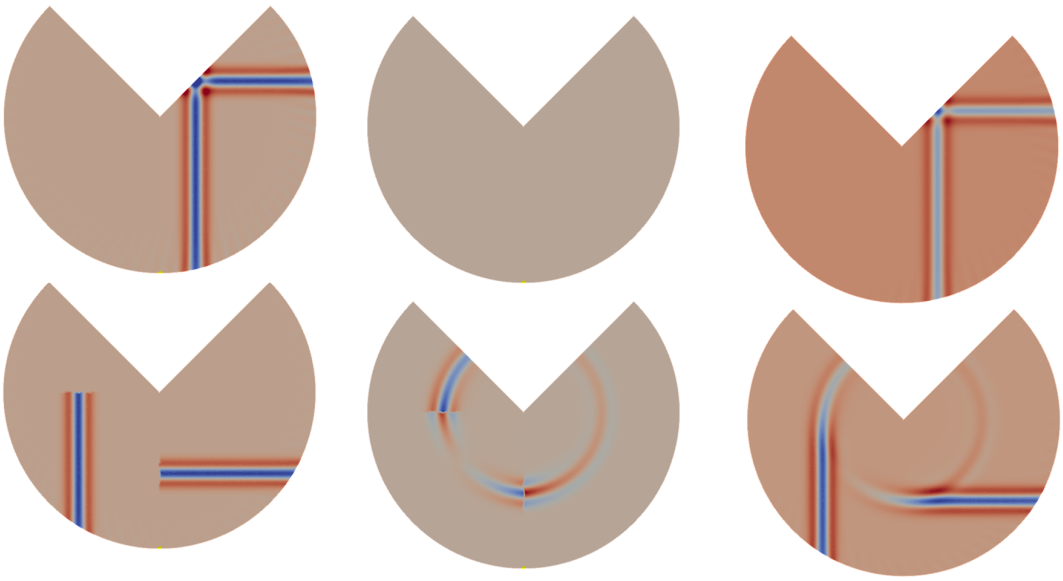

Figure 3.3. Snapshots at different time instants for the case of partial illumination corresponding to the optical field (first column), the diffracted field (second column) and the total field (third column).

The second relevant scenario corresponds to full illumination by the incident wave as shown in fig. 3.4. In the figure the wedge is a rectangular wedge and as a result the reflected field is horizontal therefore generating two reflection boundaries meeting at the vertex. Sanpshots for this solution are also shown in fig. 3.5.

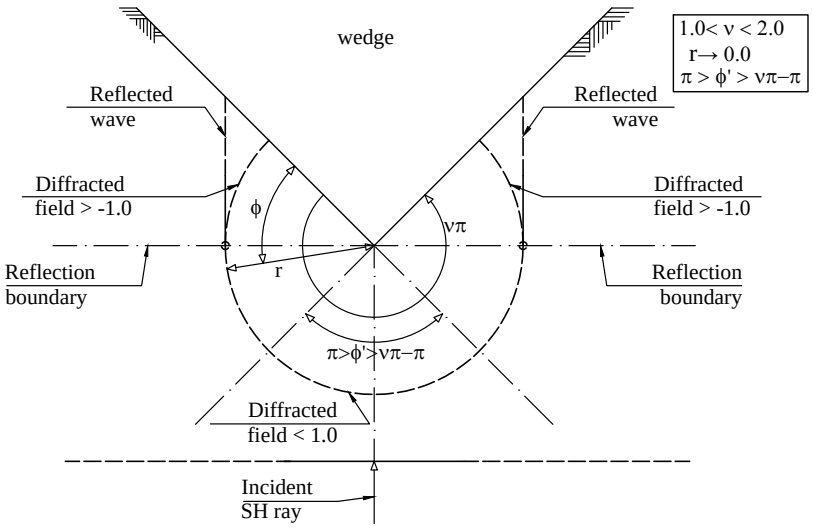

Figure 3.4. Incident, reflected and diffracted fronts corresponding to the case of full illumination. The field values shown at the boundaries correspond to limits in the far field behaviour.

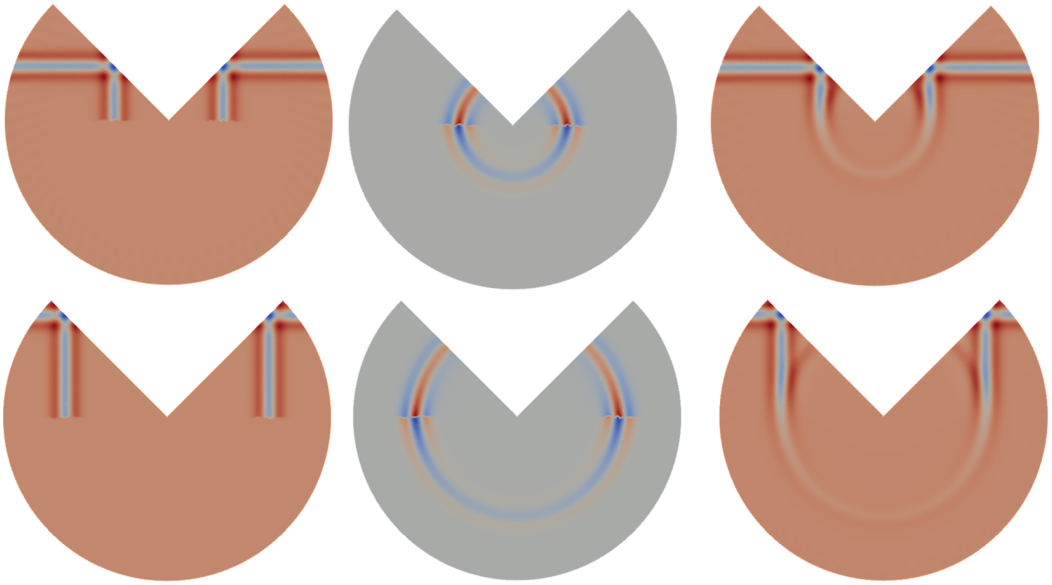

Figure 3.5. Snapshots at different time istants for the case of full illumination corresponding to the optical field (first column), the diffracted field (second column) and the total field (third column)).

3.2 Response of simple surface topographies

There have been numerous studies of topographic effects based upon the assumption of horizontally polarized shear waves. Among these, the most relevant investigations are identified in the works by (Trifunac, 1971, 1973), who found the frequency-domain solution to the scattering of plane SH waves by a semi-circular canyon and a semi-

circular valley using a separation of variables approach; and by Sanchez-Sesma (1985, 1990) on the problem of infinite wedges of internal angle $\nu\pi$ (where $0 \leq \nu \leq 2$) also under incident SH waves. Both sets of solutions are actively used in the validation of numerical implementations and as first order approximations to predict the amplification by more complex topographies. More recently, solutions in terms of wave function expansions for the scattering of SH waves by irregularities of various shapes have also been developed by a region matching technique (Tsaur & Chang, 2008; Tsaur et al., 2010; Han et al., 2011; Gao et al., 2012; Zhang et al., 2012; Gao & Zhang, 2013; Tsaur & Hsu, 2013): although these works correspond to the simplest case of scattering of scalar waves by strongly idealized geometries, they constitute a useful data-base of solutions that can be used to build conceptual understanding of the problem. Due to the simplicity behind SH based models they appear highly attractive as an actual engineering tool to predict geometric effects.

In this work we study topographic effects in terms of two simple models. We follow a fundamental approach based upon superposition ideas and aimed at revealing physical aspects of the response not evident in general solutions. We have selected as study cases the simple topographies of a V-shaped canyon and a V-shaped hill under the incidence of SH waves. Both problems can be used as fundamental or basic solutions to approximate the field in more complex topographies. Here, instead of conducting a typical parametric analysis, we select 6 particular configurations for the geometry in order to expose interesting aspects of the response. As analysis technique we use a partition of the field, where we separate from the total solution the geometrical and diffracted displacement components. The study of the diffracted part of the motion is relevant as this component is aware of the size of the irregularity. This is in contrast to the geometrical field whose amplitude for a given frequency remains constant with distance. We accomplish the separation of the different fields using a combination of numerical results with classical ray theory.

The results are presented in terms of the spatial distributions of the separated transfer functions for different dimensionless frequencies. This idea has been explored previously in (Jaramillo et al., 2012; Gomez et al., 2016) to find the solution to an arbitrary canyon under incident SH waves. However, in this work we describe the response in terms of the spatial variations of the amplitudes of the frequency-domain transfer functions along the free surface, for each independent term and aiming at finding the changes experienced by the incident field in terms of amplitude, duration, frequency content and spatial variability. We also study some extreme cases where it is shown that the diffracted field recovers the free-field motion at large distances from the scatterer, with the corresponding distance decreasing at low frequencies.

3.2.1 Method of analysis

The analysis technique used in the study of topographic effects in this work consists in separating the total field into independent geometrical and diffracted terms as stated by eq. (3.4)

$$u^T = u^{IN} + u_F^R + u^D \equiv u_F^0 + u^D \tag{3.4}$$

and where u^{IN} = incident field, u_F^R = field reflected over the free surface of the irregularity and u^D = diffracted field. In eq. (3.4), the optical field u_F^0, which results from the superposition of the incident and reflected rays $u^{IN} + u_F^R \equiv u_F^0$ is named by obvious reasons the physical incoming motion. In this work we compute u^T numerically and u_F^0 analytically using classical theory of rays. The term u^D is then simply obtained according to eq. (3.5);

$$u^D = u^T - u_F^0. \tag{3.5}$$

3.2.2 Geometric definition of the $V-$Shaped canyon and the $V-$Shaped hill

The canonical V-shaped canyon and hill topographies to be studied in this work are shown in fig. 3.6. Each shape is characterized by its slope angle θ and half-width a. The half-space has a propagation velocity for the shear wave c, mass density ρ and is under the action of a vertically incident SH-wave. The parametric study covers the set of parameters reported in table 3.1.

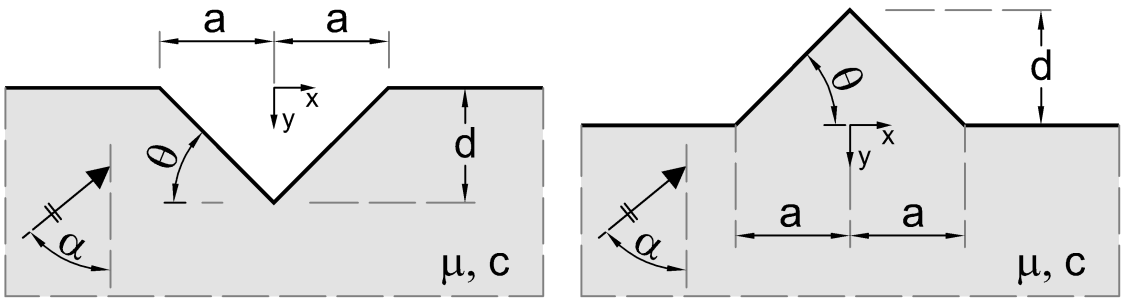

(a) (b)

Figure 3.6. Definition of the solution domains corresponding to the $V-$shaped canyon and $V-$shaped hill.

Case	θ	a	ρ	c
1	25°	0.25	1.0	1.0
2	45°	0.25	1.0	1.0
3	60°	0.25	1.0	1.0
4	25°	0.25	1.0	1.0
5	45°	0.25	1.0	1.0
6	60°	0.25	1.0	1.0

Table 3.1. Geometric and material parmeters defining the problems under study. Cases 1 through 3 correspond to the $V-$Shaped canyon, while cases 4 through 6 describe values for the $V-$Shaped hill.

3.2.3 Ray theory solution for the canyon and hill topographies

The ray theory solution for the topographies considered in this study is shown in fig. 3.7. Each family of rays has been labeled with an integer number. The incident front is indicated by ray 1. The dashed lines enclose zones of discontinuity of the optical field. According to the nature of the optical field in each case, we classify the studied topographies as gentle, moderate and strong. In the gentle topography, corresponding to cases 1 and 4, all the incident energy is reflected back into the half-space, while in the moderate scenarios, associated to case 2 in the canyon and case 5 in the hill, either part of the energy is reflected back into the half-space (canyon) or is trapped inside the scatterer (hill).

The case of strong topography is configured by the shapes 3 and 6. In the canyon, part of the energy is deflected by the scatterer surface towards a finite region of length L (see fig. 3.8) in the free surface of the half-space, while in the hill a large amount of energy remains trapped inside the scatterer in the form of rays traveling back and forth between the opposite slopes of the hill. The constant values appearing in the different regions in fig. 3.8 correspond to amplitudes of the response computed on the basis of the optical field according to:

$$L = \frac{d}{tan(2\theta - \pi/2)} - a$$
$$L_{ZONE2} = 2acos\theta$$
$$L_{ZONE3} = \sqrt{a^2 + d^2} - 2acos\theta$$

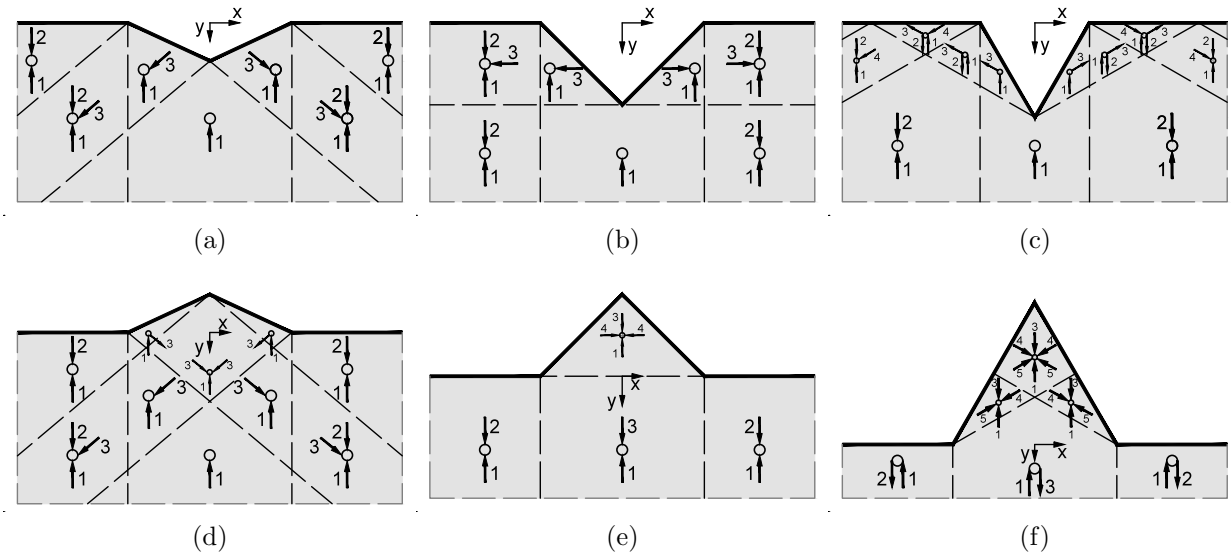

Figure 3.7. Ray diagrams for the canyon and hill topographies with geoetric parameters defined in table 3.1 a) Case 1, canyon with $\theta = 25°$ (Gentle topography) b) Case 2, canyon with $\theta = 45°$ (moderate topography) c) Case 3, canyon with $\theta = 60°$ (strong topography) d) Case 4, hill with $\theta = 25°$ (gentle topography) e) Case 5, hill with $\theta = 45°$ (moderate topography) and f) Case 6, hill with $\theta = 60°$ (strong topography)

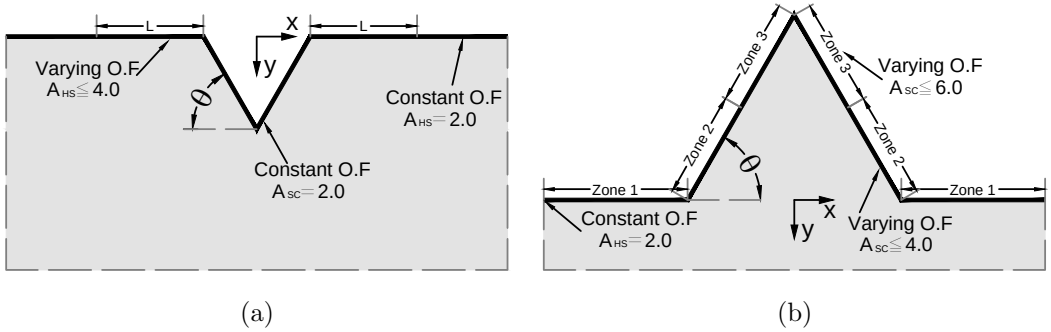

Figure 3.8. General solution to the problem of topographic site effects for a canyon and a hill. The labels A_{HS} and A_{SC} in each figure represent amplitude values over the free surface of the half-space and the scatterer respectively.

3.3 Results

3.3.1 Frequency domain response

The spatial distribution of the amplitude of the frequency domain transfer function along the free surface of the topographic irregularities is shown in fig. 3.9 and fig. 3.10 for different values of the dimensionless frequency $\eta = \frac{2a}{\lambda}$ where $\lambda =$ is the incident wave length. Each plot simultaneously shows the discontinuous field u_F^0, the total field

u^T and the diffracted field u^D. The set of rays existing in each part of the different domains determines the maximum and minimum amplitude of the optical field, while its spatial variation is determined by the addition of rays with different wave vectors. The geometrical field in cases 1 and 4 is obvious as two rays with equal phases are added over the free surface of the scatterer and half-space. In case 2, the incident and reflected fronts impinging against the canyon surface have the same phase and therefore lead to the constant amplitude value of 2.0. Now, the slope of the canyon causes the vertical incident front to divert horizontally, propagating parallel to the free surface of the half-space and away form the canyon. As a result the optical field in the half-space oscillates around the free-field solution with amplitudes between 3.0 and 1.0. In the hill of moderate topography, on the other hand, the incident rays and their reflections over the two slopes of the relief form a 4-rays-system that produces oscillations around the free-field solution with amplitudes between 0.0 and 4.0 depending on the value of η.

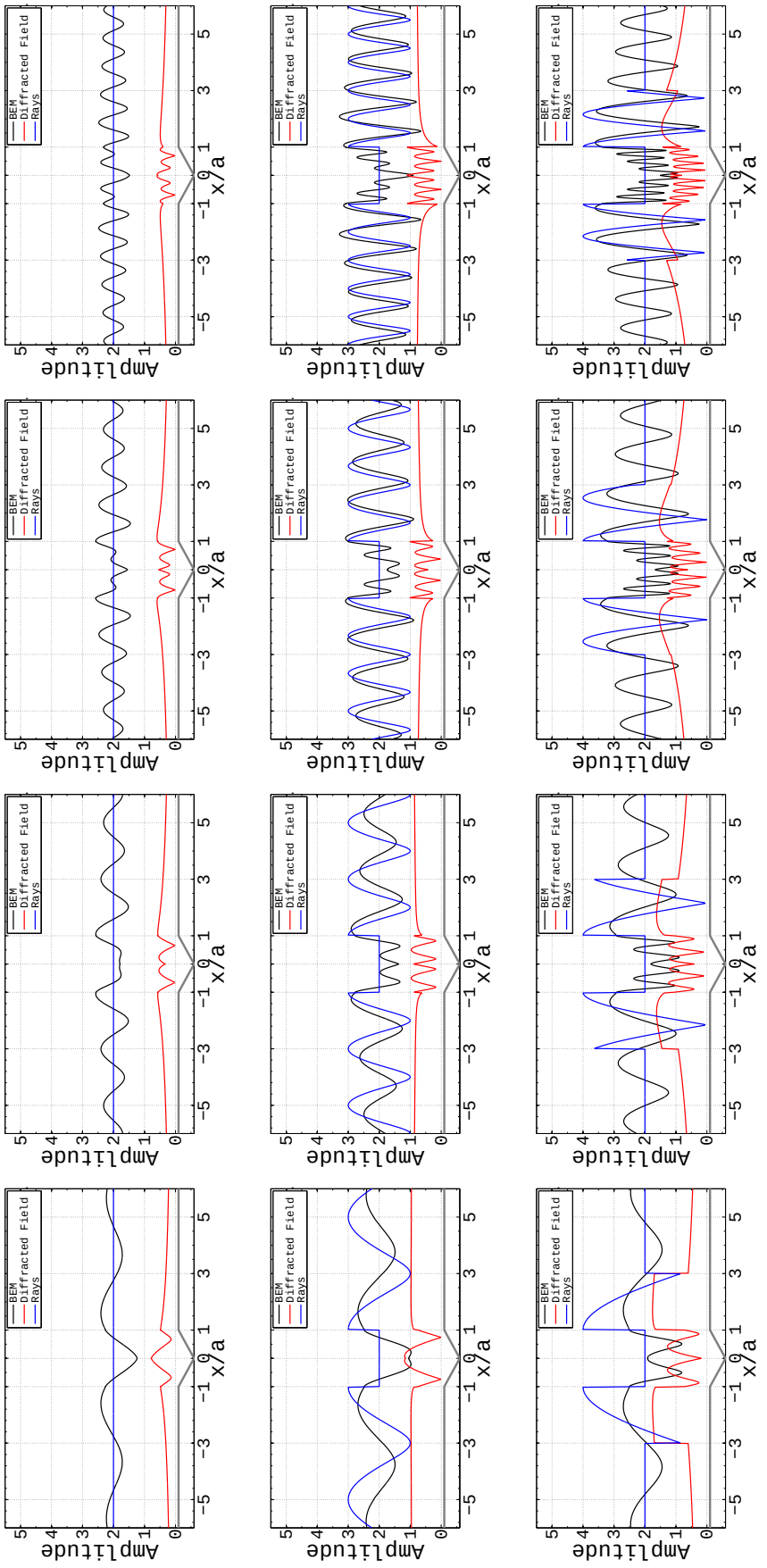

Figure 3.9. Frequency domain transfer function over the free surface of the $V-$shaped canyon topography. The results are organized as follows: (row 1) Gentle topography; (row 2) intermediate topography; (row 3) strong topography. Each column represents a different value of the dimensionless frequency parameter as follows $\eta = [0.5, 1.0, 1.5, 2.0]$.

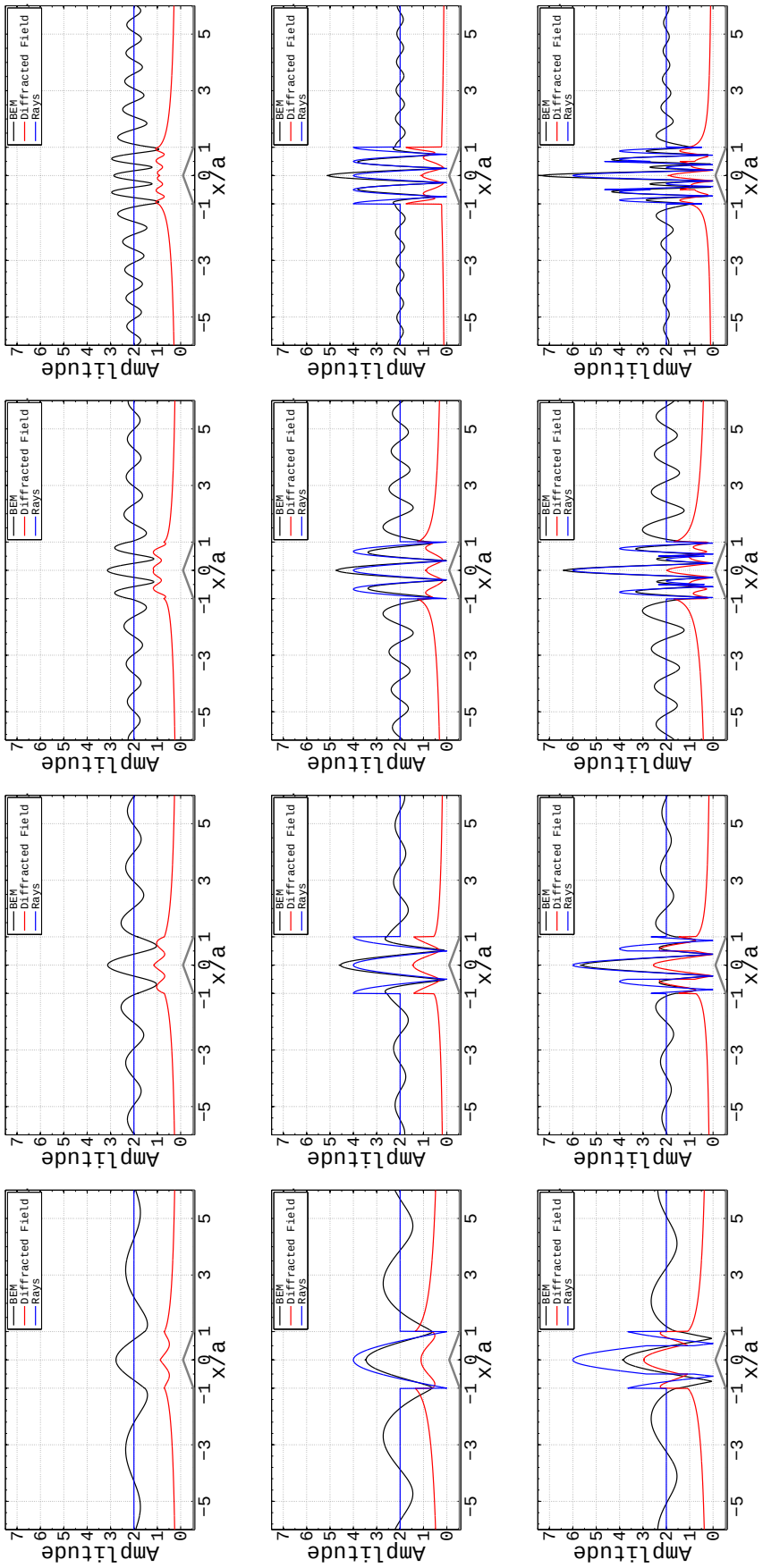

Figure 3.10. Frequency domain transfer function over the free surface of the $V-$shaped hill topography. The results are organized as follows: (row 1) Gentle topography; (row 2) intermediate topography; (row 3) strong topography. Each column represents a different value of the dimensionless frequency parameter as follows $\eta = [0.5, 1.0, 1.5, 2.0]$.

In the strong topographies of cases 3 and 6 there are two interesting scenarios. In the canyon, rays incident against the slopes are deflected against a finite zone of the half-space producing there a 4-rays-system. A similar behavior, with zones having a different number of rays as a result of the slopes occurs in the hill. In this last topography two systems with different number of rays are formed. These are schematized in fig. 3.11 with 4 rays in zone 2 and 6 rays in zone 3. As a result, depending on the value of η, two different systems of oscillations exist over zones 2 and 3, with amplitudes of 4.0 and 6.0 respectively.

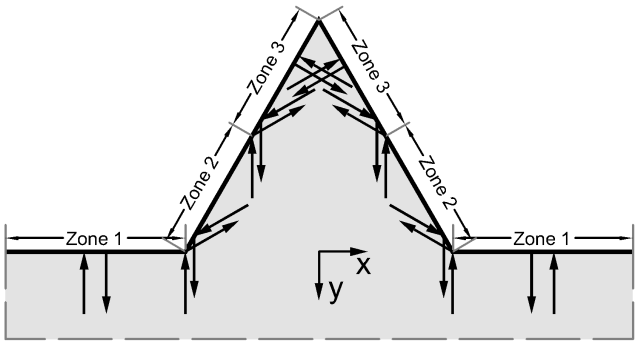

Figure 3.11. Distribution of rays along the different zones-Case 7.

The maximum amplitudes predicted on the basis of the number of rays in each part of the surface are summarized in table 3.2.

Case	θ	Half-space	Scatterer
1	25°	2.0	2.0
2	45°	3.0	2.0
3	60°	4.0	2.0
4	25°	2.0	2.0
5	45°	2.0	4.0
6	60°	2.0	6.0

Table 3.2. Maximum amplitudes for the optical field over the free surface of the half-space and scatterer in the V-shaped canyon and hill topographies.

On the other hand, the diffraction term u^D produces spatial variations in the total solution via the out-of-phase sources located at the corners of the topographic irregularity. This modification is specially important in the regions of constant optical field, like in the scatterer surface for the canyon topographies and over the free surface of the half-space in the hill topographies. Those modifications are stronger in the low frequency regime. Such behavior is observed in cases 1 and 4 where all the spatial variation is due to the diffraction field. In the canyons of cases 2 and 3 the response in the free surface of the half-space in the high frequency regime is dominated by the optical field. By contrast, the diffraction field dominates the amplitude and spatial variation over the

scatterer surface. In this same topography the diffracted field exhibits spatial variations over the scatterer surface and over a finite region of the half-space.

In order to develop understanding of the role played by the diffracted field upon the topographic effect it is important to explain the mechanisms that produce the spatial variations of the response. These variations over the scatterer surface can be understood like the result of rays with opposite wave vectors emanating from the sources of diffraction located at the top and bottom of the canyon. This spatial variation depends on the dimensionless frequency parameter $\alpha = \ell/\lambda$ where ℓ is the length of the slope (equivalent to the distance between diffraction sources). On the other hand, the oscillations over the half-space are due to the rays that emanate from the bottom and right apex of the canyon. These rays hit the free surface at angles whose value decreases as the distance from the scatterer increases. In the limit the angle becomes null turning into a ray that propagates parallel to the one originated at the top source. This mechanism is explained in fig. 3.12 where we plot independently the response corresponding to each one of the diffraction sources and their superposition which is the same function displayed in fig. 3.9. It is interesting to observe from fig. 3.12a how the superimposed function exhibits oscillations over the scatterer and half-space surface even when the independent contributions from each source are smooth functions. In fig. 3.12b we also plot the angle of each incident ray emanating from the bottom source versus the distance over the half-space. It is clear how as this angle approaches the constant null value the transfer function approaches the constant stabilized value free of oscillations. The distance at which the free-field is eventually recovered depends on the canyon depth.

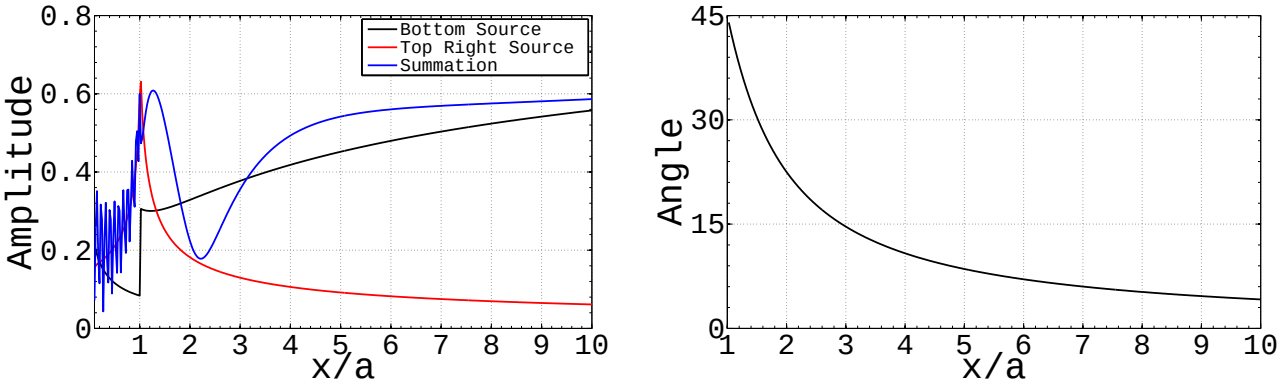

(a) (b)

Figure 3.12. Amplitude of the diffracted field over the scatterer and half-space surface due to the bottom and right apex a) η =8.0 b) Angle of ray emanating from the bottom.

3.3.2 Reconstruction of the free-field response

This section focuses on the mechanisms by which the diffracted field acting over the geometric solution restores the free-field solution in the far-field of the studied scatterers.

In order to explain the response at the two extreme cases of low and high frequency we use the analysis method described in Jaramillo et al. (2012), where the diffracted field is built via superposition of contributions from different sources and diffraction events. In that technique the scatterer surface is approximated by the superposition of fundamental wedges, each one contributing with a source of diffraction. The field from each source is then assumed to behave as a ray with an associated diffraction coefficient computed following the techniques from the geometrical theory of diffraction Keller (1962). This aspect of the response is explained with respect to the $\theta = 45°$ canyon shown in fig. 3.13. The rays marked as 1, 2 and 3 represent the reflected optical field, while the dashed lines define its respective reflection boundaries and shadow zones. Note that there are 3 diffracted waves consistent with the three wedges forming the canyon.

As discussed in the previous section, regarding the response of the semi-infinite wedge, along the incidence and reflection boundaries the diffracted field takes a sign, with respect to the plane front, which is opposite in the illuminated zone and equivalent in the shadow zone. At the same time, as the distance from the diffraction source increases the diffracted field reaches a constant limit value equal to half the amplitude of the plane front. Hence, for a plane front of unit amplitude, the diffracted field is equal to $\pm 0.5e^{-ikr}$. These values and its corresponding signs are shown in the figure adjacent to each boundary. The reconstruction of the far field response corresponding to the full recovery of the wave fronts propagating vertically is reached by the superposition of the two diffracted rays emanating from each one of the top corners of the canyon. These contribute with a total amplitude for the diffracted field $u^D = 0.5 + 0.5 \equiv 1.0$ in the far-field.

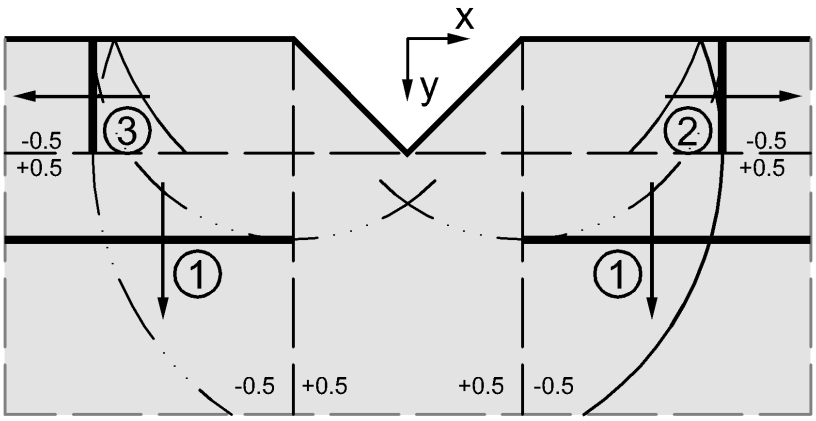

Figure 3.13. Schematic description of the process upon which the incoming field is recovered as a far field boundary condition by the diffracted part of the response for the $\theta = 45°$

Similarly, the wave front reflected at the slopes and propagating horizontally is depleted in the far field by the diffracted field produced by the wedge forming the bottom corner

of the canyon. Upon reflection over the free boundary this diffracted front doubles its amplitude reaching the limit value of 1.0 eliminating the reflected front. These limit values of the response are also clarified in fig. 3.14a and fig. 3.14b. The first plot shows the contribution from the left source of diffraction measured over a vertical line drawn from the right corner. Note that inside the zone of discontinuity of the plane front, the diffracted field approaches the constant value of $0.5e^{-ikr}$ which added to the contribution from the opposite source and the symmetry of the problem, results in a unit amplitude which smooths out the discontinuity in the infinite plane front. This limit is approached faster at low frequencies, which is an intuitively obvious result that indicates that a receiver located inside the domain is less aware of the presence of the scatterer at lower frequencies. Similarly, fig. 3.14b shows the contribution from the bottom source of diffraction over the free surface of the half-space drawn from the right corner. The value of 1.0 reached upon reflection of this diffracted ray along the free surface is shown at different frequencies. As in the previous case it is also clear how this free-field condition is recovered faster by the diffracted field at low frequencies.

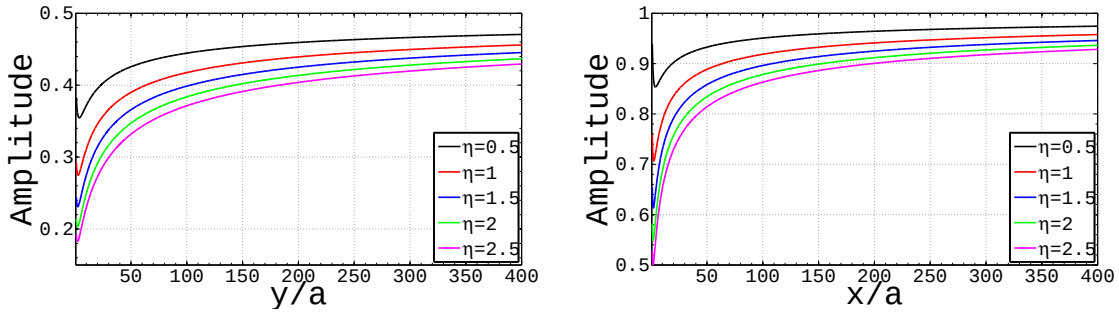

(a) (b)

Figure 3.14. Amplitude of the diffracted field in the $\theta = 45°$-canyon for different values of η. a) Over a vertical line b) Over the free boundary.

For completeness the family of reflected and diffracted rays for all the considered canyons is shown in fig. 3.15.

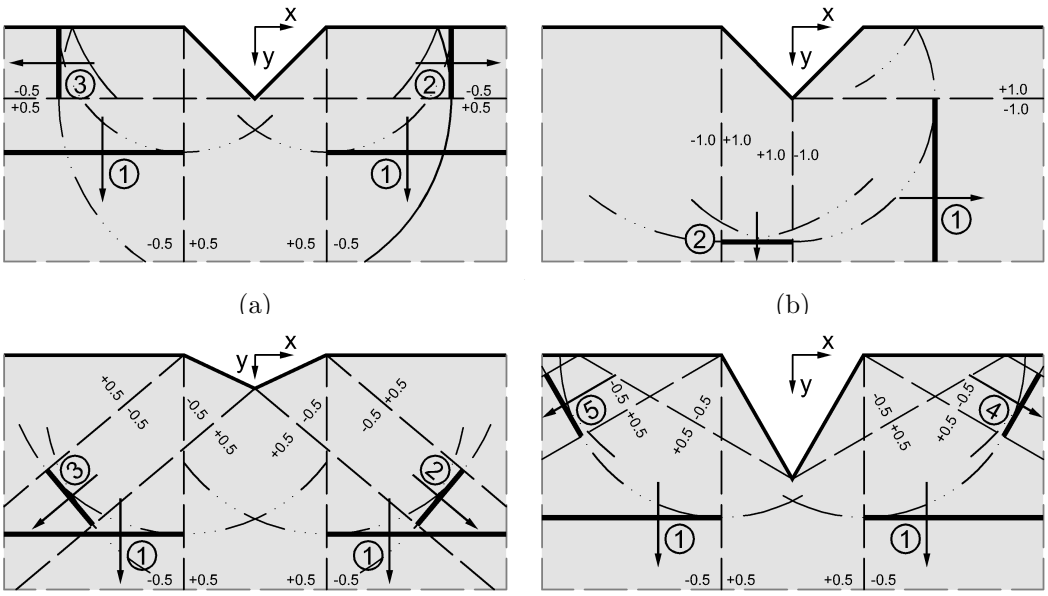

Figure 3.15. Schematic description of the process upon which the incoming field is recovered as a far field boundary condition by the diffracted part of the response.

3.3.3 Spectral response

This section focuses in the response of the $\theta = 25°$ canyon and hill shown in fig. 3.16. The response, in terms of the frequency domain transfer functions along the 6 receivers in each case is shown in fig. 3.17.

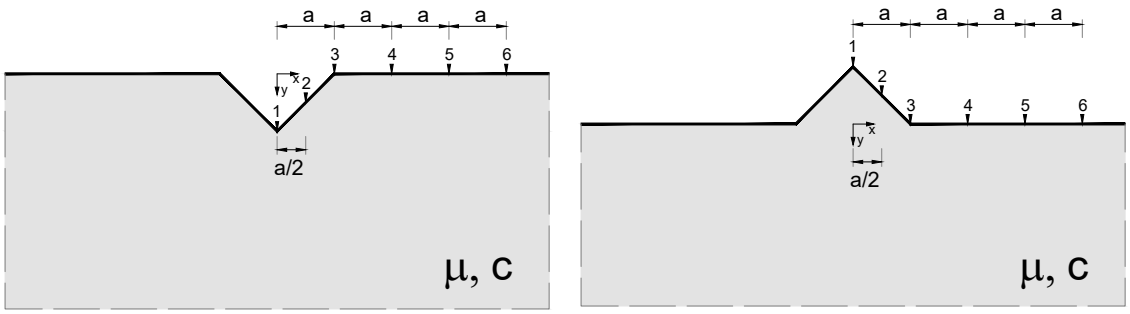

Figure 3.16. Definition of receivers for calculation of the response spectra along the free-surface of the $\theta = 25°$-V-shaped canyon and $\theta = 25°$-V-shaped hill topographies.

Point 1 for the canyon exhibits de-amplification consistent with energy defocusing towards the interior of the half-space. The response of point 2, located over the slope, is similar to that in a half-space with a minor topographic effect. Topographic effects are

stronger at the diffraction source 3 and they extend to the remaining receivers located over the free surface of the half-space where the response exhibits an amplification-deamplification pattern around the reference half-space solution. In the hill, maximum amplification (and hence topographic effect) occurs at the crest over observation point 1. At point 2 inside the hill there is still some amplification while the topographic effect decreases at the receivers located along the free surface of the half-space. In summary, topographic effects for the canyon take place along the adjacent half-space surface while the response is reversed for the hill where the geometric effects occur inside the topographic formation.

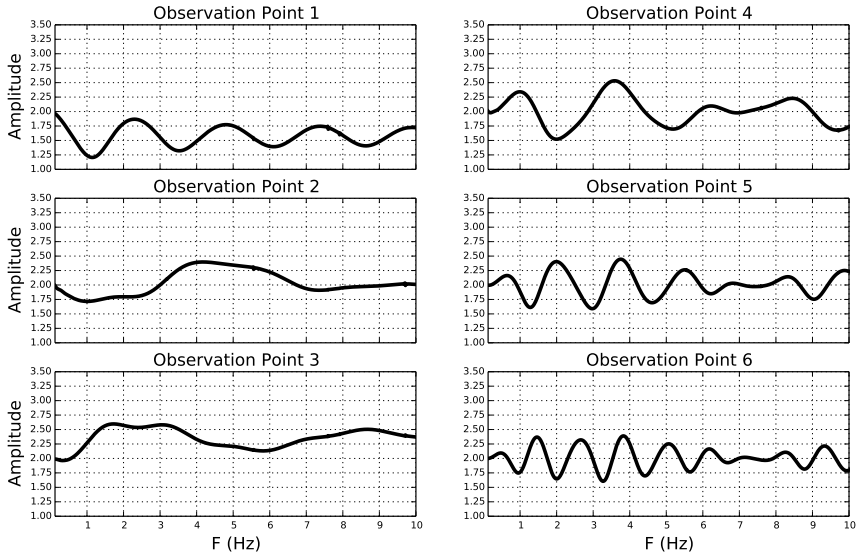

(a)

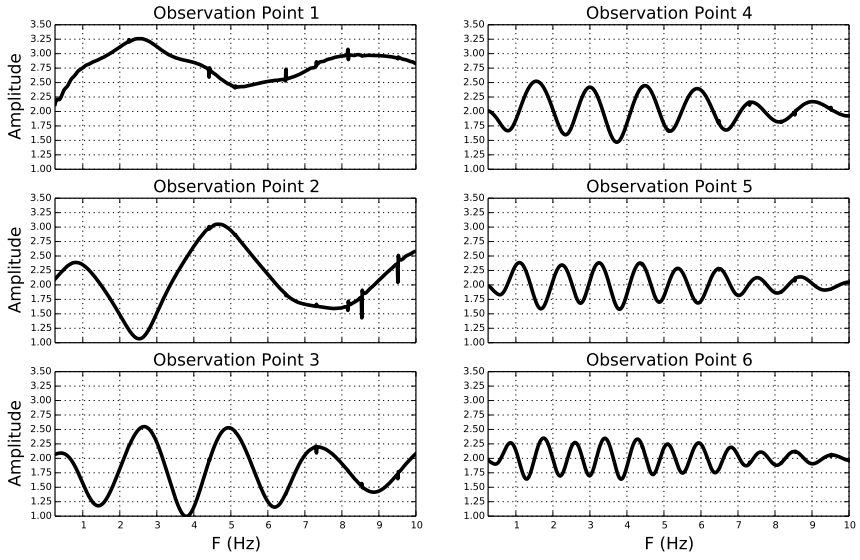

(b)

Figure 3.17. Transfer functions along the 6 receivers shown in fig. 3.16 for the $\theta = 25°$-V-shaped hill and canyon.

As an additional response characterization the spectral displacements resulting from three ground motions with Fourier spectra shown in fig. 3.18 are displayed in fig. 3.19. Each plot contains a set of 4 results corresponding to the ratio of the response spectra for the 3 considered motions with respect to the incident field and the frequency domain transfer function expressed in terms of the structural period. It is interesting to observe that the transfer function and the corresponding ratio of response spectra are strongly connected. This particular form of the response leads directly to the concept of topographic aggravation factor followed in code approaches.

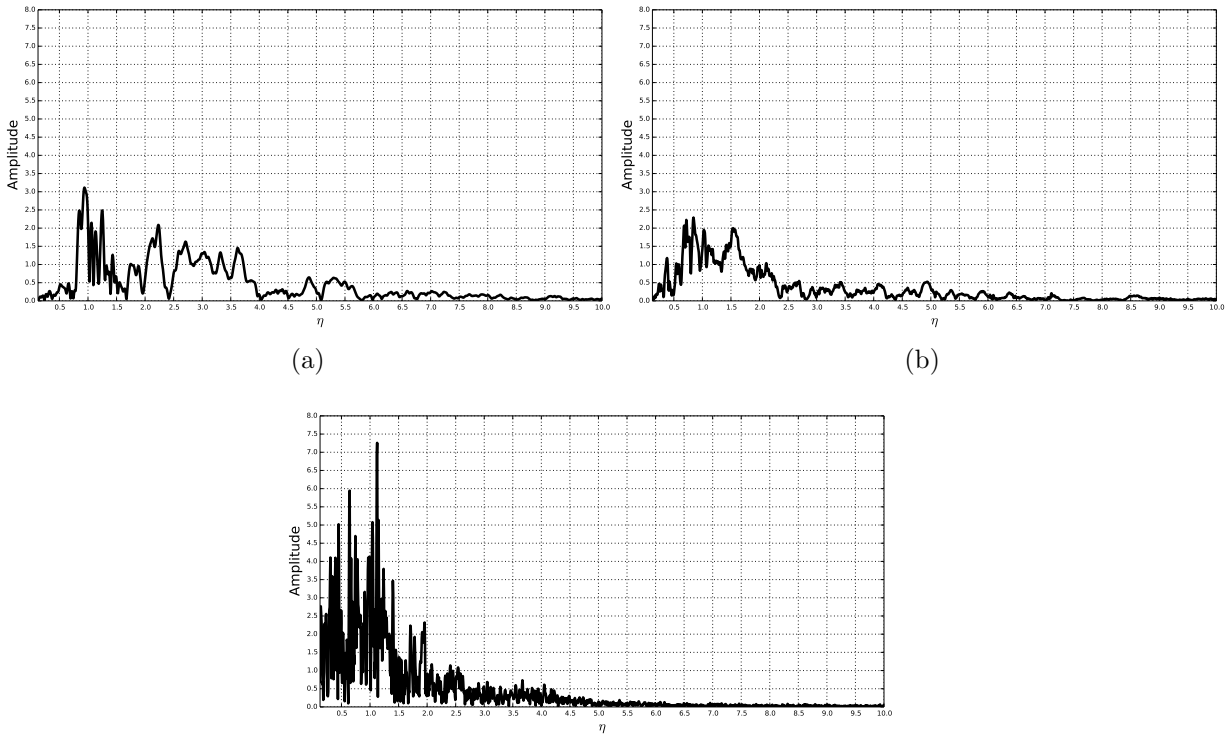

Figure 3.18. Fourier amplitude spectra for the ground motions considered in the spectral response of the studied topographies .

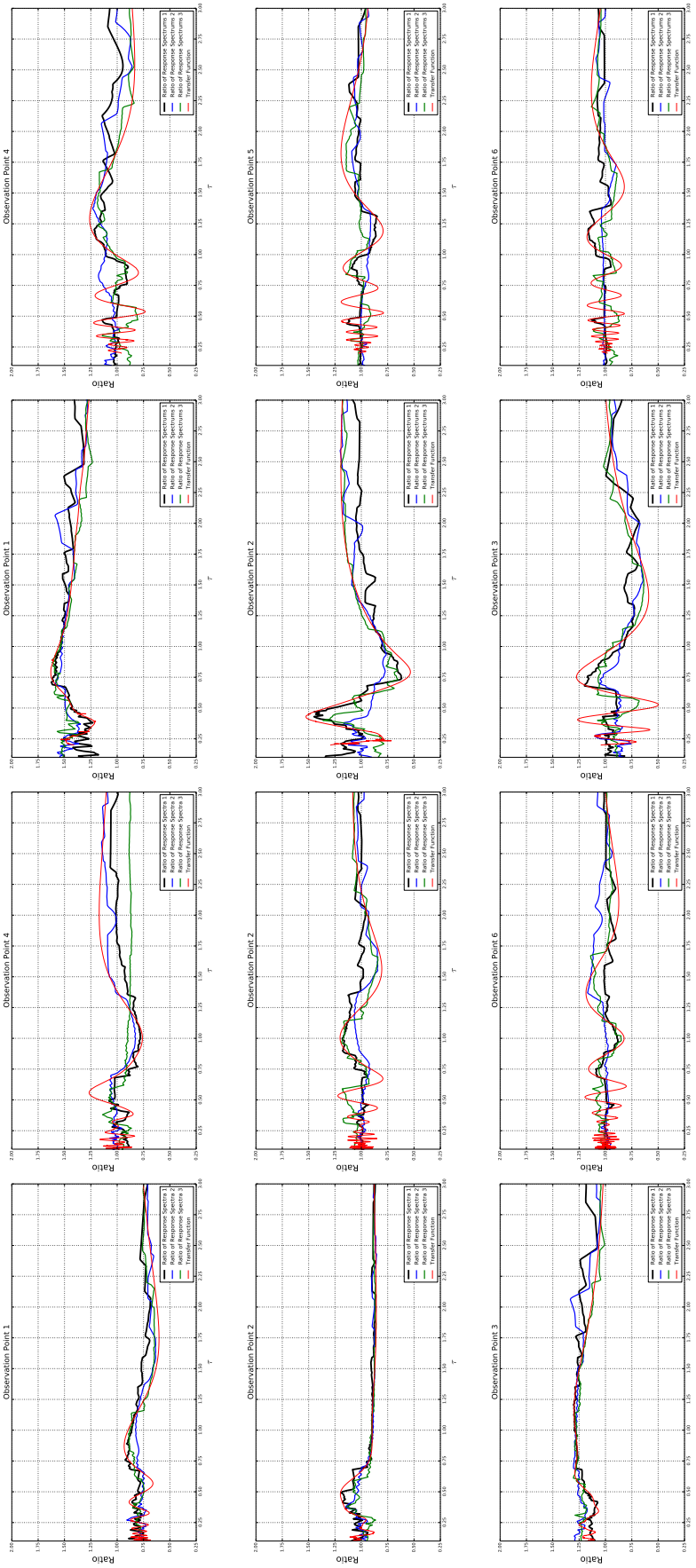

Figure 3.19. Spectral Relations along the 6 receivers shown in fig. 3.16 for the $\theta = 25°$-V-shaped hill and canyon.

Figure 3.20 and fig. 3.21 show the acceleration response spectra at the 6 receivers shown in fig. 3.16 for the 25^0 canyon and hill geometries. Every spectral response has been discriminated into free-field solution (or half-space solution), diffracted solution and total solution. The diffracted response was obtained with the transfer function from the diffracted field together with the Fourier spectra for the input signal. From these plots it is observed that from the spectral point of view the topographic effect is not as strong as inferred from the analysis in the frequency domain. In fact, the acceleration spectral response indicate that in this case the topographic effects are localized at points 3 and 1 in the canyon and hill respectively.

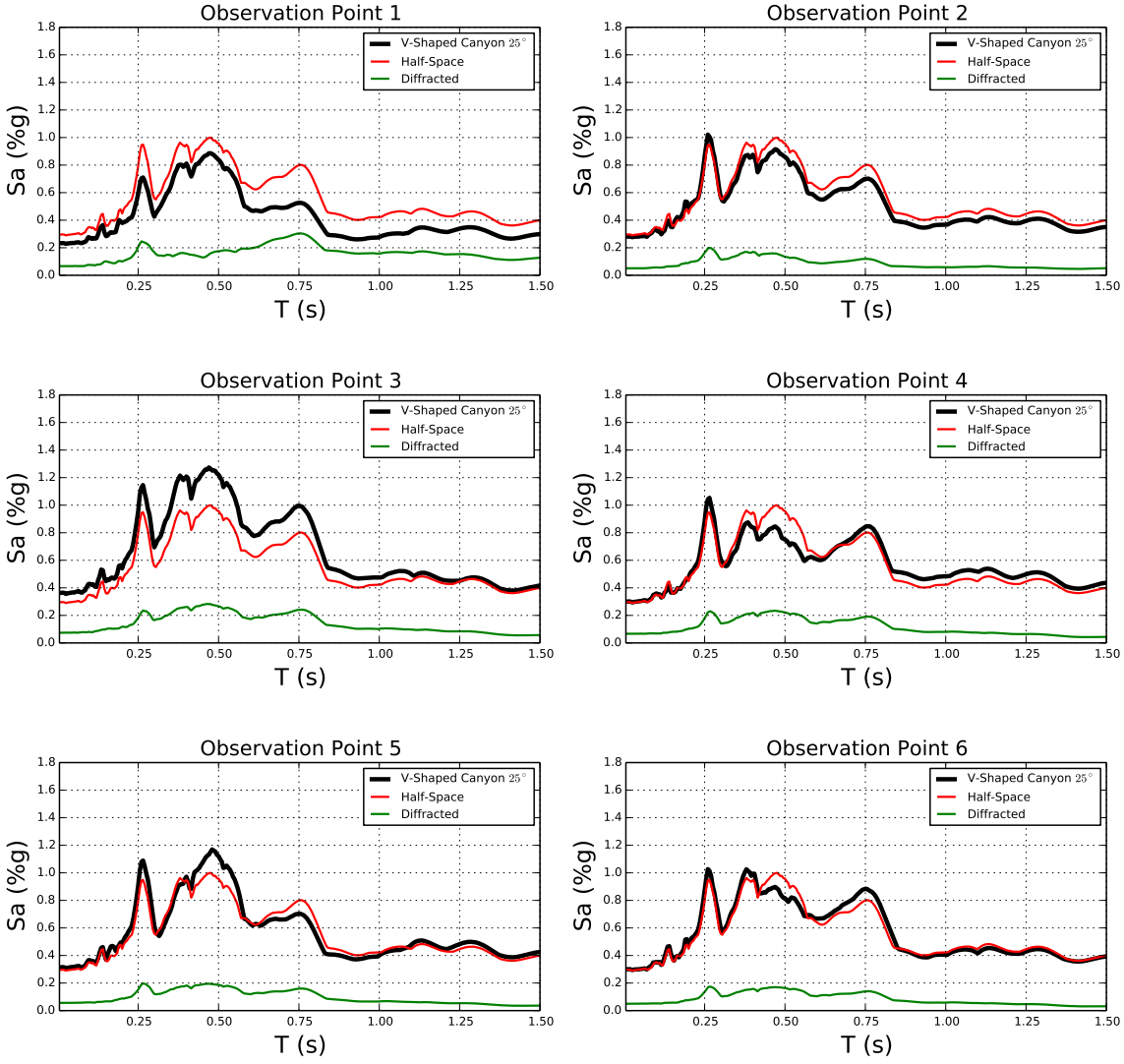

Figure 3.20. Acceleration response spectra at the 6 receivers shown in fig. 3.16 for the $\theta = 25°$-V-shaped canyon (time signal 3).

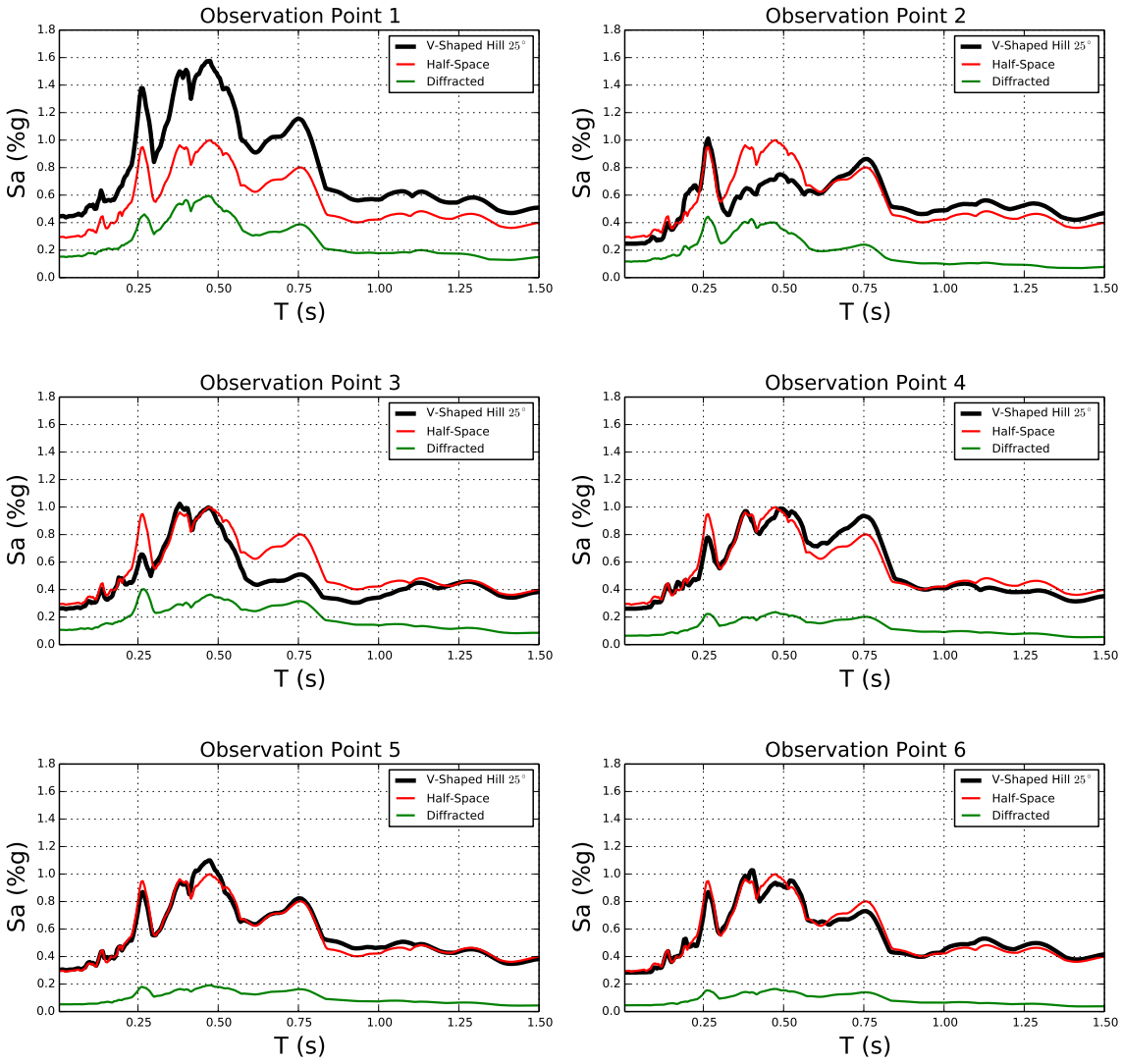

Figure 3.21. Acceleration response spectra at the 6 receivers shown in fig. 3.16 for the $\theta = 25°$-V-shaped hill (time signal 3).

Conclusions

This chapter has studied the effect of the diffracted field on the response of two canonic topographic irregularities. It discusses the most relevant aspects of diffracted waves produced by a corner singularity in a semi-infinite wedge. The results for this fundamental solution, and particularly, the limit values reached by the diffracted field at reflection boundaries have been used to explain interesting phenomena such as the recovery of remote boundary conditions on scattering problems defined by localized topographies. From the point of view of possible topographic effects the frequency domain results have shown the spatial variation of amplification and deamplification patterns. These results have also shown a strong similarity between the transfer function and the ratio of

response spectra. The final part of the chapter also shows the spatial distribution of acceleration response spectra where it is identified that in spectral terms the topographic effect is weaker than its frequency domain description.

Chapter 4

Size-conditioned-response-spectra

Introduction

This chapter describes the main contribution in this work. After having identified the wedge as the fundamental geometric element in a topographic profile we propose a method to address topographic effects from an engineering perspective. It focuses on identifying the minimum dimensions of a model intended for site response analysis if one is interested in considering topographic effects up to a prescribed value of the structural period. The problem is addressed based on the ideas of Sáenz et al. (2019) who proposed a rational method to smooth the topographic profile at the expense of loosing accuracy in the spectral response below a certain target period. In that contribution the result is then provided in terms of a topography-dependent-response-spectra (TRS). By contrast, this work proposes an additional extension to these methods but now based on truncating those topographic accidents that in advance, are known to be irrelevant in the response for structural periods above a prescribed target value. The resulting zone of accurate structural periods corresponds to the high frequency range for which the eliminated topographic accidents are considered infinitely far from the site of interest. The response resulting from this size-limited model is thus termed size-conditioned-response-spectra (SCS).

To identify the irrelevant geometric features associated to a target period we used the distance-decay-effect experienced by diffracted waves generated at singularities of the topographic profile. This controlling aspect of the response is studied through parametric analysis of a working model corresponding to a trapezoidal canyon under vertically incident (SH and SV) plane waves. The analysis yields cut-off frequencies at which the contribution from the diffraction source at a distance L_w may be considered negligible. These frequencies allow us to propose a simple expression to compute the minimum size of the required topographic model. The resulting local topographies are then termed reduced models.

The accuracy and usefulness of the proposed technique is later verified in a study of an artificial model built out of a cross section of the Aburrá Valley region in Medellín,

Colombia, Restrepo et al. (2016). For this scenario we computed the exact and approximate response at 6 different sites of interest. Results, which are given in terms of spectral ratios between the approximate and the exact response, show the expected accuracy even at values of the structural period slightly larger than the target value. As an additional exercise, the resulting reduced models were also further simplified after applying the smoothing algorithm proposed by Sáenz et al. (2019). This step generates reduced models with geometries resembling those considered in the formulation of TAFs in code-based regulations. The combination of size and shape results in response spectra valid within a relatively well defined period range or with acceptable accuracy starting from a minimum period, defined by the level of smoothness, and extending up to a maximum period defined by the size of the local model.

The chapter is organized as follows. In the initial section, after this introduction, we present the concept of a size-conditioned-response-spectra with regards to an arbitrary and schematic topographic profile. That discussion shows that a fundamental parameter in the spectral response at a site of interest is the distance between adjacent diffraction sources and the site of interest. The chapter continues with the frequency domain based parametric analysis of the distance parameter in terms of the amplitude of the transfer function for our working model of a symmetric trapezoidal canyon. The final two sections in the chapter contain the results, in terms of the conducted verification exercises, and the conclusions and activities for further work.

4.1 Spectral response at a site of interest within a topographic profile

Figure 4.1a depicts an sketch of a topographic profile formed by the combination of a V-shaped canyon and a hill supported by an elastic half-space and subjected to a vertically incident plane wave. Green dots in this model highlight the location of geometric singularities which produce diffracted waves once are hit by the impinging incident field (Jaramillo et al., 2012; Gomez et al., 2016; Asimaki & Mohammadi, 2018). Point R (shown in red), located on the slope, represents a site of interest where topographic effects are to be considered.

The fundamental problem addressed in this work is that of finding the minimum portion of the full topographic profile (fig. 4.1a) that must be included in a model if we wish to find the spectral response at the site of interest up to a prescribed value of a target structural period T^{tar}. This idea is emphasized by the schematic spectral plots shown in the right part of the figure and which are partially shaded up until T^{tar}. Each one of these limited response spectra, and its limiting period T^{tar}, is associated to a reduced model of decreasing size as highlighted by the thick lines surrounding point R in each case (fig. 4.1 b-d). Note that sources of diffraction are incrementally removed from the model after each subsequent truncation. Thus, each continued simplification generates also a continuing loss in accuracy in the spectral response marked by the location of T^{tar}. This is precisely the main concept behind our proposed idea: it indicates that as we remove diffraction sources, and thus decrease the size of the reduced model, we also

introduce a shift toward lower values of the target period T^{tar}.

To address the fundamental question regarding the determination of the minimum required model we rely on arguments from the geometrical theory of diffraction (Keller, 1956, 1962; Kouyoumjian & Pathak, 1974) according to which, the total field U^T at R can be separated into an optical component U^O and a diffracted term U^D like:

$$U^T = U^O + U^D. \tag{4.1}$$

This separation of the field components has already been identified by several authors in the context of seismology and earthquake engineering, (Sánchez-Sesma, 1985; Valencia et al., 2017). Note that each source of diffracted waves corresponds to a geometric or corner singularity appearing in the topographic profile. The singularity appears in the form of a finite wedge configured by the interception at a point of two adjacent plane surfaces: hence, the diffracted field associated to the wedge is a key element in the response of a topographic profile. Closed-form solutions for the total field generated by a profile of arbitrary shape built through the superposition of convex and concave wedges have been obtained by Jaramillo et al. (2012).

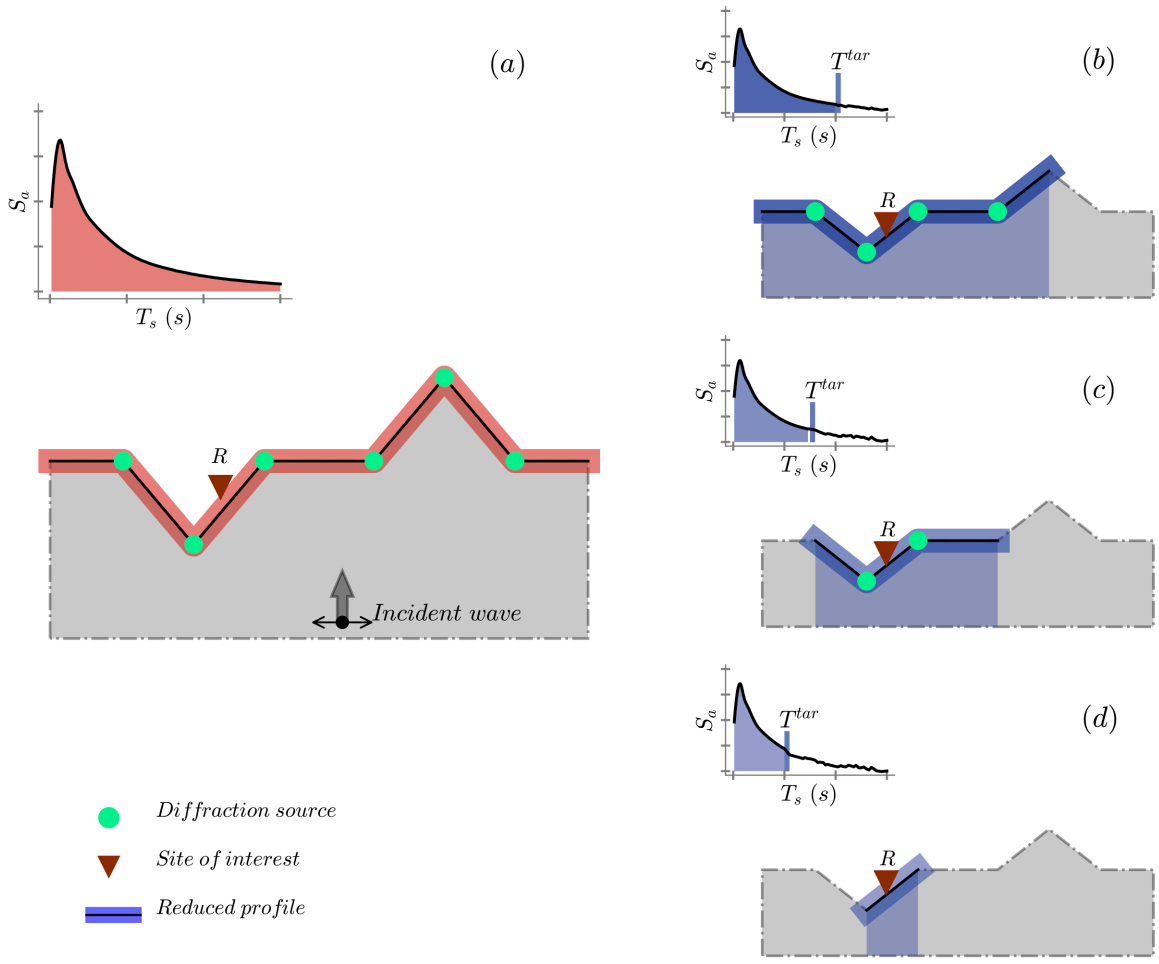

Figure 4.1. (a) Schematic representation of an arbitrary topographic profile with combined convex and concave features. The green dots are geometric singularities which produce diffracted waves after interacting with incident fields. The fully shaded response spectra shown at the left(top) represents the motion at the site of interest (red triangle) resulting from analysis of the complete model. (b)-(d) Size-conditioned-response-spectra at the site of interest and resulting from analysis of the reduced models is shown at the right. Each partial model is comprised by the thick light blue lines. Note that the range of valid structural periods in the response spectra decreases as the model becomes simpler.

Although the optical field U^O, which corresponds to the incident front and its reflections at free boundaries, affects the response at R, its contribution is easy to calculate since it depends only upon the angle of incidence. In contrast, the diffracted field U^D is associated to the presence of geometric singularities and subsequently to topographic effects.

According to the solution of an infinite wedge subjected to horizontally polarized shear waves (Kouyoumjian & Pathak, 1974), the amplitude of the diffracted waves originating at the corner singularity decays with distance. Furthermore, as will be shown later in

this chapter, the number of wavelengths required for a diffracted wave of frequency f, propagating at a speed β, to decay below a given reference value is constant. Such unique signature of the diffracted field naturally suggests that a controlling parameter dominating the response at R is the distance between the geometric singularities present in the topographic profile and the site of interest. If the nearest source of diffraction from the receiver point R is located at a distance ℓ, then the topographic contribution from this source at R depends on whether or not the diffracted waves have died out as they travel along the distance ℓ.

To explore the effect of the distance parameter on the response, we start from the concept of topography-conditioned-response-spectra (TRS) introduced by Sáenz et al. (2019). That work considers the complete topographic profile but instead of reducing its total size, it computes a period-limited spectral response which results after simplifying the shape of the topographic profile. Here we propose an additional simplification, not based on eliminating small-length features from the model, but on decreasing its total size. The resulting response is therefore termed a size-conditioned-response-spectra (SCS).

The connection between the range of accuracy in the SCS and the reduced models had already been illustrated in fig. 4.1. Note there that the full response is captured by the regional model shown in the top part of the figure. The main highlighting feature of this representation is the inability of the reduced models to capture the low frequency response as the size of the topographic profile decreases. Longer wavelengths associated with larger periods are expected to arrive with important amplitudes at the site while higher frequency, short wavelengths, die out faster. It is evident that diffracted waves play a key role on the topographic effect.

4.1.1 Parametric response of a source of diffraction

We now study the response of a source of diffracted waves through a parametric analysis conducted in the frequency domain. The study is aimed at capturing the distance-frequency relation for diffracted waves generated at corner singularities. Our main goal is to identify the distance at which the amplitude of the transfer function of a diffracted wave of frequency f decays below a predefined threshold value. The fundamental source of diffraction is shown in the schematic representation of fig. 4.2 where the corner singularity is defined by the green point marked as D, while point R is an observation site where the response is going to be measured. Note that the singularity is formed by the interception of the continuous line, containing the observation point at a distance L_w, and the infinite dashed line extending to the left. These two lines intercepting at D form a wedge which is infinite unless it becomes bounded by further interceptions with other plane surfaces.

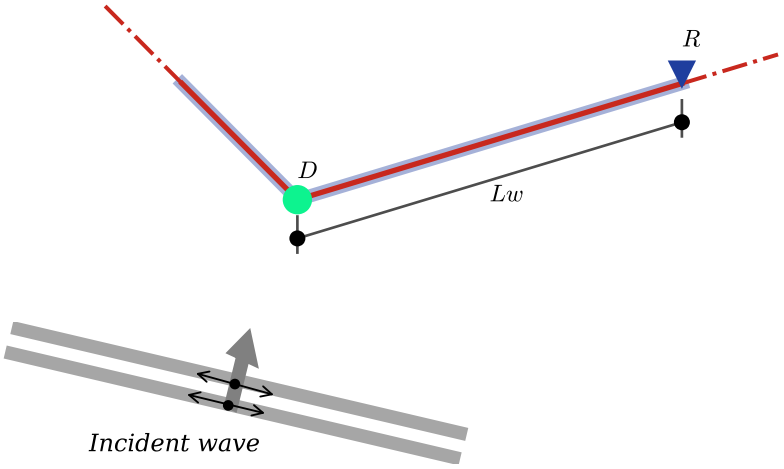

Figure 4.2. Generalized source of diffraction at point D and at a distance L_w from the site of interest R. The source of diffraction is conformed by the plane surfaces meeting at the corner point D forming a wedge.

To solve modelling issues related to our numerical scheme, the source of diffraction is placed within a simple working model of a topographic profile conformed by the symmetric trapezoidal canyon shown in fig. 4.3. The canyon, which is subjected to vertically incident SH and SV waves contains two sources of diffraction, marked as D_1 and D_2, conformed by the interception of the plane surface forming the bottom of the canyon, with the flat, inclined surfaces completing semi-infinite wedges at each side. The distance between sources is of 5.0 km and the observation point R is located half-way through it, right at the middle of the canyon. The trapezoidal shape facilitates imposition of the plane wave excitation within the implemented numerical formulation and at the same time allows the consideration of diffraction sources formed by wedges of different angles. Note that this model is convenient for the numerical analysis as it allows us to simultaneously incorporate diffraction sources of various angles and at the same time apply an exact plane wave excitation. In this study we considered values of $\alpha = [20°, 30°, 45°]$ and material properties corresponding to a shear wave propagation velocity $\beta = 1.0$ km/s, a Poisson's ratio $\nu = 1/3$ and a damping ratio of 3% (which is equivalent to a quality factor of $Q \simeq 16.5$). The selected value of damping should cover a wide variety of cases of average velocities for the profile of the surface earth crust, including soft soil deposits. The value of 3% is the one suggested in (EPRI) and corresponding to the average damping for the soil profile for small strains that reproduces reasonably well site amplifications at the reference Gilroy 2 site. For sites comparable to Gilroy 2 the dimensions of the reduced model are those reported in this work; however one must realize that our approach being strongly dependent on the assumed value of attenuation would lead to other dimensions in sites with damping values that may be larger or smaller with respect to the 3 % value.

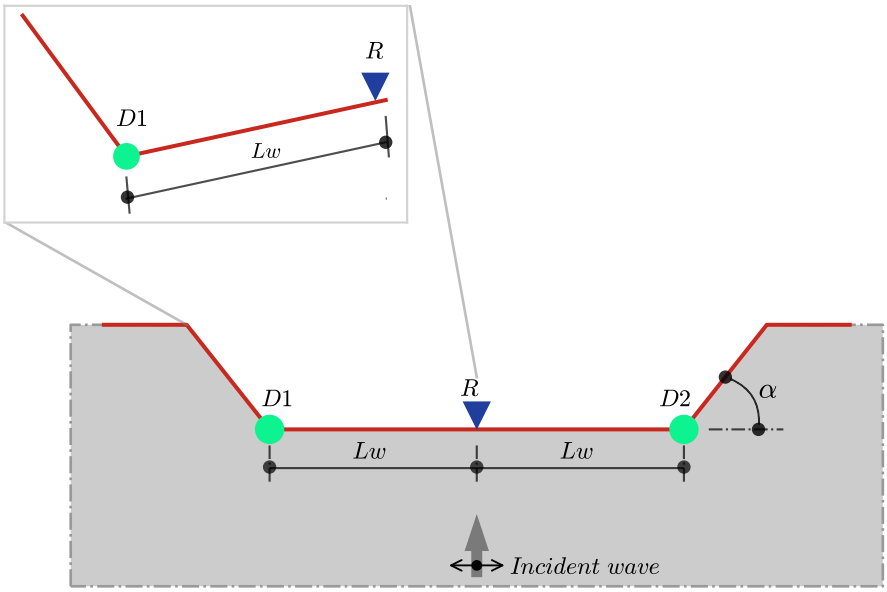

Figure 4.3. Working model used in the parametric study of the distance-decay effect of diffracted waves. The canyon shape has been used to embed diffraction sources like the one shown in the inset. The sources of diffraction are indicated by the green dots and the site-of-interest is represented by the blue triangle. All the analysis were conducted for a shear wave propagation velocity $\beta = 1.0$ km/s, damping factor $\xi = 3\%$ and Poisson's ratio $\nu = 0.3$.

The frequency domain parametric analysis was conducted using an in-house implementation of the direct boundary element method with exact consideration of radiation conditions at the remote boundaries of the half-space, Banerjee & Butterfield (1981) —a validation of the code is available in Gomez et al. (2013)—. In each considered model we obtained the amplitude of the transfer function over the frequency range $f = [0.01 - 10.0]$ Hz at the receiver point R and corresponding to the total field U^T. The main purpose of the analysis is to identify the frequency-dependent-length at which the amplitude of the transfer function approaches values equivalent to the half-space solution ($\mid TF^o \mid = 2.0$). However, since the problem is frequency dependent we have maintained the distance L_w constant in our simulations and instead identified the cut-off frequencies at which this condition is reached. To specify the half-space limit we assumed that the diffraction effect is negligible whenever the amplitude $\big|\big|TF^T\big| - |TF^o|\big|$ decays below a threshold value of 0.1. In this sense the cut-off frequency f_c corresponds to the frequency associated to the $\big|\big|TF^T\big| - |TF^o|\big| = 0.1$ condition.

The complete set of results for all the considered slope angles α and incident waves are shown in fig. 4.4. These plots show the amplitude of the transfer function for the total response at the receiver point R. The shaded horizontal band marks the $\big|\big|TF^T\big| - |TF^o|\big| \leq 0.1$ threshold. Similarly, the vertical shaded band indicates the inaccurate frequency range defining also the cut-off frequency above which the diffracted wave field has minor effect in the total response.

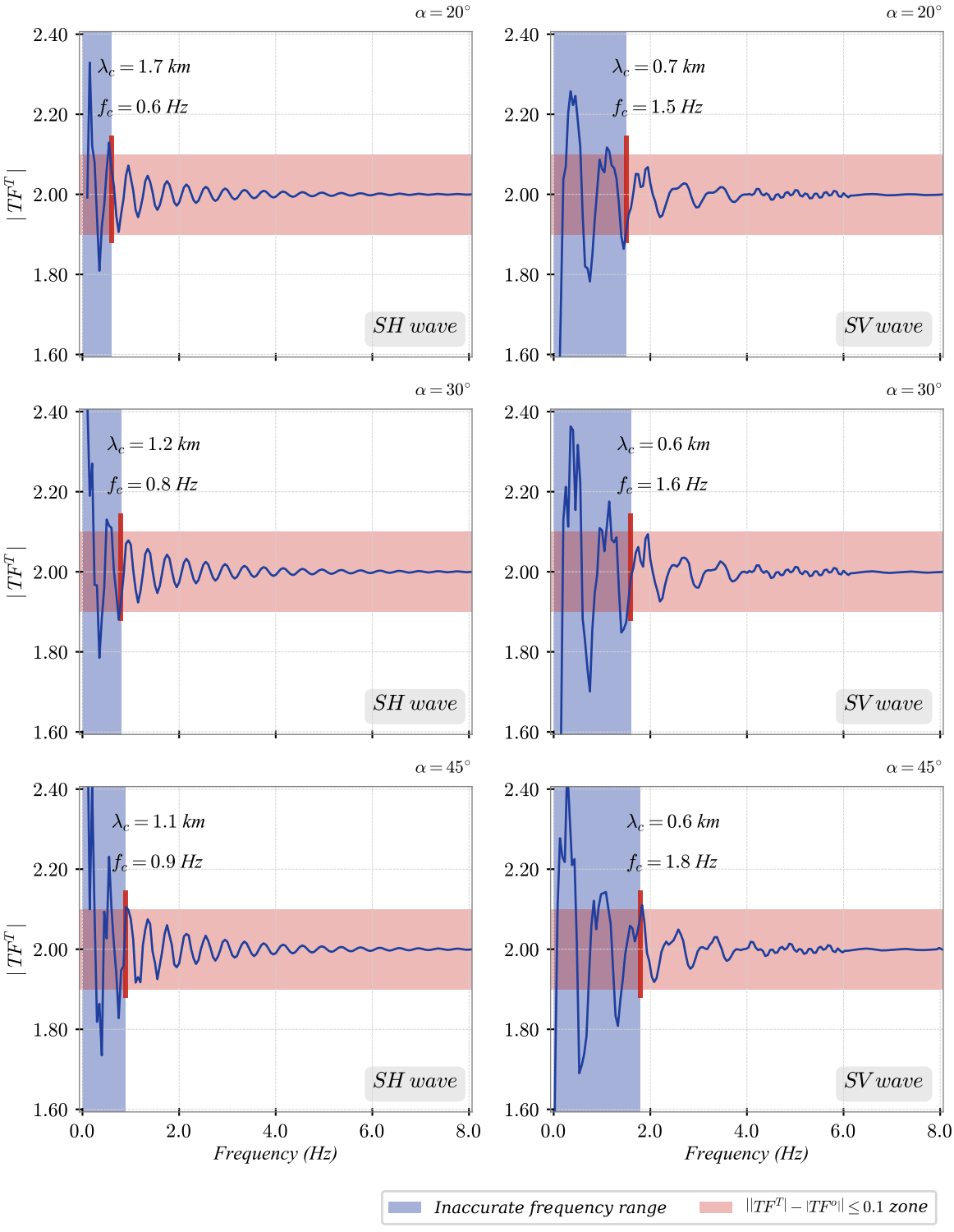

Figure 4.4. Amplitude of the transfer function for the total field U^T as per eq. (4.1) at the site of interest R for slopes of various angles and for vertically incident SH and SV waves. The vertical shaded band in the total response marks the frequency range above which the diffracted wavefield has minor effect in the total response. Similarly the horizontal shaded band limits the zone of negligible value of the transfer function.

From the parametric analysis we identify those frequencies at which the condition $\left|\left|TF^T\right| - |TF^o|\right| \leq 0.1$ is reached. These cut-off frequencies are reported in table 4.1 for each one of the considered angles and wave polarization. The cut-off frequency in each case marks the frequency range of the diffracted field that significantly contributes to the response at the point of interest R located at a distance $L_w = 2.5$ km from the source.

Table 4.1. Cut-off frequencies and their equivalent dimensionless parameter n as defined by eq. (4.2). n_{SH} and n_{SV} correspond to SH and SV wave incidence respectively.

α (°)	f_c^{SH} (Hz)	f_c^{SV} (Hz)	n_{SH}	n_{SV}
20	0.6	1.5	1.50	3.75
30	0.8	1.7	2.00	4.25
45	0.9	1.8	2.25	4.50

After recognizing the distance-frequency response of the diffracted waves it is convenient to condense the results from the parametric analysis in a single parameter n, represented in fig. 4.5 as a function of the slope angle and relating the wavelength λ_c associated to the cut-off frequency f_c and the distance L_w according to:

$$n = \frac{L_W}{\lambda_c}. \tag{4.2}$$

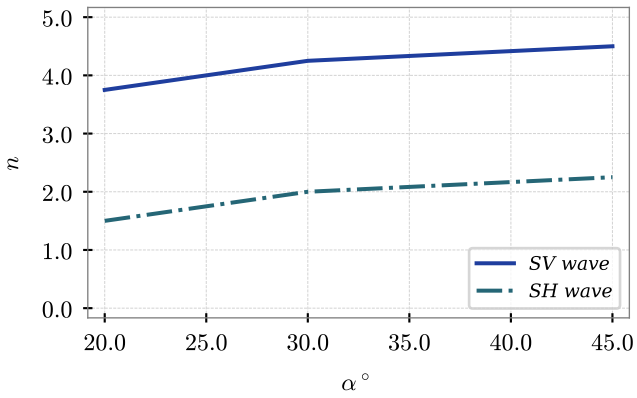

Figure 4.5. Variation of the dimensionless parameter n value with slope angle α.

The dimensionless parameter n is indicative of the number of wavelengths λ_c that can be accommodated in the source-receiver distance L_w. Accordingly, the values of n and f_c reported in table 4.1 can be used to estimate the effective distance L_{min} required in the construction of a particular model. To clarify the meaning of this dimensionless parameter consider a canyon of slope angle $\alpha = 20°$ under incident SH waves. The

values of $n_{SH} = 1.5$ and the associated cut-off frequency $f_c = 0.6$ Hz (highlighted in blue in table 4.1) implies that diffraction sources located beyond a distance $1.5\lambda_c$ do not contribute to the response at the receiver R and thus can be neglected.

4.2 Rational modelling of topographic effects in site response analysis.

According to the parametric analysis of a source of diffracted waves, only those waves of length $\lambda_c > \ell/n$, where ℓ is the receiver distance and n is the dimensionless parameter from table 4.1, contribute significantly to the response. Equivalently, sources located beyond ℓ do not contribute to the response for frequencies $f > f_c$. These results are used as the basis of our proposed method to find the minimum required size of a geometric profile to capture topographic effects. We postulate that if we are interested in finding the spectral response at a site up to a target structural period T^{tar}, only those topographic features located within a distance $\ell < L_{min}$ (measured on each side from the site of interest), where:

$$L_{min} = NT^{tar} \tag{4.3}$$

need to be included in the model. In eq. (4.3) N is also a parameter that depends on the type of motion analogous to n in eq. (4.2). Subsequently, if analysis is conducted with a reduced topographic model which extends through a distance L_{min} at each side from the point of interest the resulting response spectra would be accurate up to a period T^{tar}. The associated terms reduced-model and size-conditioned-response-spectra are now obvious.

The distance-response dependence is now taken as the fundamental relation between the effective size of the topographic profile and the size-conditioned-response-spectra. To find N we start again from eq. (4.2) and write

$$L_{min} = n\lambda^{tar}$$

and where now $\lambda^{tar} = \beta T^{tar}$. Using the dimensionless factor n (eq. (4.2)) it follows that:

$$L_{min} = (n\beta)T^{tar} \tag{4.4}$$

from which we recognize:

$$N = n\beta.$$

To clarify the meaning of L_{min} in eq. (4.3) and its usefulness in the determination of a size-conditioned-response-spectra, consider the topographic scenario shown in fig. 4.6

and for which an analyst wants to find the response at the receiver point R (highlighted by the blue triangle) and in terms of a response spectra which is accurate up to the target period T^{tar}. To select the minimum required model for the analysis, the size parameter L_{min} is computed using eq. (4.3) resulting in the model shown in the figure. The size-conditioned-response-spectra is accurate over the shaded part defined for $T < T^{tar}$.

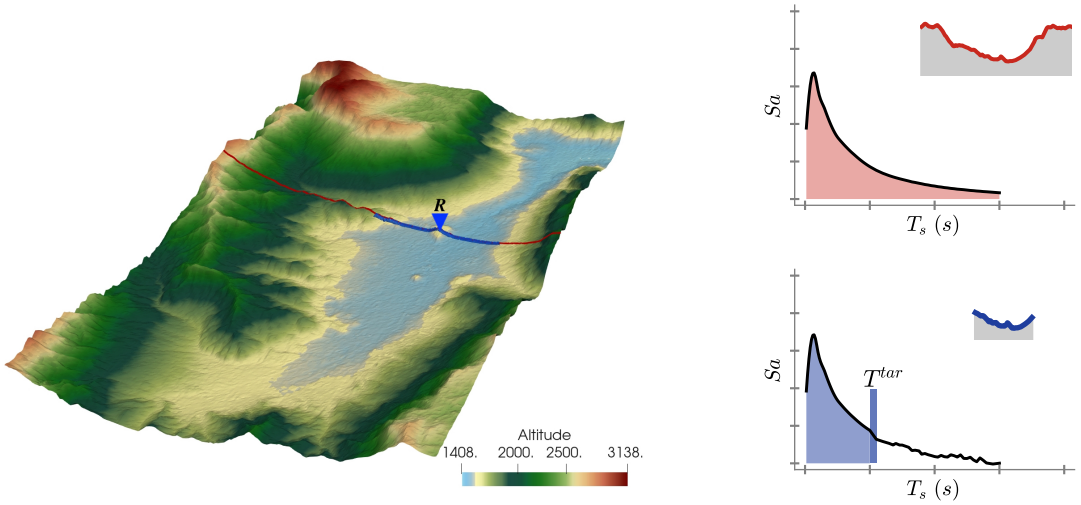

Figure 4.6. Schematic representation of the seismic scenario conformed by the large, regional model (with cross section shown at the top-right) and the reduced model (with cross section shown at the bottom-right). Analysis of the regional model produces a complete response spectra (fully shaded) whereas analysis of the reduced model of total width $2L_{min}$ produces a response spectra valid only up to the target period T^{tar} (partially shaded).

The following algorithm can be used to obtain the minimum required size as a function of the shear wave propagation velocity for the medium β and the target period T^{tar}. This period would fix the accurate size of the period window in the resulting response spectra. Using these parameters and the value of $n_{SH} = 2.25$ or $n_{SV} = 4.5$ compute L_{min} from eq. (4.4). At the site of interest build a computational domain which extends laterally a distance L_{min} at each side.

Data: β, T^{tar}
Result: L_{min}
LET $n_{SH} = 2.25$ or $n_{SV} = 4.50$ from Table 1;
USE (4.4) to compute L_{min};
BUILD the computational model extending L_{min} at each side from the site of interest;
CONDUCT site response analysis under vertically incident plane waves using numerical simulation;
Algorithm 1: Algorithm to build reduced models for the determination of Size Conditioned Response Spectra

4.2.1 Topographic effects with size-conditioned-response-spectra in the Aburrá Valley region in Medellin, Colombia

As study case to test the effectiveness in the prediction of surface shaking of the reduced models built through the concept of size-conditioned-response-spectra, we estimate the response along a set of 3 receivers distributed over a modified cross section of the Aburrá Valley Region (AVR) in Medellin, Colombia, fig. 4.7. This geographic scenario corresponds to a long-shaped sedimentary basin, which extends along the north-south direction for an approximate length of 40 km and with a nearly constant cross section of an average width of 25 km. The lowest part of the valley is formed by thin deposits of the Medellín river configuring a skin-like layer of sediments supported by a moderately stiff soil which is typically classified as type C by Colombian seismic standards. The flat part of the formation is surrounded by moderate-to-steep topographic irregularities where most of the current urban development, in terms of mid rise reinforced concrete buildings, is taking place. A detailed description of the urban and geographic context can be found in Restrepo et al. (2016).

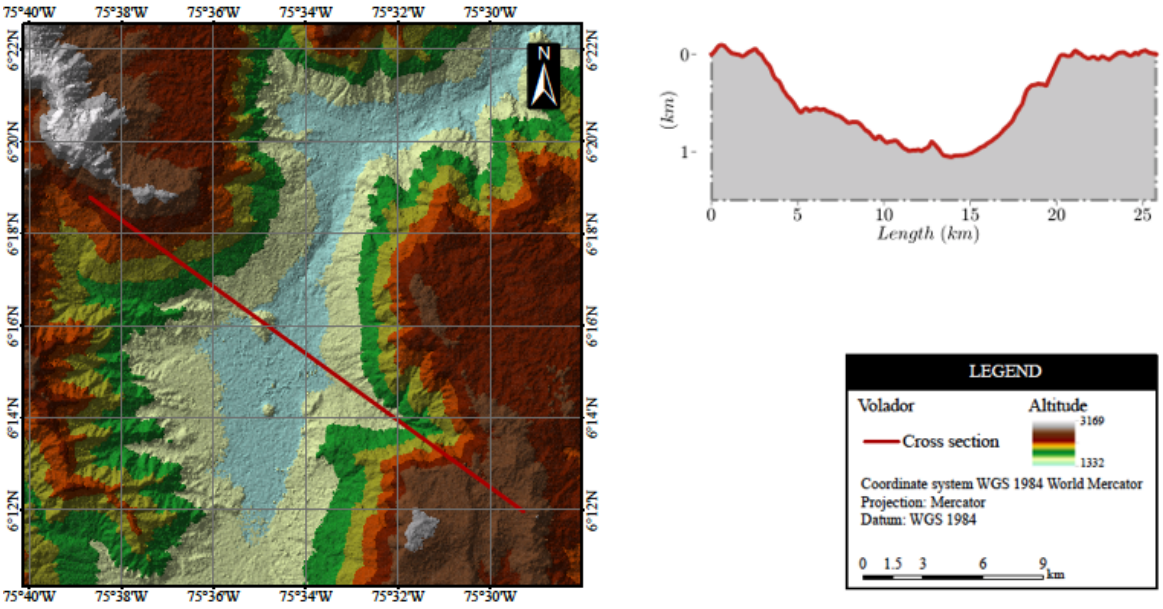

Figure 4.7. Top view of the Aburrá Valley Region studied in this work. The red line and corresponding cross section analyzed in this work are shown in the right. This section is referred herein as the volador cross section.

The geographic set up selected for the site response analysis, shown in fig. 4.8, is the same east-west cross section previously studied by Sáenz et al. (2019). In contrast to that study, here the altimetric configuration has been altered in 2.5 times in order to scale potential topographic effects. Although this scaling of the topographic features in the considered profile renders the model an unrealistic scenario such distortion aims at pushing the proposed methods to its limits so it can be used with confidence in realistic topographies. In this work we will find the response at the 3 sites of interest marked by the black triangles in fig. 4.8. These are located at typical sites found within the actual urbanistic context of the city. To find the response at the different sites we used the same in-house implementation of the boundary element method from the previously described parametric analysis. At each site we found the response from (i) a reduced model, built using the effective length from eq. (4.4), and (ii) from the full regional topography. In each case the selected target period was $T^{tar} = 1.0$ s, shear wave propagation velocity $\beta = 1.0$ km/s, $n_{SH} = 2.25$ and $n_{SV} = 4.50$, which corresponds to the most conservative case reported in table 4.1 and associated to the 45°-canyon. Each resulting reduced-model, for SV and SH waves is shown on the right side of fig. 4.8 while its relative location and size is shown by the shaded area in the regional profile. It must be realized that in our case the shaded area in these figures is shown just for reference but it does not form a discretized computational domain since we are using a boundary element based algorithm which discretices only the surface topography. If the analysis of the reduced model is to be conducted with domain-based methods like the finite element method care should be taken with suppressing the effect from spurious reflections in the boundaries where the model is truncated. These effects however are not the subject of this work.

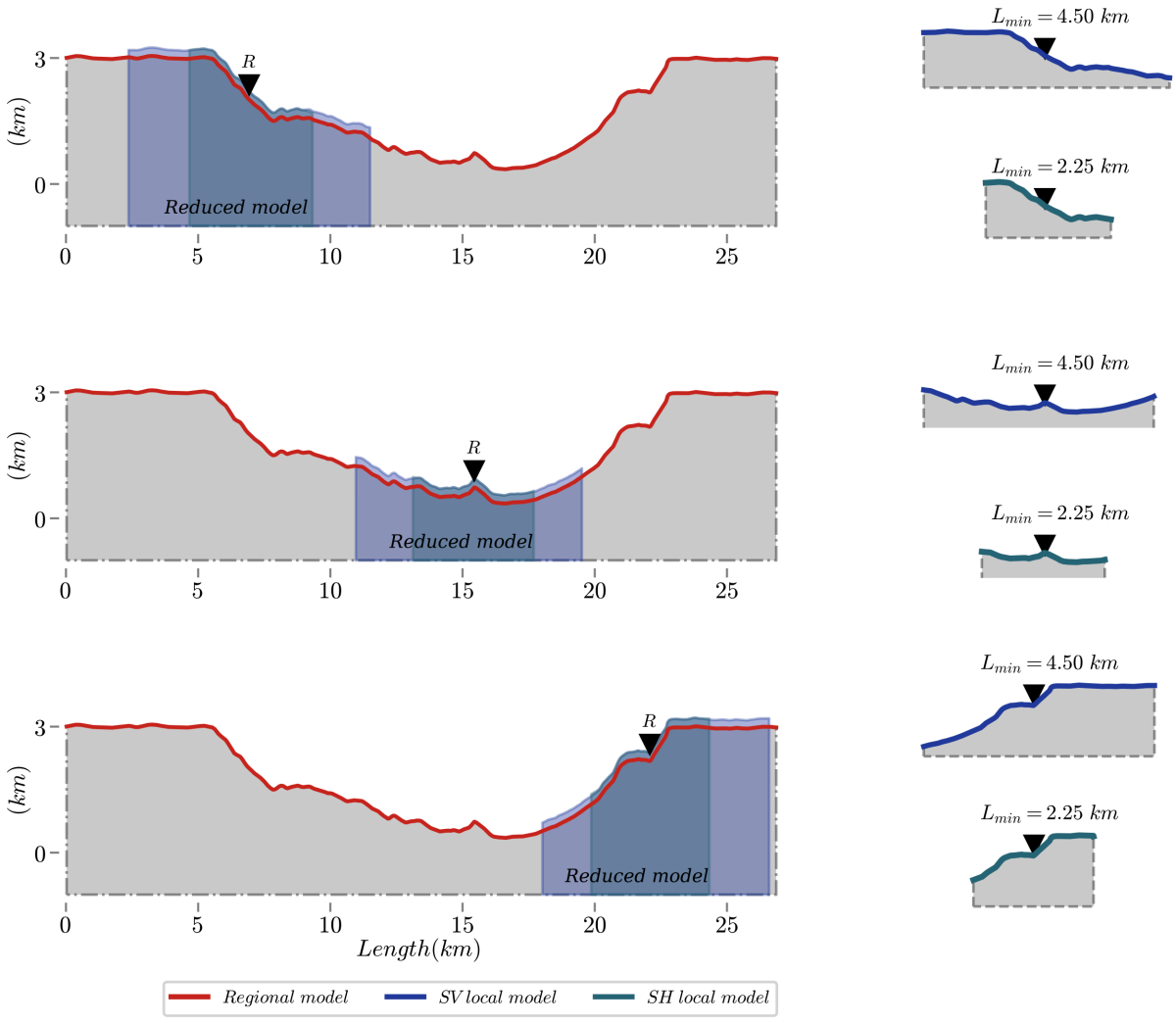

Figure 4.8. Two-dimensional east-west cross sections from the Aburrá Valley region used in this study. The left panel shows the complete or regional cross-section while the right panels show the reduced models. The point of interest is the black triangle in all cases. The size and relative location of the reduced models within the large profile are shown by the shaded portion of the full model.

The analyses were conducted in the frequency domain where the resulting transfer functions from excitations in the form of plane SV and SH waves were later convoluted with the Fourier spectra of the input signal shown in fig. 4.9. The input signal corresponds to a synthetic outcropping-like motion obtained after numerical manipulation of a record from the Michoacán, México 1997 earthquake after using the algorithm from Al Atik & Abrahamson (2010). The numerical manipulation is mainly intended to achieve a Fourier spectra with constant amplitudes in the range $[0.1 - 10.0]$ Hz in order to obtain appreciable spectral modifications over a wide period range.

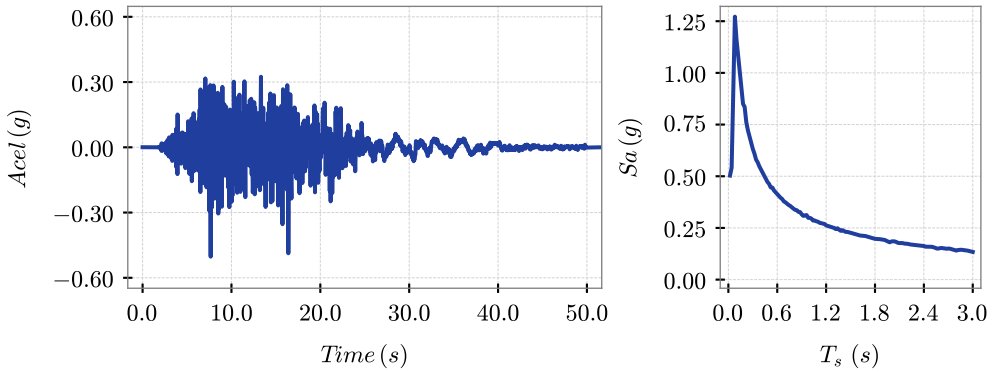

Figure 4.9. Synthetic acceleration time history used in this work and its corresponding response spectra. The original signal corresponds to a record from the Michoacán, México 1997 earthquake. For analysis purposes the signal has been numerically modified to match a Fourier spectra with constant amplitudes in the range $[0.1 - 10.0]$ Hz.

Results are presented in the form of ratios of response spectra (RRS) between ground motions obtained with the reduced-model and those of the full or regional topographic profile, which are assumed like the exact solution for comparison purposes. Results corresponding to SH and SV wave incidence are shown in fig. 4.10, the right panel in each case shows the receiver location within the regional scenario. The gray band surrounding each solution corresponds to the accurate response zone of range $[0.95 - 1.05]$, while the horizontal (dashed) line highlights the exact ratio of 1.0. As a final aid in the interpretation of results the small vertical line in each plot specifies the target period $T^{tar} = 1.0$ s. Note that the response in all cases is contained within the gray band even for periods larger than the prescribed target value. This is due to the fact that we have used a conservative value of n in eq. (4.4).

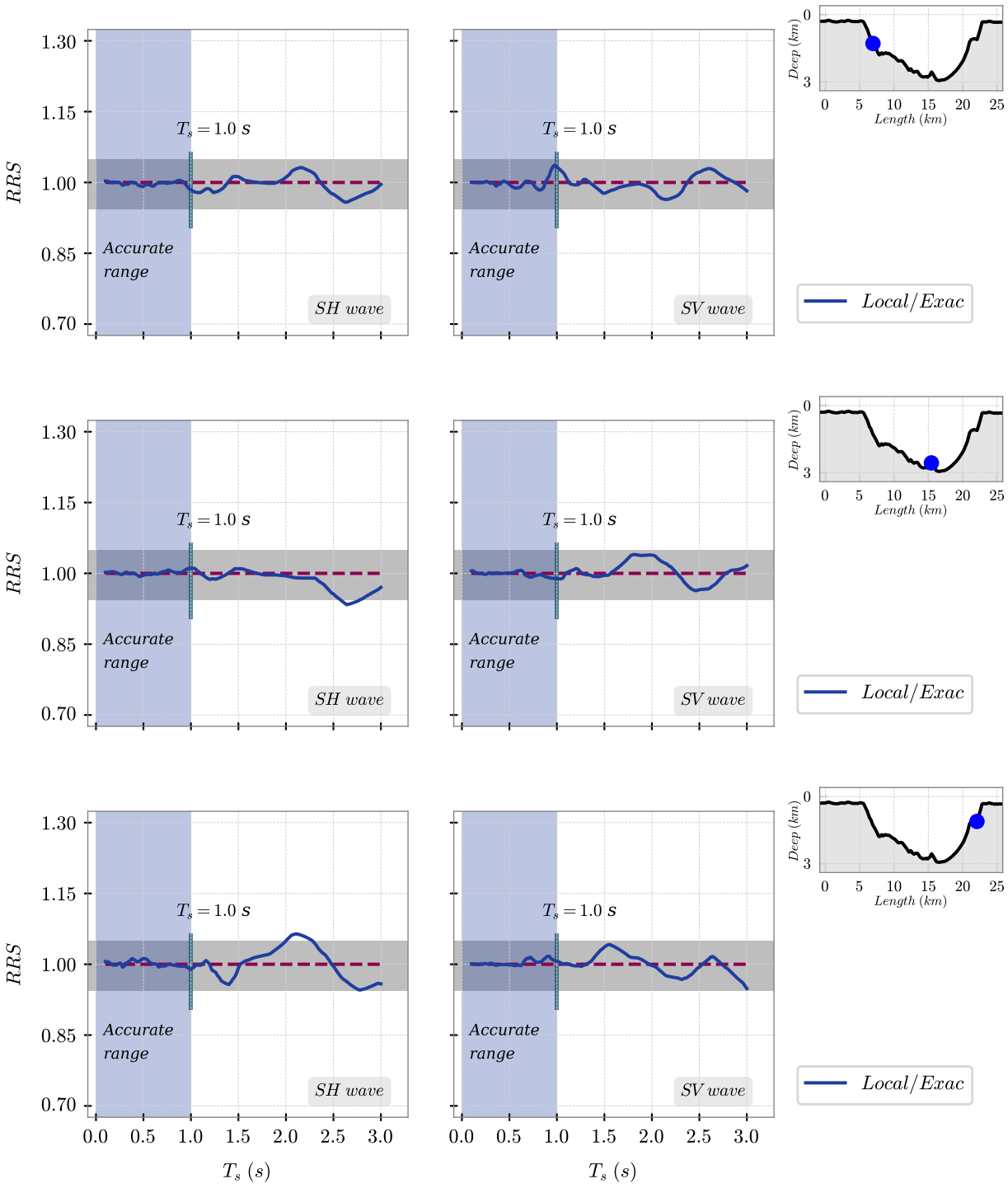

Figure 4.10. Ratios of response spectra at different points of interest between responses obtained with the reduced model and the full model. The light gray band in each case limits the region of accepted accuracy in the response while the vertical line shows the target period. The relative location of the point of interest in each profile is shown by the inset figure.

The effectiveness behind the proposed reduced models was also tested for a second cross section corresponding to a convex regional topography. In this case, the profile, shown in fig. 4.11 was artificially generated after performing a 180° rotation of the original concave profile with respect to an horizontal axis. The regional and reduced topographies are presented in fig. 4.11, while the resulting spectral ratios are shown in fig. 4.12. Accuracy is still maintained up to the target period, however by contrast to the case of the concave scenario the effective period range is now shorter.

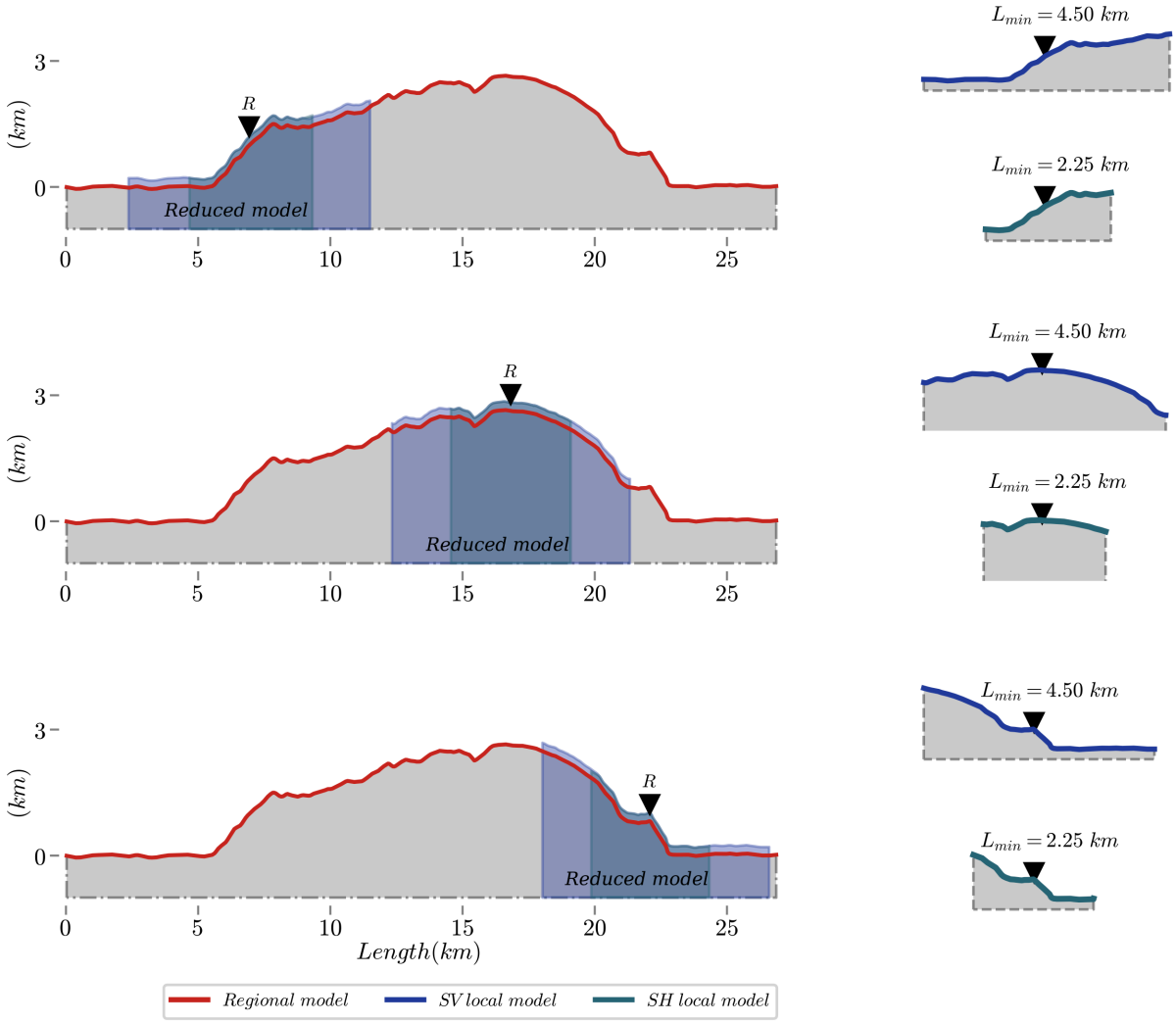

Figure 4.11. Fictitious two-dimensional cross-section resulting from a 180° rotation with respect to an horizontal axis from the original section shown in fig. 4.8. The reduced models for incident SV and SH waves are shown in the middle and right panels.

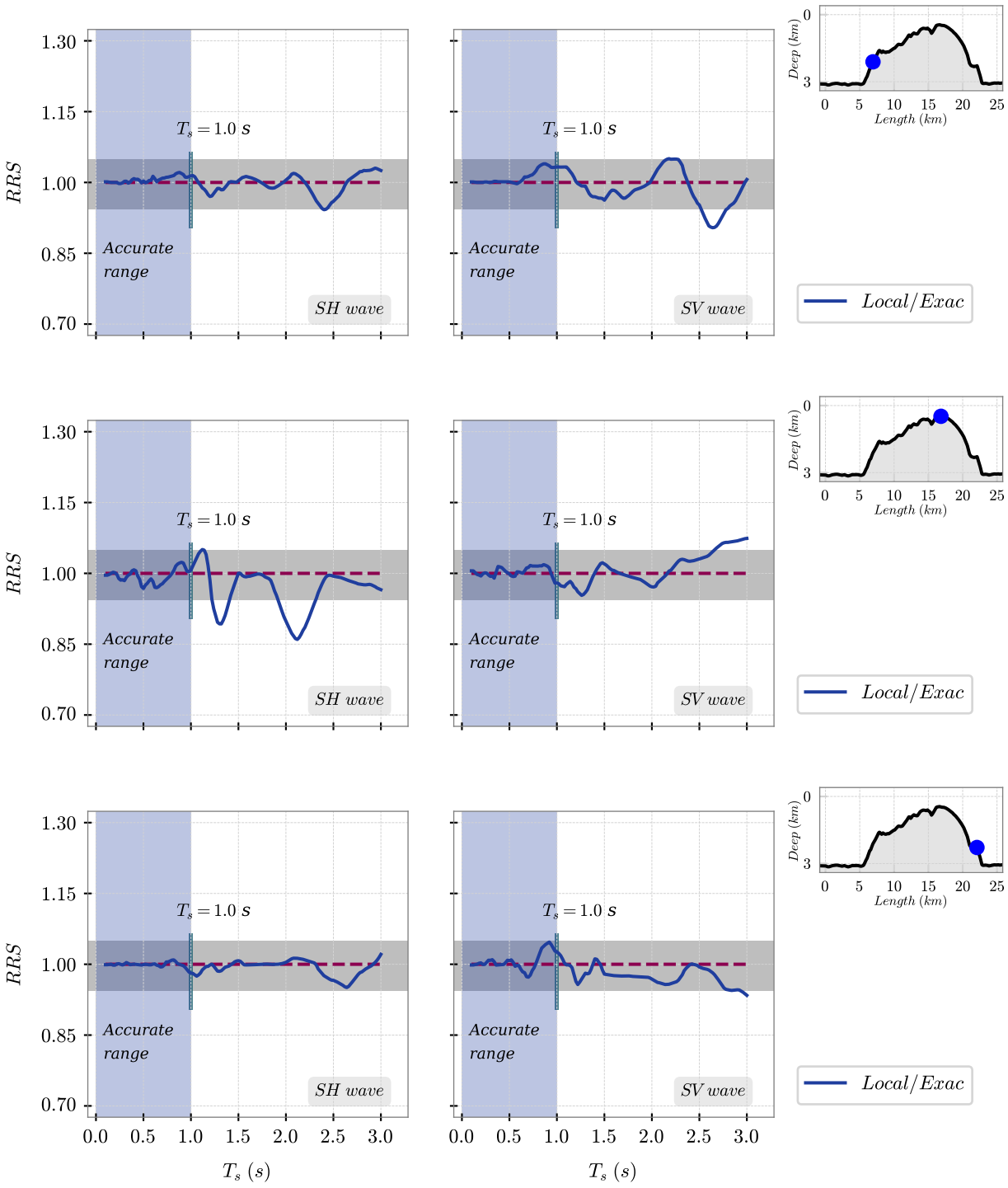

Figure 4.12. Ratios of response spectra at different points of interest between responses obtained with the reduced model and the full model. The light gray band in each case limits the region of accepted accuracy in the response while the vertical line shows the target period. The relative location of the point of interest in each profile is shown by the inset figure.

4.2.2 Effect of smoothing the shape in the topographic profile

Topographic aggravation factors available in code regulations are based on smooth geometric models. Here we explore the effect of those simplified shapes. For that purpose we conducted further analysis at the 3 receivers from fig. 4.10 and whose reduced models based on a target period $T = 1.0$ s were already found and reported in fig. 4.8. The topography in these models is now further simplified using the method from Sáenz et al. (2019). We select a prescribed low limit period of $T = 0.6$ s which implies that all irregularities of characteristic dimension smaller than $h = 24$ m can be eliminated without affecting the response at periods larger than $T = 0.6$ s. The simplified models and results in terms of ratios of response spectra are shown in fig. 4.13. The reported spectral ratios are the quotients between the spectral response obtained with the reduced and form-simplified model and the full topographic profile. The RRSs are guaranteed to be accurate in the period range between $T = 0.6$ s and $T = 1.0$ s and where low and high frequency effects were removed through two independent operations corresponding to size-reduction and form-simplification.

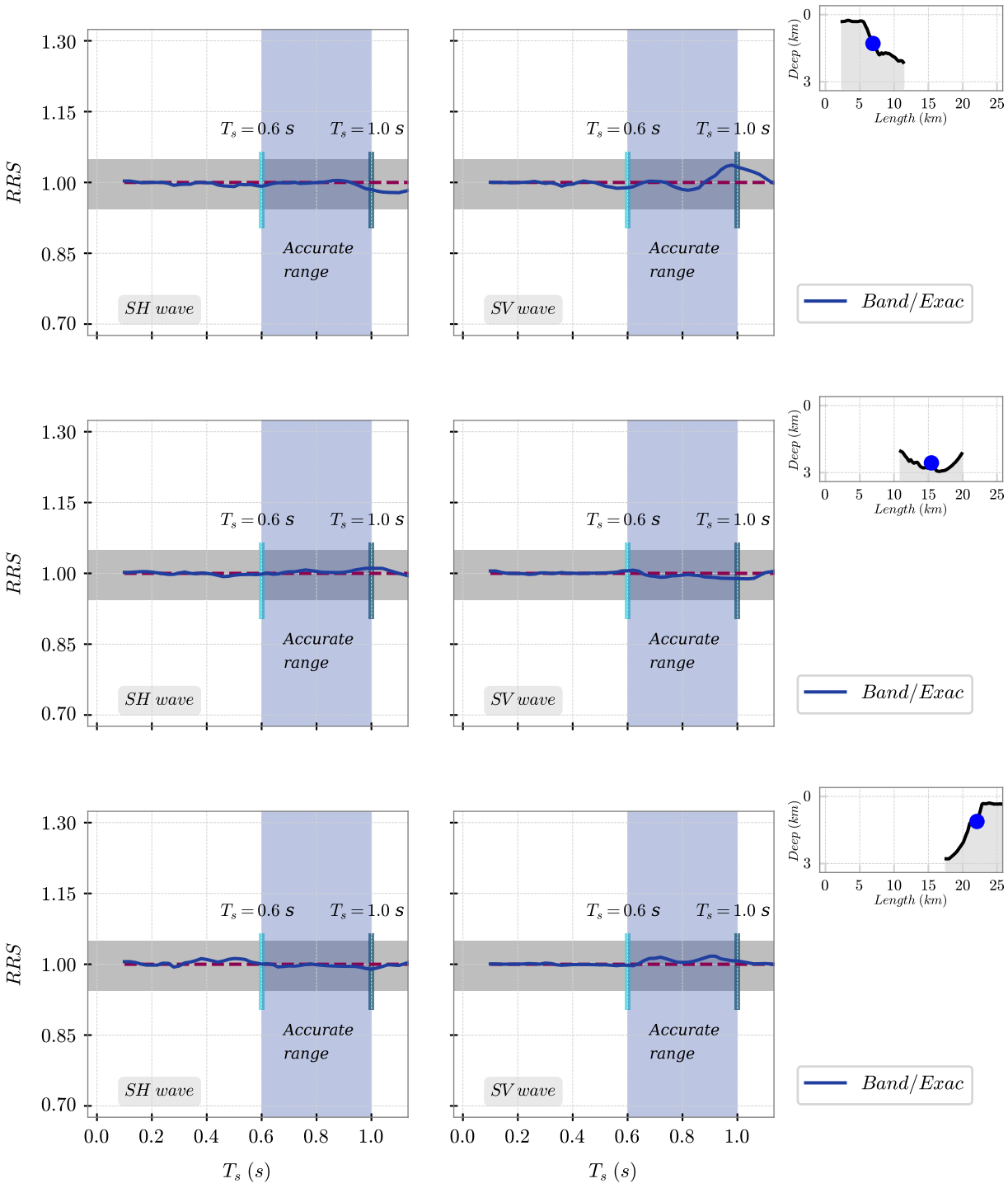

Figure 4.13. Ratios of response spectra at different points of interest between responses obtained with the reduced model after applying also the smoothing approach formulated in Sáenz et al. (2019) and the full model. The valid portion of the response spectra is now highlighted between vertical bars.

Conclusions

We addressed the problem of topographic effects from an engineering perspective. Particularly, we propose an expression to find the minimum required size of an analysis model that guarantees results with spectral accuracy up to a prescribed value of a target period T^{tar}. We introduce two main concepts namely: (i) reduced models (or reduced topographic profiles) to refer to the portion of the regional geographic setup that must be analyzed in order to capture topographic effects up to a target period T^{tar} and (ii) size-conditioned-response-spectra (SCR) to refer to the response spectra associated to a reduced topographic model and valid in the period range $T = [0.1, T^{tar}]$.

The required size vs target period relation to select the appropriate reduced model at a particular site is obtained from a frequency domain based parametric analysis of the amplitude of the transfer function for the total field. For these waves, which are known to decay with distance, we found that the number of wavelengths required for a diffracted wave of frequency f propagating at the speed β, to decay below a certain threshold value is constant. The size of the reduced model changes in such a way that the larger the value of the target period, the larger the required reduced model dimension.

The proposed approach is then applied to the prediction of the response at 3 local sites within an artificial model built out of a cross-section of the Aburrá Valley Region in Medellín, Colombia. At each site we found the response using a reduced model, associated to a target period, and the full regional topography. Results are presented in terms of ratios of response spectra between the two models from which we conclude that in fact the reduced models are accurate even for periods larger than the target period. For the prescribed target periods we found reduced models with an effective size close to 32% of the regional model.

As an additional test, we shape-simplified the reduced models in order to resemble the idealized topographies behind coded-based aggravation factors. We found that this secondary smoothing effect introduces error in the low period range thereby limiting the accurate spectral response to a finite period band defined between $T = T^{min}$ and a maximum value $T = T^{tar}$.

Chapter 5

WAVES: Explicit parallelized finite element solver for wave Propagation Analysis

Introduction

Numerical modeling is needed in the quantification of topographic effect in the response at a local site. In this dissertation we have used a frequency domain based boundary element technique as a computational tool to elucidate the physics behind the impact of surface topography in the local response. As described in previous chapters this technique has the advantage of accurately incorporating radiation boundary conditions at infinity through properly formulated frequency dependent Green's functions. However, this inherent frequency-domain nature makes such methods highly specialized to be used in a routine basis by consulting engineers which are more familiar with time domain analysis conducted with commercial finite element packages. When conducting wave propagation analysis in terms of commercial codes the main issue is in the imposition of a physically sound excitation representative of the incident seismic field.

In this appendix we describe an explicit finite element solver which has been developed as part of this dissertation. In particular, algorithms based upon the finite element method (FEM) have the advantage of allowing the incorporation of arbitrary boundary conditions and material models. This section describes the explicit finite element code **WAVES** which has been created as part of the research program on topographic effects conducted at the research lab Grupo de Mecanica Aplicada at Universidad EAFIT. Although the code has been originally implemented for the solution of plane wave scattering problems in the time domain, it is also possible to conduct analysis of generalized dynamic problems in 2D and 3D domains.

In simple terms the computer program finds the displacement time history for arbitrary two-dimensional and three-dimensional domains discretized into finite elements. As its main features the code allows to conduct plane wave analysis using as input excitation

the domain reduction (DRM) technique formulated by Bielak et al. (2003), while the time discretization corresponds to a central difference scheme (having diagonal mass matrices) with uncoupled equations for each degree of freedom. Here we first present the time-domain discretization scheme resulting in an explicit solution algorithm. Further details of the code, including a user manual and several examples are available in the github repository Waves. As a main feature the code allows for the implementation of user defined elements and material models with an explicit formulation. In the final part of this section we conduct a numerical experiment showing two alternative forms of imposing dynamic excitations required for topographic effects. The experiment is conducted in the analysis of the response of V-shaped canyon, a trapezoidal hill and semi-circular valley. In each one of these topographies the response is computed with our finite element solver but applying the incident plane field in terms of an exact domain reduction method and an approximate transmitting boundary approach.

5.1 Explicit solution scheme

Consider the discrete dynamic equilibrium equations at time t

$$M\,{}^{t}A + C\,{}^{t}V + K\,{}^{t}U = {}^{t}F \tag{5.1}$$

and where M, C, K are the assembled mass, damping and stiffness matrices respectively while ${}^{t}A$, ${}^{t}V$, ${}^{t}U$ and ${}^{t}F$ are the nodal accelerations, velocities, displacements and external loads vectors at time t. In **WAVES** the external forces may be the result of particular point loads or effective forces consistent with a plan wave analysis.

In terms of nodal forces, eq. (5.1) can be written like;

$${}^{t}F^{I} + {}^{t}F^{D} + {}^{t}F^{s} = {}^{t}F \tag{5.2}$$

where ${}^{t}F^{I}$, ${}^{t}F^{D}$ and ${}^{t}F^{s}$ are inertial, damping, elastic and external nodal forces respectively.

Expanding the acceleration and velocity terms at time t in a consistent finite central differences scheme we have;

$$\begin{aligned} {}^{t}A &= \frac{1}{\Delta t^2}\left({}^{t-\Delta t}U - 2\,{}^{t}U + {}^{t+\Delta t}U\right) \\ {}^{t}V &= \frac{1}{2\Delta t}\left(-{}^{t-\Delta t}U + {}^{t+\Delta t}U\right). \end{aligned} \tag{5.3}$$

Consider now the trial states

$$
\begin{aligned}
{}^{t}\hat{A} &= \frac{1}{\Delta t^2}\left({}^{t-\Delta t}U - 2^{t}U\right) \\
{}^{t}\hat{V} &= -\frac{1}{2\Delta t}{}^{t-\Delta t}U
\end{aligned}
\tag{5.4}
$$

which allows us to write eq. (5.3) like;

$$
\begin{aligned}
{}^{t}A &= {}^{t}\hat{A} + \frac{1}{\Delta t^2}{}^{t+\Delta t}U \\
{}^{t}V &= {}^{t}\hat{V} + \frac{1}{2\Delta t}{}^{t+\Delta t}U
\end{aligned}
\tag{5.5}
$$

Notice that the terms ${}^{t}\hat{A}$ and ${}^{t}\hat{V}$ result after assuming that ${}^{t+\Delta t}U = 0$ in eq. (5.3) thus they are commonly referred to as predictors. Notice also that after the displacements at $t+\Delta t$ have been found the corrected values of ${}^{t}A$ and ${}^{t}V$ can be obtained via eq. (5.5). In this sense the terms $\frac{1}{\Delta t^2}{}^{t+\Delta t}U$ and $\frac{1}{2\Delta t}{}^{t+\Delta t}U$ play the role of correctors to the initial predictors. The resulting algorithm is commonly referred to, by obvious reasons, as a predictor-corrector scheme.

Using eq. (5.5) in eq. (5.1) results in the following equation governing the displacements at time $t+\Delta t$;

$$
\left(\frac{1}{\Delta t^2}M + \frac{1}{2\Delta t}C\right)^{t+\Delta t} U =^{t} F - M^{t}\hat{A} - C^{t}\hat{V} - K^{t}U \tag{5.6}
$$

The dynamic finite element equilibrium equations given in eq. (5.6) can be written in the standard static form:

$$
\hat{K}^{t+\Delta t}U = {}^{t}\hat{F}
$$

after letting;

$$
\hat{K} = \frac{1}{\Delta t^2}M + \frac{1}{2\Delta t}C
$$

and

$$
{}^{t}\hat{F} = {}^{t}F - M^{t}\hat{A} - C^{t}\hat{V} - K^{t}U
$$

.

It is convenient, and physically appealing, to write eq. (5.6) in terms of forces like:

$$
{}^{t+\Delta t}F^{I} +^{t+\Delta t} F^{D} =^{t} F -^{t} \hat{F}^{I} -^{t} \hat{F}^{D} -^{t} F^{s} \tag{5.7}
$$

- Equation (5.7) is an equilibrium equation at time $t = t$ allowing to predict the displacements at time $t = t + \Delta t$ in terms of previously known values at times t and $t = t - \Delta t$ as schematically shown in fig. 5.1

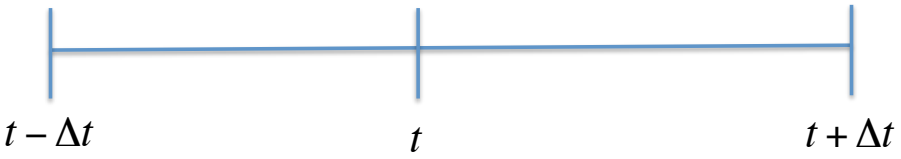

Figure 5.1. Definition of the general iteration giving displacements at $t = t + \Delta t$ in terms of previously known values at times t and $t = t - \Delta t$.

- The equation is exact within the error introduced by the expansion used in eq. (5.3).
- The first predicted solution is at $t = \Delta t$ which implies that we require data at $t = -\Delta t$ and at $t = 0$ (i.e., initial conditions) as schematically shown in fig. 5.2.

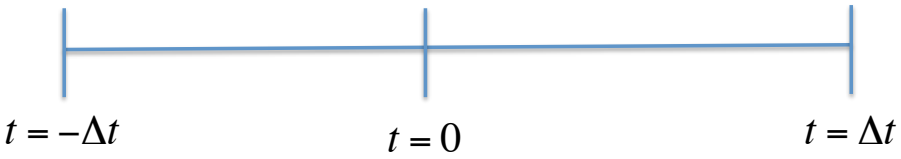

Figure 5.2. Initial iteration predicting values at time $t = \Delta t$ in terms of the artifitial values at $t = -\Delta t$ and the initial conditions at $t = 0$.

5.1.1 Damping Assumptions

The damping matrix C appearing in eq. (5.6) is actually not assembled in the standard finite element sense but it is rather built from the mass and stiffness matrices. Moreover we can consider the following possibilities regarding damping.

(i) Neglect damping (This is however inconvenient for finite domains) which gives:

$$^{t+\Delta t}F^I + ^{t+\Delta t}F^D = ^t F - ^t \hat{F}^I - ^t F^s \tag{5.8}$$

(ii) Use Rayleigh Damping and retain the velocity expansion used in (5.3). That is;

$$C = \alpha M + \beta K \tag{5.9}$$

then we have (in terms of forces);

$$(1 + \beta \Delta t^2)^{t+\Delta t}F^I + \frac{\alpha}{2\Delta t}{}^{t+\Delta t}F^S = ^t \hat{F} \tag{5.10}$$

where;

$$ {}^{t}\hat{F} = {}^{t}F - {}^{t}\hat{F}^{I} - {}^{t}\hat{F}^{D} - {}^{t}F^{s} $$

Solution in equation eq. (5.10) requires the full assembly and factorization of an effective stiffness matrix.

(iii) Use Rayleigh damping but modify the velocity expansion introduced in eq. (5.3). Using

$$ {}^{t}V = \frac{1}{\Delta t}({}^{t}U - {}^{t-\Delta t}U) \tag{5.11} $$

yielding;

$$ {}^{t+\Delta t}F^{I} = {}^{t}F - {}^{t}\hat{F}^{I} - {}^{t}\hat{F}^{D} - {}^{t}F^{s} \tag{5.12} $$

where now the velocity predictor and corrector terms are defined like:

$$ {}^{t}\hat{V} = \frac{1}{\Delta t}\left({}^{t}U - {}^{t-\Delta t}U\right) $$

and

$$ {}^{t}V = \frac{1}{2\Delta t}\left(-{}^{t-\Delta t}U + {}^{t+\Delta t}U\right) $$

respectively, giving the equation:

$$ {}^{t+\Delta t}F^{I} = {}^{t}F - {}^{t}\hat{F}^{I} - {}^{t}F^{s} - {}^{t}\hat{F}^{D} \tag{5.13} $$

5.1.2 Algorithm implemented in WAVES (damping assumption 3)

Let us write eq. (5.13) like

$$ {}^{j+1}F^{I} = {}^{j}F - {}^{t}\hat{F}^{I} - {}^{j}F^{s} - {}^{j}\hat{F}^{D}. \tag{5.14} $$

The first prediction corresponding to $t = \Delta t$ is given by;

$$ {}^{\Delta t}F^{I} = {}^{0}F - {}^{0}\hat{F}^{I} - {}^{0}\hat{F}^{S} - {}^{0}\hat{F}^{D} $$

which results after applying eq. (5.13) at $t = 0$ and where the term

$$ {}^{0}\hat{F}^{D} = C\frac{1}{\Delta t}\left({}^{0}U - {}^{-\Delta t}U\right) $$

requires knowing the fictitious value $-^{\Delta t}U$. This last term can be computed after applying the central difference expansion at $t = 0$ and solving for $-^{\Delta t}U$ giving;

$$-^{\Delta t}U =^{0} U - \Delta t\,{}^{0}V + \frac{\Delta t^2}{2}{}^{0}A \tag{5.15}$$

Finally using eq. (5.15) in eq. (5.14) allows us to start up the algorithm. The general and initial iteration are schematized in fig. 5.3 and fig. 5.4 respectively.

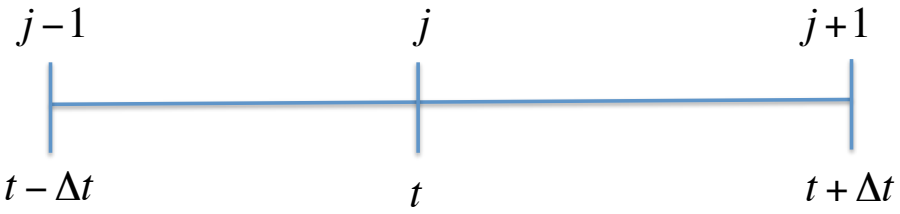

Figure 5.3. Definition of the general iteration

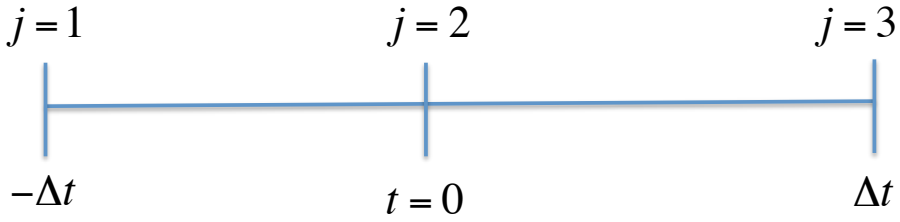

Figure 5.4. Definition of the initial iteration

5.1.3 Decoupling

The equilibrium equations discussed so far can be decoupled whenever the coefficient matrix is diagonal. As a result, the algorithm can proceed one degree of freedom at a time without the need for a complete assembly process and with large memory savings. Consider the particular case of damping assumption 3 and a lumped mass matrix. Writing eq. (5.14) for the i-th degree of freedom (i.e., i is kept fixed) results in:

$$\frac{1}{\Delta t^2} M_{ij}{}^{t+\Delta t}U_j =^{t} F_i - K_{ij}{}^{t}U_j - M_{ij}{}^{t}\hat{A}_j - C_{ij}{}^{t}\hat{V}_j \tag{5.16}$$

Now, if the lumped mass matrix is written like;

$$M_{ij} = m_I \delta_{ij}$$

we have:

$$\frac{1}{\Delta t^2} m_I {}^{t+\Delta t}U_i =^t F_i - K_{ij}\,{}^tU_j - m_I\,{}^t\hat{A}_i - C_{ij}\,{}^t\hat{V}_j \tag{5.17}$$

producing the following recursive equation;

$${}^{t+\Delta t}F_i^I =^t F_i -^t \hat{F}_i^S - {}^t\hat{F}_i^{\,I} - {}^t\hat{F}_i^{\,D}. \tag{5.18}$$

To initialize the algorithm we apply the FDs equations at $t = 0$ leading to:

$$\frac{1}{\Delta t^2} m_I {}^{\Delta t}U_i =^0 F_i - K_{ij}\,{}^0U_j - m_I\,{}^0\hat{A}_i - C_{ij}\,{}^0\hat{V}_i.$$

In the above we require:

$${}^0\hat{V} = \frac{1}{\Delta t}\left({}^0U_i - {}^{-\Delta t}U_i\right)$$

which at the same time implies prior knowledge of the artificial term ${}^{-\Delta t}U_i$. This can be obtained from (5.15) as follows:

$${}^{-\Delta t}U_i =^0 U_i - \Delta t\,{}^0V_i + \frac{\Delta t^2}{2}\,{}^0A_i. \tag{5.19}$$

The initial acceleration is obtained after assuming homogeneous ICs;

$$m_I\,{}^0A_i + C_{ij}\,{}^0V_j + K_{ij}\,{}^0U_j =^0 F_i$$

therefore

$$m_I^0 A_i = \frac{{}^0F_i}{m_I}$$

and

$${}^{-\Delta t}U_i = \frac{\Delta t^2}{2m_I}\,{}^0F_i.$$

Moreover, neglecting the damping effects on the prediction of ${}^{\Delta t}U_i$ yields;

$${}^{\Delta t}U_i = \frac{\Delta t^2}{2m_I}\,{}^0F_i$$

Data: Time span, Geometry, Material Parameters
Result: Displacements, Velocity and Acceleration time histories
Initialize solution vectors ($j = 1$ corresponds to ICs: 0 superscript indicates $t = 0$);
${}^{0}U_i \longleftrightarrow^{j=1} U_i = 0$, ${}^{0}V_i = 0$, ${}^{j=1}A_i = \dfrac{{}^{1}R_i}{m_I}$;
Select Δt and damping coefficients α, β;
Fix 1-st predicted value (let $j = 2$);

$$ {}^{\Delta t}U_i \longleftarrow \frac{\Delta t^2}{2m_I}{}^{0}F_i \longleftrightarrow \left[{}^{j=2}U_i \longleftarrow \frac{\Delta t^2}{2m_I}{}^{j=1}F_i\right] $$

Time Integration Phase;
while $j \leq N$ **do**

Predictors

$$ {}^{j}\hat{A}_i \longleftarrow \frac{1}{\Delta t^2}\left({}^{j-1}U_i - 2{}^{j}U_i\right) $$

$$ {}^{j}\hat{V}_i \longleftarrow \frac{1}{\Delta t}\left({}^{j}U_i - {}^{j-1}U_i\right) $$

$$ {}^{j+1}F_i^I \longleftarrow {}^{j}F_i - K_{ij}{}^{j}U_j - m_I{}^{j}\hat{A}_j - C_{ij}{}^{j-1}\hat{V}_j $$

Solve

$$ {}^{j+1}U_i \longleftarrow \frac{\Delta t^2}{m_I}{}^{j+1}F_i{}^{I} $$

Correctors

$$ {}^{j}A_i \longleftarrow {}^{j}\hat{A}_i + \frac{1}{\Delta t^2}{}^{j+1}U_i $$

$$ {}^{j}V_i \longleftarrow {}^{j}\hat{V}_i + \frac{1}{2\Delta t}{}^{j+1}U_i $$

$$ j \longleftarrow j + 1 $$

end

Algorithm 2: Full Algorithm

5.1.4 Program structure

In the explicit integration scheme the solution corresponding to the i-th degree of freedom at time $t + \Delta t$ is found from eq. (5.20):

$$ {}^{j+1}U_i \longleftarrow \left(\frac{\Delta t^2}{m_I}\right){}^{j+1}F^I{}_i \tag{5.20} $$

where m_I is the total mass associated to the i-th degree of freedom and ${}^{j+1}F_i^I$ is the total force considering the contribution from the external, elastic, inertial and damping terms at times t and $t - \Delta t$. This force is given by eq. (5.21):

$$ {}^{j+1}F_i^I \longleftarrow {}^{j}\ F_i - K_{ij}{}^{j}U_j - m_I{}^{j}\hat{A}_i - C_{ij}{}^{j}\hat{V}_j. \tag{5.21} $$

Accordingly, in the uncoupled explicit finite element formulation the equation solving process proceeds one degree of freedom at a time. This implies a different assembly process to the one used in an implicit algorithm where a formal coefficient matrix is assembled and inverted. Now the mass, damping and stiffness elemental matrices are used to obtain effective nodal forces at each degree of freedom. In summary the mesh is not covered in an element by element basis, but in a node by node basis. In the following algorithm we discuss this nodal assembly process where in order to solve the displacement at a given degree of freedom prior knowledge of the elements contributing to the given node is necessary.

In particular in **WAVES** the total mass m_I and the total force ${}^{j+1}F_i^I$ is built after considering the contribution from the different elements connected to the node. This nodal assembly process is schematized in fig. 5.5 in which 4 bi-lineal elements are connected by a central node.

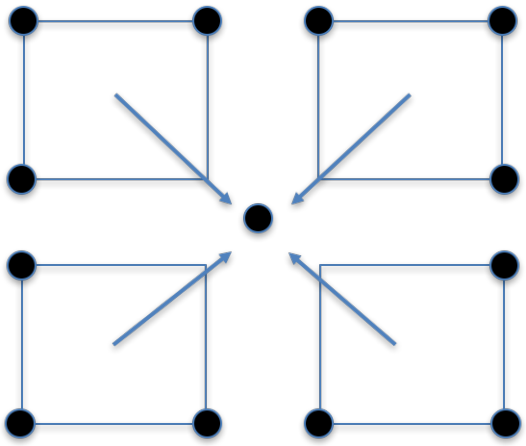

Figure 5.5. Nodal assembly

The nodal assembly is described in the following algorithm:

Data: Number of elements connected to the node
Result: Total mass and force contribution
for $i \longleftarrow 1$ *to* $Numnp$ **do**
  $k \longleftarrow NIEL_i$
  for $j \longleftarrow 1$ *to* k **do**
    Retrieve element parameters
    Compute predictors
    Compute element contribution (**UEL.for**)
    Assembly element contribution into the force vector ${}^{j+1}F_i^I$
  end
  Solve for the current d.o.f
  Perform corrections.
end

Algorithm 3: Nodal assembly

The subroutine **UEL.for** in the algorithm computes the contribution from the current element to the degree of freedom being solved. The library of available elements in the code corresponds precisely to a set of **UELs** subroutines. Additional elements can be easily implemented and added to the code by just coding new **UEL** subroutines as will be specified later.

5.2 Dynamic response of canonical shapes

As an application of our explicit time domain finite element solver we compute the dynamic response of the three simple canonical shapes shown in fig. 5.6. Specifically, the aim of this section is to test the imposition of incident plane waves through approximate techniques as proposed by Joyner & Chen (1975) following the concept of absorbing boundaries introduced by Lysmer & Kuhlemeyer (1969). These approximate methods are a common practice among finite element users of commercial codes not specialized to wave propagation problems. In this work we find the response of the topographic features using an exact plane wave excitation in terms of the domain reduction method from Bielak et al. (2003) and compare it with the transmitting boundary approach from Joyner & Chen (1975).

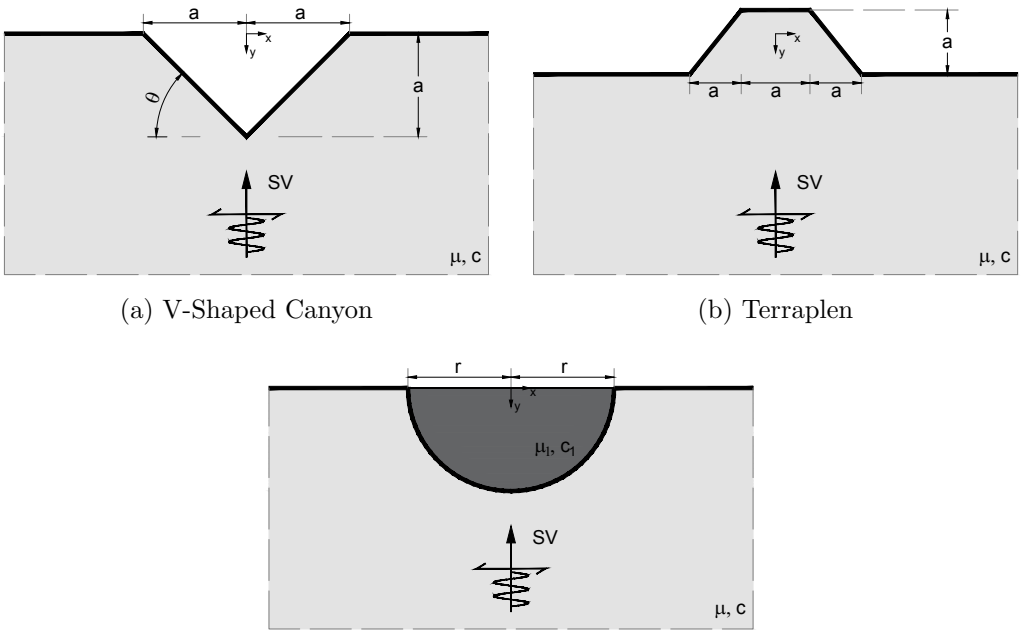

(a) V-Shaped Canyon

(b) Terraplen

(c) Valley

Figure 5.6. Modelos analizados

The transmitting boundary formulated by Joyner & Chen (1975) corresponds to the absorbing boundary from Lysmer & Kuhlemeyer (1969) written as a tractions vector like

$$\tau_B = \rho \beta V_P. \tag{5.22}$$

In the case of absorbing boundaries V_P is the particle's velocity consistent with the scattered field, while in the case of transmitting boundaries V_P is the particle's velocity associated to the incident field. These are applied in the enclosing boundary in the form of external excitation. In eq. (5.22) τ_B represents the traction vector to be applied at the base of the model, ρ is the density of the supporting half-space, β is the shear wave velocity of propagation for the half-space and V_P is the particle's velocity computed as the first time derivative of the incident displacement field. All the models involving the DRM approach are surrounded also by absorbing boundaries to absorb spurious energy generated by the scattterer. Similarly, those models used in testing of the transmitting boundaries are supplemented with absorbing boundaries at the lateral edges. Results are provided in terms of displacements time histories as well as spectral responses along the surface in each topographic feature. The time domain excitation, consists of a Ricker pulse with characteristic frequency $f_c = 2.5\ Hz$ but with frequency content as high as $10\ HZ$. The displacement and velocity pulses are given by:

$$R_D(t) = \left[2.0\left(\pi f_c\left(t - t_c\right)\right)^2 - 1.0\right] e^{-\left(\pi f_c (t - t_c)\right)^2} \tag{5.23}$$

$$R_V(t) = 2.0\left(\pi f_c\right)^2 \left(t - t_c\right)\left(3.0 - 2.0\left(\pi f_c\left(t - t_c\right)\right)^2\right) e^{-\left(\pi f_c (t - t_c)\right)^2} \tag{5.24}$$

where R_D and R_V represent the displacement and velocity field respectively, while t_c is a time mark used to fix the maximum amplitude in the displacement signal. Results at three different receivers in each topography computed by both methods are displayed in fig. 5.7. The rows correspond to the canyon,hill and valley respectively. Although the results from the transmitting boundary approach predict larger amplitudes as compared to the exact solution from an engineering point of view they provide an accurate prediction of the resulting wave field.

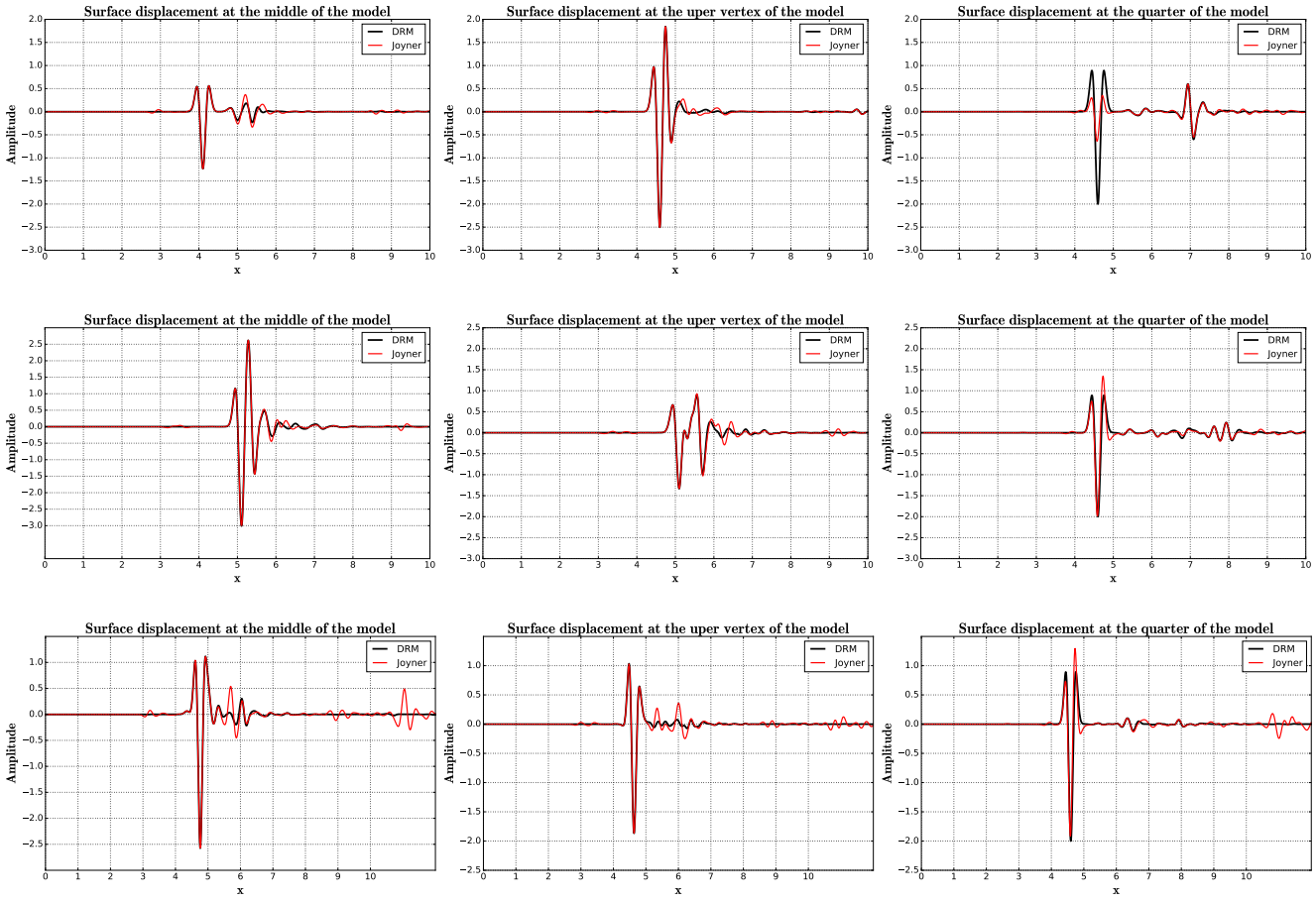

Figure 5.7. Displacement time histories at three different points along the simple topographic shapes shown in fig. 5.6 above. Each trace corresponds to the exact solution following the DRM technique and the approximate solution employing transmitting boundaries.

Conclusions

We have described an explicit time domain finite element solver intended to be used in the determination of spectral amplification factors of models involving topographic irregularities using plane wave analysis. Such codes are the typical resource in engineering applications since it avoids performing frequency domain analysis. As the main

features the code allows the imposition of exact excitation in terms of plane waves using a domain reduction method approach or the use of approximate excitations in terms of seismic motions applied through transmitting boundaries. The implementation is fully parametrized and it receives user element subroutines and material models.

Concluding remarks

This thesis addresses the problem of topographic effects in the determination of the ground motions at a local site. Although there has been a strong effort from the engineering community to understand the effect of geometry in the final response there are no methods to its consideration at the practical level. Most, if not all of these efforts have been focused on interpretation of field records, numerical results from realistic models and a wide variety of parametric analysis of idealized scenarios. All of these efforts confirm the importance of the topographic effect in the final ground motion but have failed to produce applicable results that can be used by practicing engineers. A common factor among the different proposed approaches for topographic effects is the use of numerical modeling with finite element methods, spectral finite element methods and finite difference methods. However all the reported cases require prohibitive computer resources and field data which is rarely available at a consulting office. This work, which is part of a long effort within the group of Mecanica Aplicada at Universidad EAFIT, has the potential to become an new paradigm in the study of the problem. It was built upon the vast amount of theoretical work conducted in the response of simple wedges to generalized plane waves during the middle of the last century. Unfortunately these theoretical contributions were relegated to a secondary and marginal role after the growth in computer resources and numerical power. In our approach we have combined the fundamental theoretical and physical aspects behind the dynamic response of wedges with concepts proper to earthquake engineering such as the tool of the response spectra. In particular we have shown that the theory diffracted waves encloses most of the modifications imparted to the incident seismic waves by the topographic effect. With diffracted waves we are able to explain modifications in the frequency content of the ground displacements as well as the spatial variations in amplitudes. These ideas when combined with specific ranges of structural period allows us to capture the topographic effect with relatively simple to build and implement numerical models which can now be treated by available algorithms.

References

Achenbach, J., 1973. *Wave Propagation in Elastic Solids*, North Holland Publishing Company.

AFPS French Association for Earthquake Engineering, 1995. *French Seismic Code. Guidelines for seismic microzonation studies*.

Aki, K. & Richards, P., 2002. *Quantitative seismology*, Univ Science Books.

Al Atik, L. & Abrahamson, N., 2010. An improved method for nonstationary spectral matching, *Earthquake Spectra*, **26**(3), 601–617.

Asimaki, D. & Mohammadi, K., 2018. On the complexity of seismic waves trapped in irregular topographies, *Soil Dynamics and Earthquake Engineering*, **114**, 424–437.

Assimaki, D. & Jeong, S., 2013. Ground-motion observations at hotel montana during the m 7.0 2010 haiti earthquake: Topography or soil amplification?, *Bulletin of the Seismological Society of America*, **103**(5), 2577–2590.

Banerjee, P. K. & Butterfield, R., 1981. *Boundary element methods in engineering science*, vol. 17, McGraw-Hill London.

Bielak, J. & Christiano, P., 1984. On the effective seismic input for non-linear soil-structure interaction systems, *Earthquake engineering & structural dynamics*, **12**(1), 107–119.

Bielak, J., Loukakis, K., Hisada, Y., & Yoshimura, C., 2003. Domain reduction method for 3D earthquake modelling in localized regions. Part I: Theory, *Bulletin of the Seismological Society of America*, **93**(2), 817–824.

Boore, D., 1972. A note on the effect of simple topography on seismic SH waves, *Bulletin of the Seismological Society of America*, **62**(1), 275–284.

Celebi, M., 1987. Topographical and geological amplifications determined from strong-motion and aftershock records of the 3 march 1985 chile earthquake, *Bulletin of the Seismological Society of America*, **77**(4), 1147–1167.

(EPRI), E. P. R. I., 1993. Guidelines for determining design basis ground motions, volume 2: Appendices for ground motion estimation.

EuroCode8, 2000. *European Committee for Standarization, EuroCode 8*, (EC8) Design Provisions for Earthquake Resistance of Structures, Part 1-1: General Rules-Seismic Actions and General Requirements for Structures, prEN, Brussels.

Gao, Y. & Zhang, N., 2013. Scattering of cylindrical sh waves induced by a symmetrical v-shaped canyon: near-source topographic effects, *Geophysical Journal International*, **193**(2), 874–885.

Gao, Y., Zhang, N., Li, D., Liu, H., Cai, Y., & Wu, Y., 2012. Effects of topographic amplification induced by a u-shaped canyon on seismic waves, *Bulletin of the Seismological Society of America*, **102**(4), 1748–1763.

Geli, L., Bard, P.-Y., & Jullien, B., 1988. The effect of topography on earthquake ground motion: A review and new results, *Bulletin of the Seismological Society of America*, **78**(1), 42–63.

Gomez, J., Restrepo, D., Jaramillo, J., & Valencia, C., 2013. Analysis of the role of diffraction in topographic site effects using boundary element techniques, *Earthquake Science*, **26**(5), 341–350.

Gomez, J., Jaramillo, J., Saenz, M., & Vergara, J., 2016. A superposition based diffraction technique to study site effects in earthquake engineering, *International Journal of Geophysics*.

Google, 2018. Google earth pro.

Han, F., Wang, G. Z., & Kang, C. Y., 2011. Scattering of SH-waves on triangular hill joined by semi-cylindrical canyon, *Applied Mathematics and Mechanics (English Edition)*, **32**(3), 309–326.

Jaramillo, J. D., Gomez, J. D., Saenz, M., & Vergara, J. C., 2012. Analytic approximation to the scattering of antiplane shear waves by free surfaces of arbitrary shape via superposition of incident, reflected and diffracted rays, *Geophysical Journal International*, **192**(3), 1132–1143.

Joyner, W. B. & Chen, A. T. F., 1975. Calculation of nonlinear ground response in earthquakes, *Bulletin of the Seismological Society of America*, **65**(5), 1315–1336.

Kawase, H., 1988. Time domain response of a semicircular canyon for incident sv, p, and rayleigh waves calculated by the discrete wavenumber boundary element method, *Bulletin of the Seismological Society of America*, **78**, 1415–1437.

Keller, J. B., 1956. Diffraction of a convex cylinder, *Electromagnetic Wave Theory Symposium*, **137**, 312–321.

Keller, J. B., 1962. Geometrical theory of diffraction, *J. Opt. Soc. Am.*, **52**(2), 116–130.

Kouyoumjian, R. G. & Pathak, P. H., 1974. A uniform geometrical theory of diffraction for an edge in a perfectly conducting surface, *Proceedings of the IEEE*, **62**(11), 1448–1461.

Lysmer, J. & Kuhlemeyer, R., 1969. Finite dynamic model for infinite media, *JOURNAL OF ENGINEERING MECHANICS-ASCE (JOURNAL OF THE ENGINEERING MECHANICS DIVISION)*, **859**, 877.

MacDonald, H., 1902. *Electric Waves*, Cambridge University Press.

Pao, Y. H. & Varatharajulu, V., 1976. Huygens principle, radiation conditions, and integral formulas for the scattering of elastic waves, *The Journal of the Acoustical Society of America*, **59**(6), 1361–1371.

Restrepo, D., Bielak, J., Serrano, R., Gómez, J., & Jaramillo, J., 2016. Effects of realistic topography on the ground motion of the colombian andes–a case study at the aburrá valley, antioquia, *Geophysical Journal International*, **204**(3), 1801–1816.

Sáenz, M., Sierra, C., Vergara, J., Jaramillo, J., & Gomez, J., 2019. Site specific analysis using topography conditioned response spectra, *Soil Dynamics and Earthquake Engineering*, **123**, 470–497.

Sanchez-Sesma, F., 1985. Diffraction of elastic sh waves by wedges, *Bulletin of the Seismological Society of America*, **75**(5), 1435–1446.

Sanchez-Sesma, F., 1990. Elementary solutions for response of a wedge-shaped medium to incident sh and sv waves., *Bulletin of the Seismological Society of America*, **80**(3), 737–742.

Sánchez-Sesma, F. J., 1985. Diffraction of elastic SH waves by wedges, *Bulletin of the Seismological Society of America*, **75**(5), 1435–1446.

Sánchez-Sesma, F. J., 1987. Site effects on strong ground motion, *Soil Dynamics and Earthquake Engineering*, **6**(2), 124–132.

Sánchez-Sesma, F. J. & Rosenblueth, E., 1979. Ground motion at canyons of arbitrary shape under incident SH waves, *Earthquake Engineering & Structural Dynamics*, **7**(5), 441–450.

Sommerfeld, A., 1896. Mathematische theorie der diffraktion., *Math.Ann*, **47**, 317–374.

Taborda, R. & Bielak, J., 2011. Large-scale earthquake simulation: Computational seismology and complex engineering systems, *Computing in Science & Engineering*, **13**(4), 14–27.

Trifunac, M., 1971. Surface motion of a semi-cylindrical alluvial valley for incident plane sh waves, *Bulletin of the Seismological Society of America*, **61**(6), 1155–1770.

Trifunac, M. D., 1973. Scattering of plane SH waves by a semicylindrical canyon, *Earthquake Engineering & Structural Dynamics*, **1**, 267–281.

Trifunac, M. D. & Hudson, D. E., 1971. Analysis of the Pacoima dam accelerogram—San Fernando, California, earthquake of 1971, *Bulletin of the Seismological Society of America*, **61**(5), 1393–1411.

Tsaur, D.-H. & Chang, K.-H., 2008. An analytical approach for the scattering of SH waves by a symmetrical V-shaped canyon: shallow case, *Geophysical Journal International*, **174**(1), 255–264.

Tsaur, D.-H. & Hsu, M.-S., 2013. Sh waves scattering from a partially filled semi-elliptic alluvial valley, *Geophysical Journal International*, **194**(1), 499–511.

Tsaur, D.-H., Chang, K.-H., & Hsu, M.-S., 2010. An analytical approach for the scattering of SH waves by a symmetrical V-shaped canyon: deep case, *Geophysical Journal International*, **183**(3), 1501–1511.

Valencia, C., Gomez, J., Jaramillo, J., Saenz, M., & Vergara, J., 2017. The scattering of sh waves by a finite crack with a superposition-based diffraction technique, *Studia Geophysica et Geodaetica*, **61**(1), 93–114.

Zhang, N., Gao, Y., Li, D., Wu, Y., & Zhang, F., 2012. Scattering of SH waves induced by a symmetrical V-shaped canyon: a unified analytical solution, *Earthquake Engineering and Engineering Vibration*, **11**(4), 445–460.